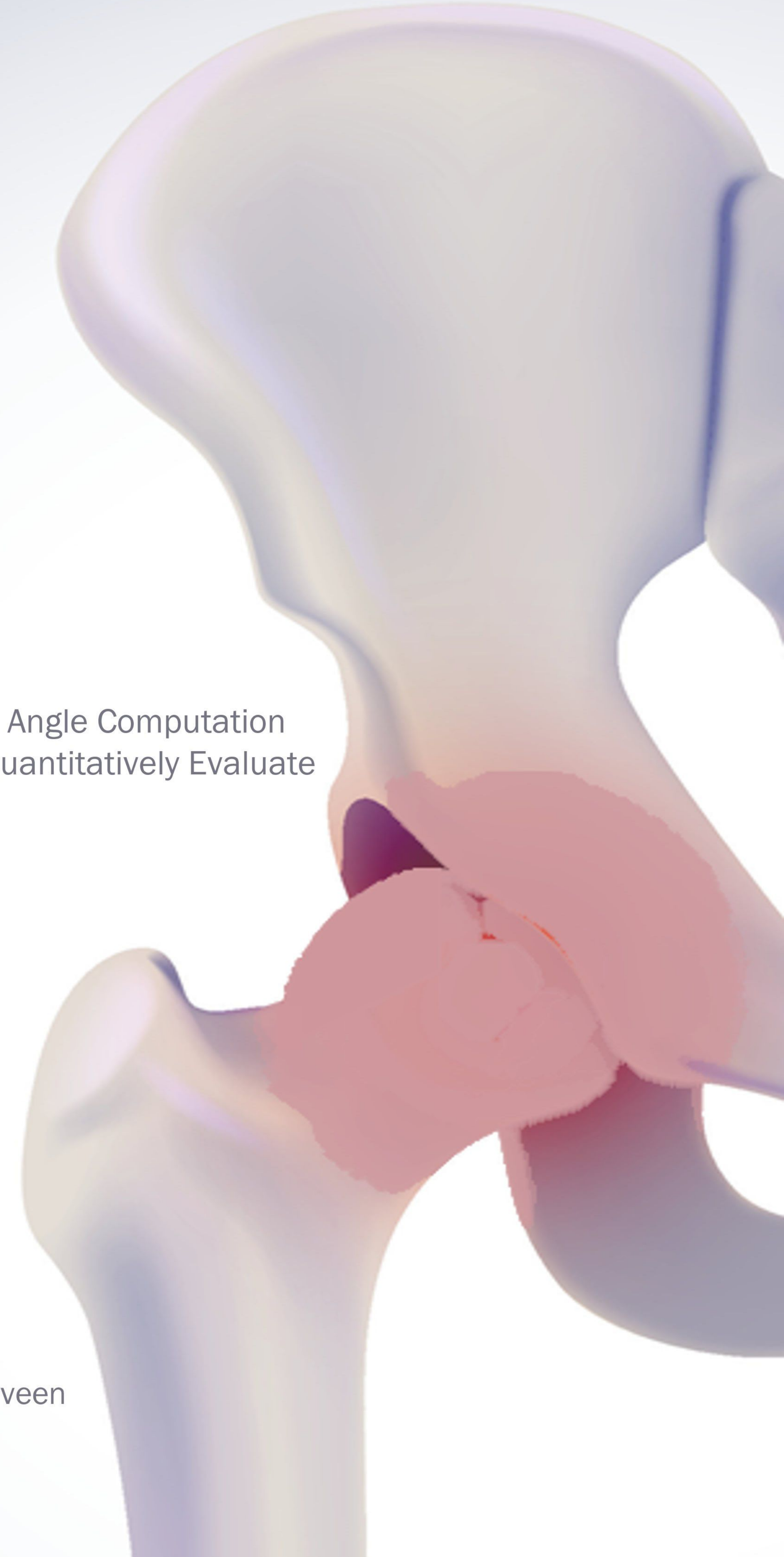

Semi-automated Alpha Angle Computation Based on ZTE MRI to Quantitatively Evaluate CAM Morphology

Technical Medicine
MSc Thesis by Vera Ederveen

Semi-automated Alpha Angle Computation Based on ZTE MRI to Quantitatively Evaluate CAM Morphology

By

Vera Ederveen

Student number: 4445368
Date: 23-05-2023

Thesis in partial fulfilment of the requirements for the joint degree of Master of Science in

Technical Medicine

Leiden University | Delft University of Technology | Erasmus University Rotterdam

Master thesis project (TM30004, 35 ECTS)
Erasmus MC - Department of Orthopedics and Sports Medicine
September 2022 - May 2023

Supervisors:
Chair and medical supervisor: Dr. Adam Weir - Erasmus MC
Technical supervisor: Dr. Ir. Nazli Tümer - TU Delft
Additional supervisor: Dr. Derek van Loon - Erasmus MC

Thesis committee members:
Independent committee member 1: Dr. Jukka Hirvasniemi - Erasmus MC
Independent committee member 2: Dr. Anne Brandts - Groene Hart Ziekenhuis

1

Preface

This graduation project reflects the final work I have delivered within the study program of Clinical Technology. I positively look back at the past years and I am very glad that I choose to do this study. I am intrigued by healthcare, but always have the urge to fully understand the process. Clinical Technology was a perfect fit as it provided me with the technical background to gain this understanding. Because of the positive experience I had during my second-year internship in the technical medicine master's program, where I was supervised by Adam and David, I approached Adam to graduate at the department of orthopedics and sports medicine. It was very exciting to research how technology could contribute to this specialism.

I want to thank my supervisors, Nazli and Adam, for their guidance throughout my research journey. The weekly meetings with their critical opinions kept me on track. In particular, I would like to express my gratitude to Adam, who provided me with a unique learning opportunity during the outpatient clinic sessions. I am grateful that you gave me the responsibility of seeing patients by myself. It taught me a lot about clinical reasoning and diagnosis, as well as the healthcare system. I especially enjoyed the anatomical and practical discussions we had, which further broadened my knowledge. Thanks to his network, I had the opportunity to observe the entire patient journey, from the outpatient clinic to the operating room and physiotherapy sessions. So I would also like to thank Tom, Willem, Matthias, and Loes for taking the time to share their knowledge with me.

I would like to thank David for his contribution to my master thesis by validating the semi-automated measurements. I hope that this research is of any use to your promotion as well and I wish you the best of luck. Most importantly, I would like to thank Derek. Although he joined the project later on, his assistance helped me overcome many obstacles and technically taught me a lot.

Finally, I would like to thank my friends and family for their support during the past months. As any postgraduate knows, the journey has its share of ups and downs. In particular, I would like to thank Frederique, who started on the same day as I did and will graduate alongside me. We have worked besides each other practically every day and she has been a great support and discussion partner.

Whatever new challenges I will face in the future, I will take the knowledge and experiences that I have gained from this project with me.

Vera Ederveen
May 2023

List of Abbreviations

2D	Two Dimensional
3D	Three Dimensional
AP	Antero-Posterior
CI	Confidence Interval
CT	Computed Tomography
DICOM	Digital Imaging and Communications in Medicine
FAIS	Femoro-Acetabular Impingement Syndrome
FHC	Femoral Head Center
FHN	Femoral Head Neck
FNA	Femoral Neck Axis
FNC	Femoral Neck Center
FOV	Field Of View
FSA	Femoral Shaft Axis
HNO	Head Neck Offset
HNOR	Head Neck Offset Ratio
ICC	Intraclass Correlation Coefficient
MRI	Magnetic Resonance Imaging
MAD	Mean Absolute Difference
MSF	Model Specific Factor
NEX	Number of Averages
OA	Osteoarthritis
PACS	Picture Archiving and Communication System
ROI	Region Of Interest
ROM	Range of Motion
SD	Standard Deviation

SNR	Signal-to-Noise Ratio
STL	Standard Triangle Language
TI	Triangular Index
ZTE	Zero Echo Time

Contents

2

Abstract

Introduction: This study developed an open access workflow for semi-automated three dimensional (3D) alpha angle measurement to allow researchers and clinicians to evaluate the 3D degree of cam morphology in a fast and objective manner, regardless of their financial resources.

Method: In the semi-automated workflow, geometrical approaches were applied to eight manually segmented 3D models of the proximal femur (four left and four right). These 3D models were created from Zero Echo Time (ZTE) Magnetic Resonance Imaging (MRI) images of four randomly selected individuals from the Feyenoord cohort, thus imparting no radiation to the subjects. Important landmarks were localized on the 3D models with subsequent radial reformatting and alpha angle computation in 12 radial sections. Novel strategies included radial section-specific spherical least square fitting to approximate the radius of the femoral head, outlier detection to handle surface irregularities and model specific thresholds to account for the asphericity of the femoral head. For six clockwise positions (12:00, 1:00, 2:00, 3:00, 6:00, and 9:00 o'clock), both qualitative and quantitative validation were conducted by comparing the semi-automated measurements to manual alpha angle measurements performed by an experienced musculoskeletal (MSK) radiologist. To evaluate the inter-observer reliability, the mean absolute difference (MAD) and intraclass correlation coefficient (ICC) were calculated for various automatic approaches, depending on which novel strategies were incorporated. Additionally, the radii (mm) and the measurement time (minutes) were compared between the manual and semi-automated approach.

Results: Reliability assessment showed poor agreement with ICCs ranging from -0.02 to 0.40, depending on which automatic approach was used. The highest ICC of 0.40 [95%CI: -0.51 - 0.89] was achieved using a radial section-specific radius without alteration of the spherical threshold or application of outlier detection. MADs ranged from 20°- 23°. Statistically significant differences (p-value <0.003) between manually drawn circular radii and automatically fitted radial section-specific spherical radii were found for 50% of the 3D hip models. All manually drawn circular radii were smaller than the radii of the automated fitted spheres. Variation in radii between and within radial sections were qualitatively and quantitatively demonstrated. Lastly, computation of the 12 clockwise alpha angles was performed by the workflow within 26 seconds, indicating a time difference of approximately 15 minutes compared to manual measurements.

Conclusion: The proposed semi-automated workflow is capable of computing 12 alpha angles across radial sections surrounding the femoral head in a fast and objective manner. The performance of the workflow could be improved by refining landmark localization, enhancing the quality and segmentation of ZTE MRI scans, enlarging the validation dataset and analysis of prior workflow error propagation. This study established that the femoral head is not perfectly spherical. This affects the accuracy of alpha angle measurements as it is strongly sensitive to radius estimation and therefore questions the reliability of the alpha angle as diagnostic measure of cam morphology. Future research should explore the potential of complementary alternative imaging parameters such as the Head-Neck-Offset Ratio (HNOR) and Triangular Index (TI), as well as the use of statistical shape models that incorporate the imperfect spherical morphology of the femoral head.

3

Introduction

3.1. Femoroacetabular impingement syndrome

Femoroacetabular Impingement syndrome (FAIS) is defined as an abnormal contact between the acetabulum and the head-neck junction of the femur during motion.[1] The impingement can be caused by two types of FAIS: a cam morphology or a pincer morphology. Cam morphology involves extra bone formation on the anterolateral side of the femoral head-neck junction, while pincer morphology involves extra bone formation on the anterolateral side of the acetabulum, leading to an increased coverage of the femoral head (Figure 3.1). This thesis focuses on the cam morphology type of FAIS. The prevalence of cam morphology ranges from 5-25 % in the general male population and 5-15 % in the general female population. [2] The incidence is much higher in young male athletes, with reported prevalences above 60 % for high-impact sports such as football, basketball, and ice hockey.[2] This is likely due to the gradual formation of cam morphology during skeletal maturation, which can be influenced by high-impact sports as the skeleton is highly responsive to mechanical loading. [3]

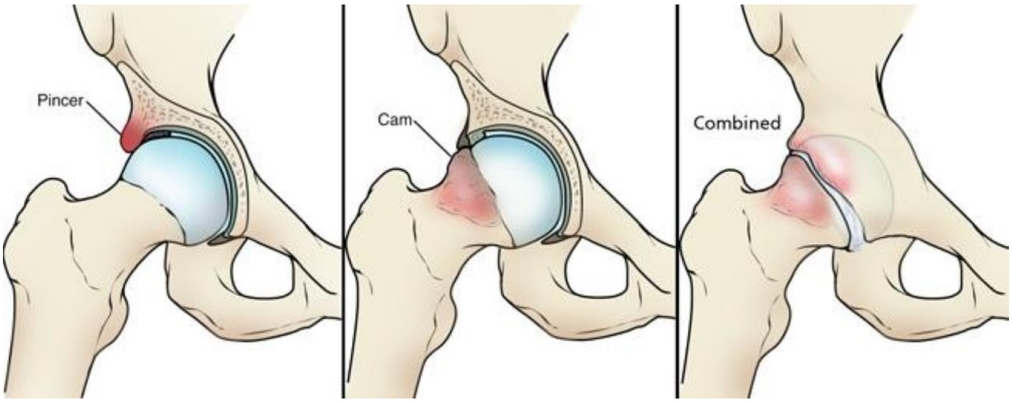

Figure 3.1: Femoroacetabular impingement syndrome (FAIS). **Left:** pincer morphology, **Middle:** cam morphology, **Right:** combined pincer and cam morphology.[4]

3.2. Sequelae

As a result of these abnormal morphologies, impingement during repetitive flexion of the hip with or without rotation can result in serious sequelae such as labral tears and chondrolabral damage at the anterosuperior and anterolateral side of the chondrolabral junction of the acetabulum.[5] Consequently, individuals with FAIS are at an increased risk of developing early osteoarthritis (OA), which leads to hip joint pain and dysfunction. Currently, OA treatment is limited to pain management and joint replacement for end-stage disease, with no cure available, and the cartilage damage being irreversible.[2] This motivates researchers to develop effective OA prevention strategies.

3.3. Diagnosis

Hip arthroscopy is one of the therapeutic options available for patients with cam impingement, with the aim of reducing symptoms. The procedure involves modifying the shape of the proximal femur and removing the bony protrusion at the femoral head-neck junction. This has proven to show symptomatic benefit beyond 5 years and may modify the long term risk of developing OA. [2] Before deciding to perform a hip arthroscopy, a diagnosis of cam or pincer morphology must be officially established through symptoms, clinical signs, and imaging findings that are consistent with FAIS, as advised by the Warwick Agreement (Figure 3.2). Symptoms may involve pain in the hip and groin region, or in the back, buttock, or thigh, while clinical signs are restricted and painful ROM, stiffness, locking, catching, clicking, or giving way of the hip joint.[4] Imaging findings are a visible presence of cam morphology, which are recommended to be examined on plain radiographs, on an anteroposterior (AP) pelvic view or lateral femoral neck view.[2]

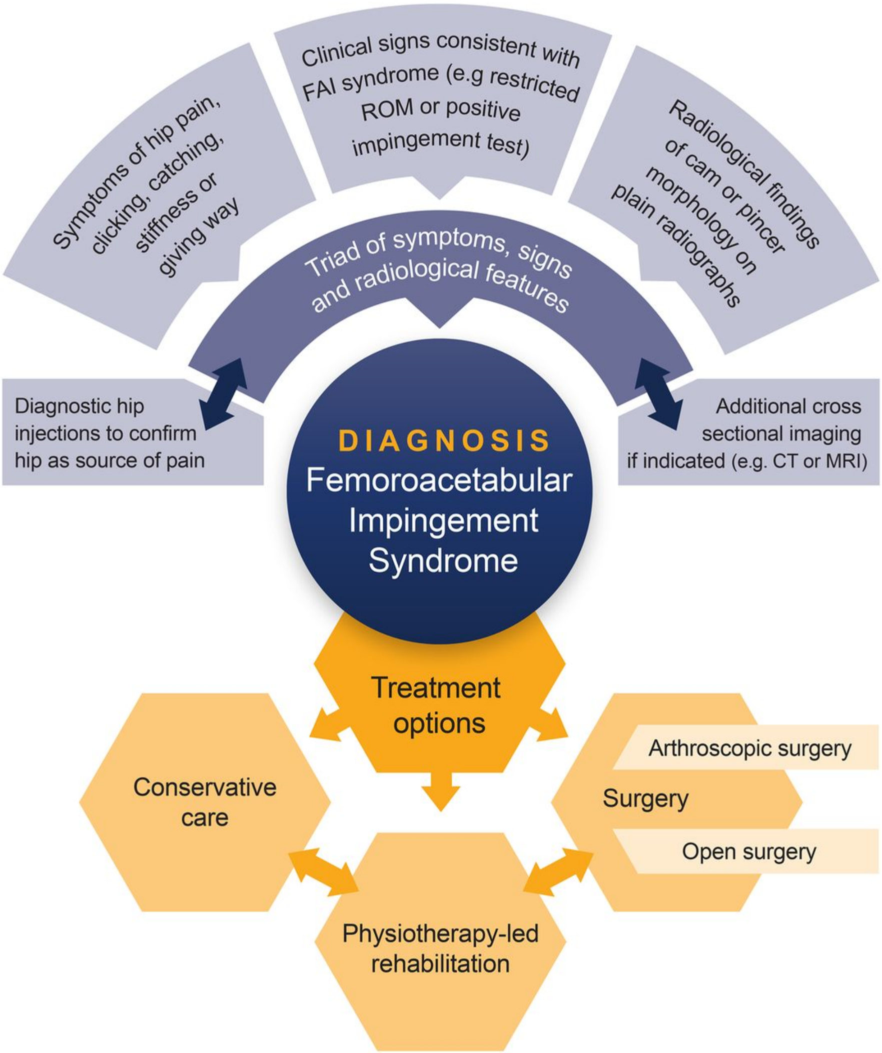

Figure 3.2: Pathway for the management of femoroacetabular impingement syndrome (FAIS).[4]

3.4. The alpha angle

In addition to assessing the morphology of the femoral head through qualitative analysis, clinicians can perform a quantitative measurement called the alpha angle to evaluate femoral deformity. The alpha angle indicates inadequate anterolateral head-neck offset and femoral head asphericity.[6] Currently, radiologists use the Nötzli method to measure the alpha angle on 2D anteroposterior (AP), frog-lateral, Dunn-view, or Lauenstein radiographs [7]. The Nötzli method involves several steps: firstly, a circle is drawn on the image that best fits the femoral head on the radially reformatted image. The center of the circle represents the femoral head center (FHC). The femoral neck center (FNC), which is the center of the isthmus of the femoral neck, is then connected to the FHC to establish the femoral neck axis (FNA). A second line is drawn from the FHC to the point (P’) at which the femoral head laterally exceeds the best fit circle.[7] Finally, the alpha angle is measured as the angle between FHC-P’ and the FNA (Figure 3.3).

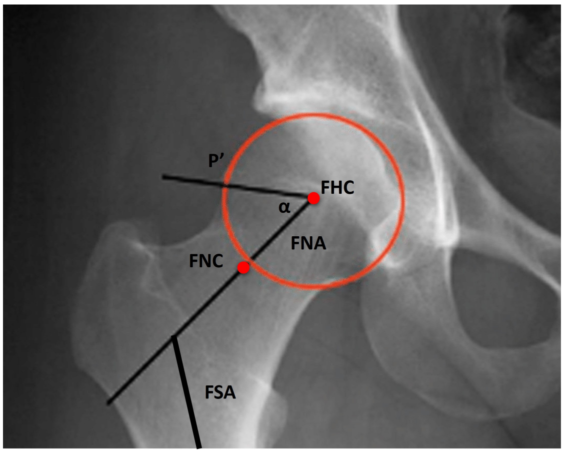

Figure 3.3: Alpha angle measurement according to the Nötzli method, using plain radiographs. **FHC** = The femoral head center, **FNC** = the femoral neck center,**FSA** = the femoral shaft axis, **FNA** = the femoral neck axis, **P’** = the point at which the femoral head laterally exceeds the best fit circle. [8]

3.5. Limitations current practice

There are several drawbacks associated with the Nötzli method. Firstly, the method is labour-intensive and subjective as it involves drawing the best-fit circle and two lines, followed by angle measurement. Secondly, the use of X-ray imaging provides only a 2D view, restricting the ability to assess the full extent of femoral deformity accurately. Although X-ray imaging is a quick, inexpensive, and widely available imaging option, it may not be optimal for diagnostic purposes. In previous studies, the prevalence of cam morphology may have been underestimated because a cam morphology may not be visible in the plane represented by the X-ray. Consequently, a wide range of alpha angle thresholds (53° to 80°) have been reported for diagnosing cam morphology [2].

3.6. Three-dimensional imaging

To provide a more reliable assessment of the location and prevalence of the cam morphology and to establish accurate alpha angle thresholds, the application of 3D imaging could be considered. This enables measurement of the full circumferential alpha angle centered around the femoral head. The use of 3D measurements would facilitate large-scale research and clinical studies, enabling the monitoring of cam morphology development and offering insights into the extent and location of cam. [9] In particular, 3D volume rendering can be used to create patient-specific hip joint models, which can contribute to accurate diagnosis and assist orthopedic surgeons in pre-operative planning for potential hip arthroscopy candidates. This will benefit the patient as it minimizes the risk of residual impingement after the surgery. [9]

3.7. Existing software

There are currently several software programs available from commercial companies that use 3D image series as input to generate a 3D model for visualizing hip impingement and measuring 3D quantitative diagnostic measures related to FAIS. Examples of these companies include *Clinical Graphics, Visual Human Software, and Medicad*. Due to the commercial nature of these companies, the high costs per patient associated with these programs prevent their widespread use, particularly for clinicians and researchers with limited funds. The inability to use this software not only hinders progress in FAIS research but also prevents clinicians from providing patients with the highest quality of care, leading to conflicting ethical and economic concerns.

3.8. ZTE Imaging

For detailed 3D assessment of the bony morphology of the hip and for surgical planning, computed tomography (CT) is considered the golden standard.[10] This is both the case for commercial companies and clinical practice. The disadvantage of CT is that it involves harmful radiation to the gonadal region when creating images, which puts patients at risk. An alternative 3D imaging method is Magnetic Resonance Imaging (MRI). However, in conventional MRI, bone is displayed as a void. This is because the contrast in MRI is based on the proton density of tissues and characteristic relaxation times (T1 and T2). In comparison to soft tissue, cortical bone has a very short transverse relaxation time ($T2^* \approx 270$ μs) and low water content (20-40 %).[10] During image acquisition, the signal of bone has already decayed, leading to bone being displayed as a void on the resulting image.

A new advance in MRI is the Zero Echo Time (ZTE) sequence. This achieves nearly zero echo time by switching to radiofrequency acquisition immediately after application of the radiofrequency pulse. This, in combination with radial k-space filling strategies and very low flip angles of approximately 1°, enables capturing the quickly decaying T2* signal from bone.[11, 12, 13] It reduces T1 and T2* effects, resulting in a proton density weighted image with clear visualization of cortical bone. Previous studies have examined the use of ZTE imaging to asses the morphology of the hip by comparing 2D quantitative measurement performed on ZTE MRI scans to CT scans. Good to excellent agreement was demonstrated (ICC ranging from 0.62 to 0.90).[10] This shows the potential of ZTE MRI to be used as an imaging modality for 3D quantitative measurement.

3.9. Goals and objectives

The objective of this study is to develop an open access workflow for (semi)-automated three dimensional alpha angle measurement based on ZTE MRI based 3D hip models. This protects patients from harmful ionizing radiation. The workflow aims to allow researchers and clinicians to evaluate the three-dimensional degree of femoral morphology in a fast and objective manner, regardless of their financial resources.

4

Methods

This section provides a description of how the workflow has been created. First, the pre-proces in which the requirements of the workflow were inquired among end-users is described. Second, the study population and imaging data that was used to develop the workflow is stated. Then, an overview of the workflow is provided, including an elaborated explanation of each step. The last part of this section provides the validation methodology used to assess the performance of the semi-automatic alpha angle workflow.

4.1. Inventory of requirements

Before the workflow was created, a questionnaire was conducted among 15 clinicians who regularly see FAIS patients in their clinical practice. This included 6 radiologists, 4 orthopaedic surgeons and 5 sports physicians from different health institutions. The respondents were approached via the network of one of the supervisors of this thesis (Sports doctor *A. Weir*) and his colleagues (Orthopedic surgeon *T. Piscaer* and Radiologist *D. Hanff*).

A questionnaire was set up via Google Forms. The aim of the questionnaire was to inquire among the end-users what the current clinical practice for FAIS patients is, and what requirements the workflow should take into account. To address these topics, the questionnaire consisted of the following questions:

1. What is your job?
2. How many patients with hip/groin related complaints do you see per month in the outpatient clinic?
3. How many of these patients are diagnosed with FAIS?
4. What type of imaging do you use for diagnosing FAIS or pre-operative planning?
5. In what manner do you use imaging: solely for visual analysis or also for performing measurements?
6. If measurements are performed, which measurements do you perform and what threshold do you use for that measurement?
7. How much time does it take you to take the measurement?
8. What software do you use for the measurement?
9. What is your opinion on the user friendliness of the software: bad - average or good?
10. What do you miss in the current software?
11. Besides measurements, the software aims to create a 3D model of the hip based on the scans of the patient. What would you like to see in this model?
12. Additional comments/suggestions?

4.2. Study Population

To evaluate the workflow, zero echo time (ZTE) MRI scans from the Feyenoord cohort were used. The Feyenoord cohort consists of 89 male football players aged 12-19 at baseline (2010). The Feyenoord cohort data was initially collected to investigate if a cam morphology can evolve over time in adolescents and whether such an evolution continues after skeletal maturation. Secondly, the aim of these previous studies was to evaluate whether clinical and/or radiographic features are associated with a cam morphology or are predictive for the formation of a cam morphology.[14] To evaluate the morphology of the hip joint, an X-ray (anteroposterior view and frog-leg lateral view) was made at t = 0 years, t = 5 years and t = 10 years for each hip joint. The 10-year follow-up also includes 35 ZTE-MRI scans available for analysis. These radiation free ZTE-MRI scans of four randomly selected participants, aged between 24 and 30 (mean age: 27.4 ± 2.43 years) were used to evaluate the performance of the workflow developed in this thesis.

4.3. Imaging Data

A coronal pelvic ZTE acquisition protocol was conducted for each patient at the 10-year follow up in the Feyenoord study. All patients were imaged using a clinical 3.0 Tesla scanner (Signa Premier, GE Healthcare) and an air coil, covering the pelvis of the subject to receive the signal. The MRI scans acquisition parameters are stated in Table 4.1.

Parameter	**Value**
Magnetic field strength (Tesla)	3.0
FOV (mm)	298 x 298
Echo time (ms)	0.02
Repetition time (ms)	788.792
Flip angle (°)	2
Bandwidth (kHz)	241
Slice thickness (mm)	1.0
NEX	3
Number of slices	280
Pixel spacing (mm)	0.5859 x 0.5859

Table 4.1: MRI acquisition parameters of the coronal pelvis ZTE protocol.

4.4. Overview Workflow

Figure 4.1 provides an overview of the workflow, illustrating the key steps involved in transforming a stack of ZTE MRI scans into the output of 12 alpha angles using a semi-automatic approach. These alpha angles were measured within 12 evenly distributed radial sections, all centered around the femoral head. The initial step of the semi-automated workflow is the segmentation of the ZTE MRI scans to create 3D hip models, as explained in section 4.6. These 3D hip models were subsequently used as input for the fully automatic part of the workflow, responsible for the computation of alpha angles. This automated part can be divided into three main steps: landmark localization, radial reformatting, and alpha angle computation. The rationale behind each methodis elaborated including images to visually support the understanding of the workflow (section 4.7 to section 4.9)

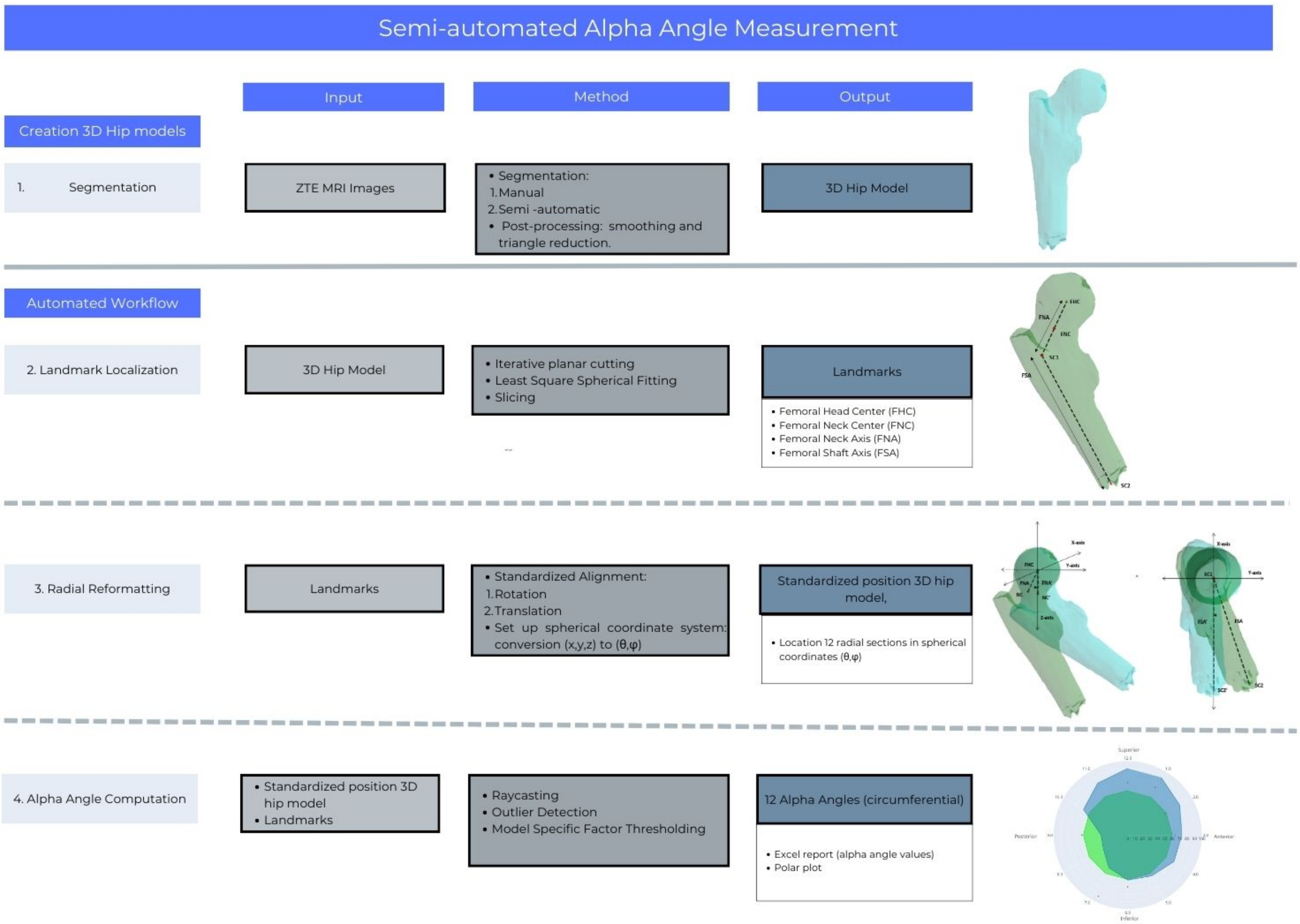

Figure 4.1: Overview of the semi-automated alpha angle measurement workflow.The first step in the semi-automated workflow is segmentation of the ZTE MRI scans to create 3D hip models. These 3D hip models serve as input for the automated workflow to compute alpha angles. **FHC** = Femoral Head Center, **FNC** = Femoral Neck Center, **NC'** = Rotated Neck Center, **FNA** = Femoral Neck Axis, **FNA'** = Rotated Femoral Neck Axis, **SC1** = Shaft Centroid 1, **SC2** = Shaft Centroid 2, **SC2'** = Rotated Shaft Centroid, **FSA** = Femoral Shaft Axis, **FSA'** = rotated Femoral Shaft Axis.

4.5. Software

To create the 3D hip models through manual segmentation, Materialise Mimics Version 25.0 software was used. Subsequently, Materialise 3-matic Version 17.0 was used for post-processing the 3D hip models. For semi-automatic segmentation and all subsequent steps in the workflow to calculate alpha angles, code was developed in Python 3.9.16.[15]

4.6. Creation of 3D Hip Models

First, an attempt was made to segment the proximal femur in the ZTE MRI scans based on semi-automated segmentation. Semi-automatic segmentation is preferred over manual segmentation if the results are accurate and precise, because it is objective and more time efficient. [16] This does mean that consistently and repeatedly, the delineation of the proximal femur by the semi-automatic segmentation algorithm should align closely to the actual boundaries of the proximal femur. Figure 4.2 shows an overview of the semi-automatic segmentation pipeline executed in this thesis and section 4.6.1 explains each step in the pipeline.

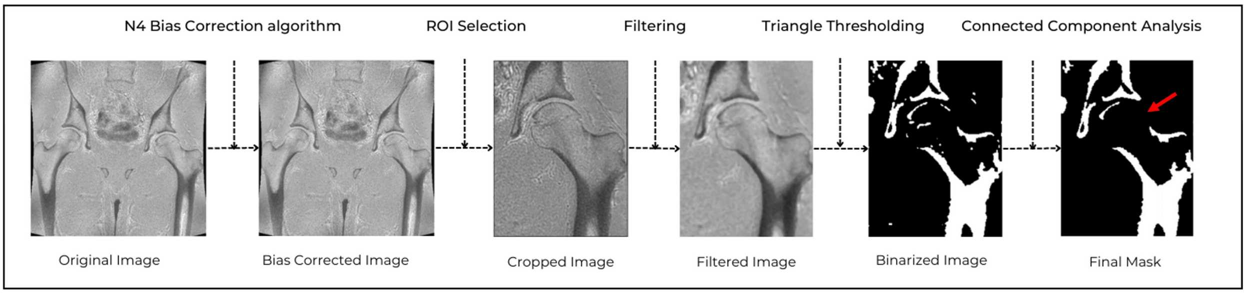

Figure 4.2: Overview of the segmentation pipeline. **Top:** the steps performed in the pipeline. **Bottom:** the resulting MRI image after post-processing. The red arrow in the most right image indicates the femoral head neck junction at which the cortical bone is no longer visible in the segmented mask.

Due to significant noise in the ZTE MRI scans, the 3D hip models that were created were not accurate enough to be able to work with in subsequent steps. Filtering, threshold alteration and connected component analysis were attempted methods to remove the undesired noise. Unfortunately, this also led to removal of the cortical bone, especially at the site of the femoral head neck junction (Figure 4.2 - most right image). Considering the main focus of this thesis was the development of a workflow for alpha angle measurement, manual segmentation was used instead to obtain precise 3D models of the hip (section 4.6.2).

4.6.1. Semi-automatic Segmentation

The semi-automated segmentation pipeline was based on an approach proposed by *Wiesinger et al*. [17] This approach was originally developed for bone segmentation of the head. The ZTE MRI scans of the head were subjected to the following operations by *Wiesinger et al*:

- Logarithmic inversion.
- Histogram based bias correction.
- Two-sided thresholding: thresholds based on the full-width-half-maximum of the noise and signal peak in the histogram.
- Refinement of the segmentation: distance-transform operations, connected component analysis and morphological operations.

Not all steps of the approach proposed by *Wiesinger et al* yielded similar results for bone segmentation of the hip. The steps that did improve the bone segmentation of the hip were adopted in the pipeline: histogram based bias correction to eliminate bias and connected component analysis to remove noise. Additional operations were applied for pelvic ZTE MRI scans specific as depicted in Figure 4.2. Each step within the semi-automatic segmentation pipeline is explained below.

Step 1: Conversion from DICOM to NIfTI
The ZTE images were stored as DICOM files. Each slice represented a separate DICOM file. DICOM is a standard used for handling, storing, printing and transmitting information in medical imaging. NIfTI is a standard originally designed for neuroimaging in specific. It saves raw image data as a 3D image instead of 2D slices like in DICOM. Since the bias correction performed in step 2 of the semi-automatic segmentation workflow requires a 3D image as input, the DICOM files were transformed into a NIfTI file. [18]

Step 2: Histogram based bias correction
Bias is a non-uniform signal response across the field of view (FOV) caused by different coil sensitivities. It leads to variations in tissue intensities across the image in different locations. This can be observed through a broadened soft-tissue peak in the image histogram.[19] To correct for bias, the N4 bias correction algorithm was applied.[20] This algorithm normalizes pixel intensities within each ROI based on the corresponding soft-tissue peak signal intensity. The result is a more accurate estimation of true tissue intensities.

Step 3: ROI Selection
The ZTE MRI scans were acquired with a FOV covering the entire pelvis. To remove a large portion of all unwanted bone prior to generating a 3D model, a region of interest (ROI) was selected. The middle slice of all slices is certain to contain the entire coronal contour of the proximal femur and served as a robust image to select the ROI. Using a module from the cv python package ('selectROI'), the workflow allows the user to select the proximal femur as ROI within the image. Consequently, the selected ROI is selected in all slices and used to crop all images.

Step 4: Filtering
Gaussian and median filters were applied to the cropped ZTE images to filter out different types of noise. A gaussian filter was applied because it is particularly effective in removing gaussian noise, which shows itself as a random variation in brightness.[21] A median filter is particularly effective at removing speckle and salt and pepper noise while preserving edges in the image.[22] This salt and pepper noise is characterized as random black and white pixels scattered throughout the image, while speckle noise is characterized by a granular pattern of bright and dark pixels. [23]

Step 5: Thresholding
Triangle thresholding was performed to convert the grayscale images into binary images. This involves constructing a line between the maximum value of the histogram and the lowest value, and computing the normal distance *d* for all values on the line. The maximum value of d represents the threshold level, as shown in Figure 4.3.[24] The object of interest in the images is the cortical bone, which produces a low signal peak, therefore this thresholding method was chosen.

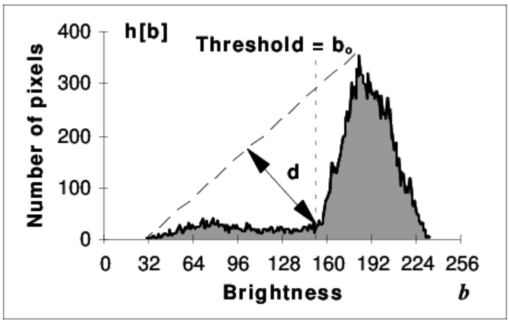

Figure 4.3: Example histogram with triangular thresholding method. A line is constructed from the maximum value of the histogram and the lowest value. Then the normal distance *d* is computed for all values on the line. The maximum value of *d* represents the threshold level as is shown by the arrow in the image. [25]

Step 6: 2D Connected Component Analysis
To further remove noise, a connected component analysis was performed. This involved removing all regions with fewer than 75 connected pixels, a condition that was determined empirically.

Step 7: 3D Volume Rendering
The marching cubes algorithm was used to create a 3D model from the binary segmented images.[26]

Step 8: 3D Connected Component Analysis
A second connected component analysis was performed, this time in 3D. The rationale behind this was to count the number of pixels belonging to each component, and then find the largest connected component, while removing all the other components. As a result, regions representing the background and noise were removed, and the femur was separated from the acetabulum, leaving only a 3D model of the proximal femur. The only requirement is that the user ensures that the proximal femur is the largest component when selecting the ROI in step 3.

4.6.2. Manual segmentation

Eight hips (four left and four right) were manually segmented using Materialise Mimics Version 25.0 software.The ZTE MRI DICOM images were imported into the software. The multiple slice edit tool was used to segment several slices which automatically interpolates the values for slices in between (Figure 4.4). Each slice was manually checked and edited to improve the interpolated estimate. The segmentation was exported as a binary standard triangle language (STL) file for further adjustments. This binary STL file includes the 3D mesh of the proximal femur with a smoothing factor of 0.3 applied during 2 iterations. A triangle reduction was applied with a tolerance of 0.05 to reduce computational time.

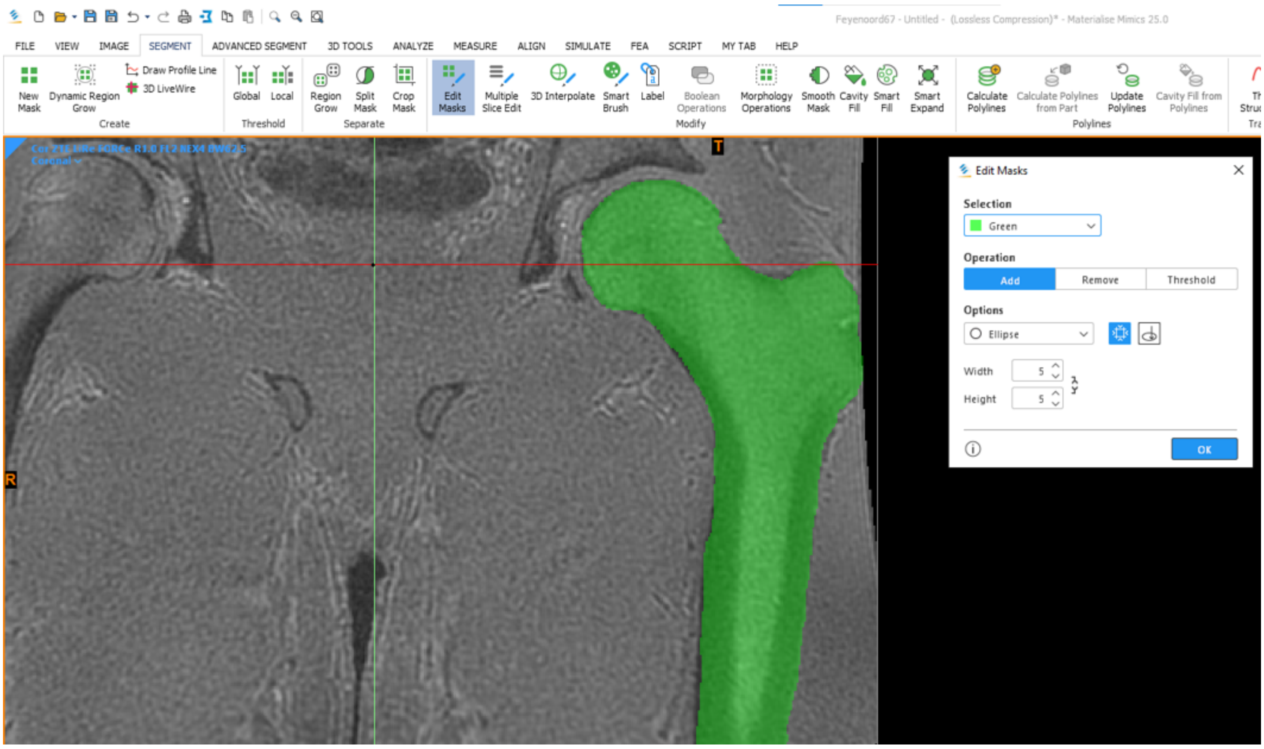

Selection: Green
Operation: Add
Options: Ellipse
Width: 5
Height: 5

Figure 4.4: Manual segmentation of the left femur using ZTE MRI DICOM images. The green mask represents the pixels belonging to the femur according to the assessor.

4.6.3. Mesh Filtering

The fix-wizard, a tool in Materialise 3-matic, was used to ensure the 3D models were watertight. This was required for further steps in the workflow. This tool analyses whether there are any inverted surface normals, bad edges, bad contours, planar holes, shells, noise shells, overlapping triangles or intersecting triangles. In case any of these are detected, they can be solved within the software. After the required alterations, each 3D model was exported as a new STL file, ready to be used for subsequent steps.

4.7. Landmark Localization

4.7.1. Overview landmarks

Per definition, the alpha angle is measured as the angle between the **femoral neck axis** and the line drawn from the **femoral head center** to the **point (P')** at which the femoral head laterally exceeds the best fit circle. Thus, to automatically compute the alpha angle, the following landmarks should be identified:

1. **The femoral head center**: It is found by automatically isolating part of the femoral head as region of interest and fitting a sphere to it. The center of the fitted sphere approximates the femoral head center.
2. **The femoral neck axis**: It is found by connecting the femoral head center to the femoral neck center. The femoral neck center is found by dividing the femoral neck in a set of slices. The centroid of the slice with the smallest surface area approximates **the femoral neck center**.

   Subsequent to landmark localization, radial reformatting is performed in which the locations of the radial sections in which the alpha angles will be measured are obtained. To standardize this approach, each 3D model was aligned within the coordinate system based on their localized landmarks. In addition to the femoral head center and the femoral neck axis, the femoral shaft axis served as an important landmark for this standardized alignment. Therefore, locating the femoral shaft axis is part of the landmark localisation step.
3. **The femoral shaft axis**: It was found by connecting two points: shaft center 1 (SC1) and shaft center 2 (SC2). Extending the femoral neck axis towards the femoral shaft to twice its length provided point SC1. SC1 is the most distal point on this extended femoral neck axis, roughly in the middle of the femoral shaft at the point at which the femoral neck transitions into the femoral shaft. SC2 was found by dividing the femoral shaft in a set of slices and the centroid of the most distal slice approximates SC2. The rationale behind this approach is further discussed in Section 4.7.3.

   Point P' requires prior execution of radial reformatting and, consequently, will be obtained later in the workflow. Its explanation will be provided in detail in Section 5.3.2.

4.7.2. The Femoral Head Center

The femoral head center was found by automatic isolation of part of the femoral head as ROI with subsequent spherical fitting to this ROI. The center of the fitted sphere approximates the femoral head center.

Isolation of region of interest

Considering the entire femoral head would ideally provide the most accurate spherical representation, but the presence of a cam morphology can influence the positioning of the femoral head center and result in fitted spheres with an overestimated radius. Thus, any site where a cam morphology is present was excluded from the spherical fitting process to ensure accuracy of femoral head center localization and quantification of the radius of the femoral head. The ideal ROI is depicted in Figure 4.5.

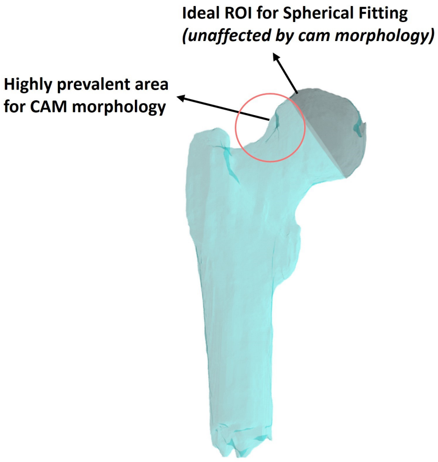

Figure 4.5: Ideal ROI for spherical fitting: the superomedial part of the femoral head, unaffected by any cam morphology. The red circle indicates a region highly prevalent for CAM morphology

To obtain the coordinates of this specific ROI, the 3D hip models first have to be aligned within the coordinate system in a standardized manner. This alignment requires prior landmark localization to relate the position of the 3D hip model within the MRI-based coordinate system. To initialize this landmark localization, the standardized position of the x, y and z axes within the cartesian coordinate system and the centroids of the 3D hip models were used (Figure 4.6). This approach enabled automated isolation of the *anteromedial* part of the femoral head from the mesh, as the isolation of the ideal ROI was not yet feasible.

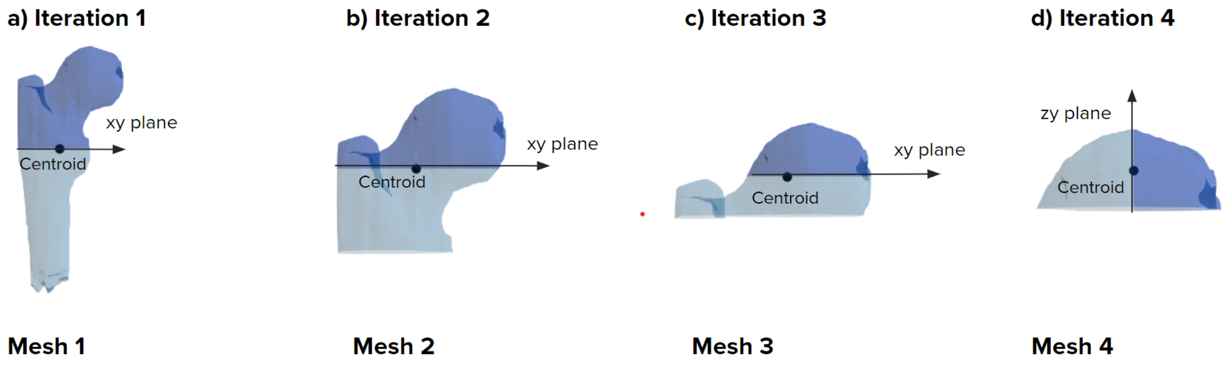

Figure 4.6: Iterative planar cutting of the femoral 3D model. a) Planar cutting using the centroid of the original mesh and the xy plane. b) Planar cutting using the centroid of mesh 1 and the xy plane. c) Planar cutting using the centroid of mesh 2 and the xy plane. d) Planar cutting using the centroid of mesh 3 and the zy plane.

An iterative planar cutting algorithm was applied that cuts the mesh four times using different planes. The first three cuts were performed to remove the distal part of the femur and the last cut was performed to remove part of the femoral head that might have a cam morphology (Figure 4.6). The first cutting plane was defined by the vector normal to the z-axis (the xy plane). The point at which the plane cuts the mesh was defined by the centroid of the original mesh. This initial planar cut resulted in mesh 1 (Figure 4.6 a). The second cutting plane was defined by the centroid of mesh 1 and the xy plane, resulting in mesh 2 (Figure 4.6 b). The third cut was defined by the centroid of mesh 2 and the xy plane, resulting in mesh 3 (Figure 4.6 c). The final fourth cut was defined by the centroid of mesh 3 and the vector normal to the x-axis (the zy-plane). Depending on whether the hip was left-oriented or right-oriented, a positive or negative vector normal to the x-axis was used. This resulted in mesh 4, representing the isolated superomedial part of the femoral head (Figure 4.6 d).

Least square spherical fitting
To find the location of the femoral head center , a sphere was fit to the data points corresponding to the isolated superomedial part of the femoral head (Figure 4.6 d). This geometrical shape was chosen as it is the best approximation of the shape of the femoral head.[27] To find the most accurate fit, the least square fitting (LSF) method was used. The LSF algorithm was chosen instead of the Random Sample Consensus (RANSAC) algorithm, an alternative geometrical fitting algorithm, because the RANSAC algorithm requires manual threshold tuning, thus making the approach semi-automatic instead of fully automatic. The idea behind LSF is to minimize the sum of the squared distances between the actual data points (the points belonging to the femoral head) and the predicted values of the sphere.

The general equation of a sphere is:

$$(x - x0)^2 + (y - y0)^2 + (z - z0)^2 = r^2 \tag{4.1}$$

The center of the sphere is represented by *(x0, y0, z0)* and the radius of the sphere by *r*. Rearrangement leads to the following equation:

$$x^2 + y^2 + z^2 = 2xx0 + 2yy0 + 2zz0 + r^2 - x0^2 - y0^2 - z0^2 \tag{4.2}$$

This enables expression of the equation in matrix form in which $\vec{f}$ is a linear combination of A and $\vec{c}$. In this vector/matrix expression, (xi,yi,zi) represents the first datapunt whereas (xn,yn,zn) represents the last data point of the dataset.[28]

$$\vec{f} = \begin{bmatrix} xi^2 + yi^2 + zi^2 \\ xi + 1^2 + yi + 1^2 + zi + 1^2 \\ \dots \\ \dots \\ xn^2 + yn^2 + zn^2 \end{bmatrix} \tag{4.3}$$

$$A = \begin{bmatrix} 2xi & 2xi & 2zi & 1 \\ 2xi + 1 & 2yi + 1 & 2zi + 1 & 1 \\ & \dots & & \\ & \dots & & \\ 2xn & 2yn & 2zn & 1 \end{bmatrix} \tag{4.4}$$

$$\vec{c} = \begin{bmatrix} x0 \\ y0 \\ z0 \\ r^2 - x0^2 - y0^2 - z0^2 \end{bmatrix} \tag{4.5}$$

To find the center and radius, denoted in vector $\vec{c}$, the following equation has to be solved:

$$\vec{f} = A\vec{c} \tag{4.6}$$

When there is a perfect fit, meaning that every point of the femoral head is localized exactly on the sphere, then there is a solution to the equation.[29] As the femoral head is not perfectly spherical, this is not the case. Therefore $\vec{c}$ will be the least square solution that minimizes the least square distance.
To perform least square fitting, the pointcloud of mesh 4 (the superomedial part of the femoral head) was extracted from the mesh (Figure 4.6 d). This pointcloud was used as input for the spherical LSF (Figure 4.7).

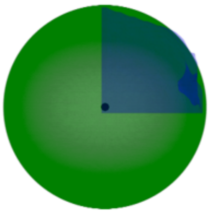

Figure 4.7: Least square spherical fitting of a sphere to the isolated superomedial part of the femoral head. The blue part represents the mesh and the green part the sphere that is fitted to the mesh using the least square fitting algorithm.

4.7.3. The Femoral Neck Axis and The Femoral Shaft Axis

The femoral neck axis was found by connecting the femoral head center to the femoral neck center. The femoral neck center is defined as the center of the femoral neck isthmus. To detect the femoral neck isthmus, the 3D hip models were sliced into equally spaced parts using planar cuts along a predefined axis. This slicing operation required definition of the slicing direction and the slicing range. The latter defines the starting and ending point of the slicing procedure and the thickness of each slice. For each obtained slice, the surface area and the centroid were subsequently computed. The centroid of the slice with the smallest surface provided the femoral neck center (Figure 4.8).

The femoral shaft axis was approximated by connecting two points: shaft center 1 (SC1) and shaft center 2 (SC2) (Figure 4.8). Extending the femoral neck axis towards the femoral shaft to twice its length provided point SC1. SC1 is the most distal point on this extended femoral neck axis. The factor of two was an arbitrarily chosen number to roughly approximate a proximal point in the middle of the femoral shaft at the point at which the femoral neck transitions into the femoral shaft. The positioning of point SC1 on the femoral neck axis ensured the intersection of the femoral neck axis and resulting femoral shaft axis (Figure 4.8).

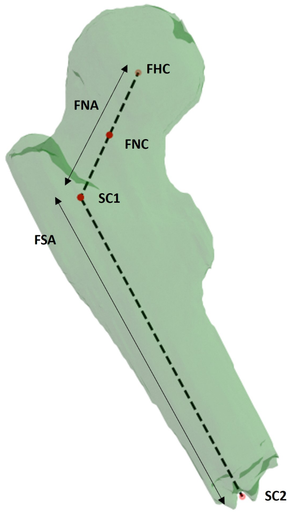

Figure 4.8: Anatomical landmarks on the proximal femur mesh. **FHC** = Femoral Head Center, **NC** = Neck Center, **FNA** = Femoral Neck Axis, **SC1** = Shaft Centroid 1, **SC2** = Shaft Centroid 2, **FSA** = Femoral Shaft Axis.

Definition of the slicing direction
To obtain slices parallel to the femoral neck axis and femoral shaft axis, the specified slicing direction should also be roughly parallel to the direction of the axis to be found. For the femoral shaft axis, the z-axis is roughly parallel as depicted in Figure 4.9. But for the femoral neck axis, no principal axis within the coordinate system was roughly parallel (Figure 4.9). Therefore, an initial rough alignment of the femoral neck with the negative z-axis was required.

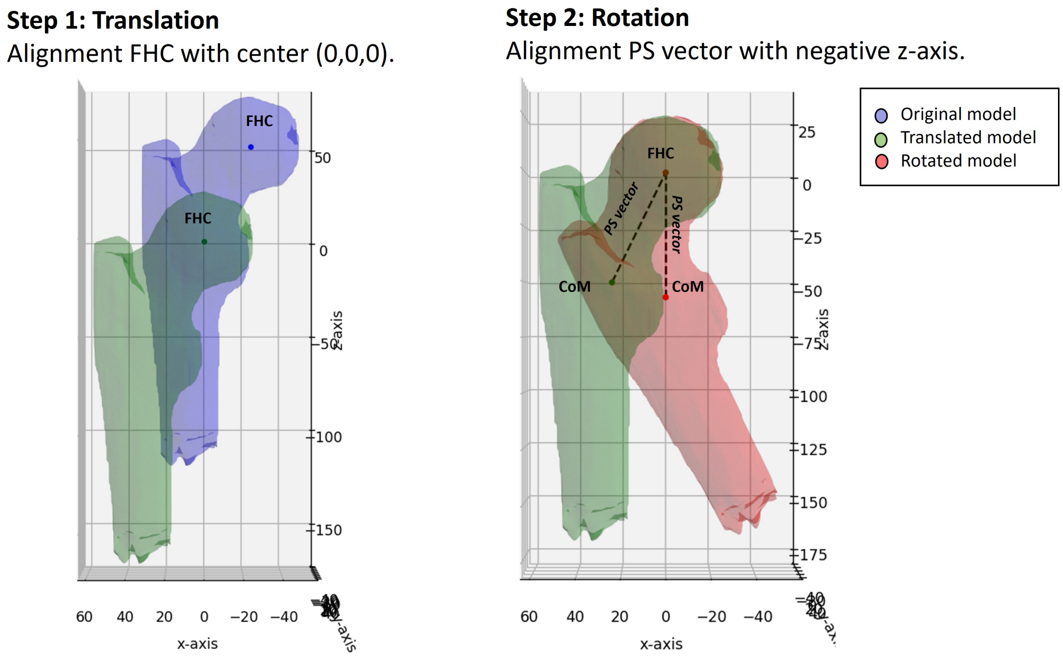
Step 1: Translation
Alignment FHC with center (0,0,0).

Step 2: Rotation
Alignment PS vector with negative z-axis.

Figure 4.9: Left: Alignment of the femoral head center (FHC) with the center of the coordinate system (0,0,0) by means of translation. **Right:** Alignment of the patient specific (PS) vector with the negative z-axis by means of rotation.

The total alignment includes a translation and a rotation. First the femoral head center was set as the center of the coordinate system by means of translation (0,0,0) (Figure 4.9 - Left) to simplify the specification of the slicing range. Second, a patient specific vector was defined using two points: (1) the femoral head center, and (2) the center of mass of the mesh. This patient specific vector was then aligned with the negative z-axis in the cartesian coordinate system by means of rotation (Figure 4.9 - Right).

The matrix below describes the transformation that was applied to each 3D model. Theta describes the rotation angle for the (negative) z-axis alignment and (Tx,Ty,Tz) the translation to align the femoral head center with the origin. These values are specific per 3D model.

$$\vec{Rz} = \begin{bmatrix} cos(theta) & -sin(theta) & Tx \\ sin(theta) & cos(theta) & Ty \\ 0 & 0 & Tz \end{bmatrix} \tag{4.7}$$

Definition of the slicing range

To determine the slicing range (the start and end point of the slicing operation), the height of the 3D model was obtained by setting a bounding box that surrounds the mesh. For the femoral shaft axis, the model was sliced from z = 0 until z = z(max) as shown in Figure 4.10 - Left. For the femoral neck axis, the model was sliced from z = 0 until z = 1/3*z(max) as shown in Figure 4.10 - Right. This smaller slicing range was chosen to ensure that no distal parts of the 3D model (the shaft) were included. Since the femoral neck axis detection approach is based on identification of the slice with the smallest surface area, including parts of the 3D hip model with a smaller area than the isthmus of the femoral neck would compromise the accuracy of femoral neck center detection.

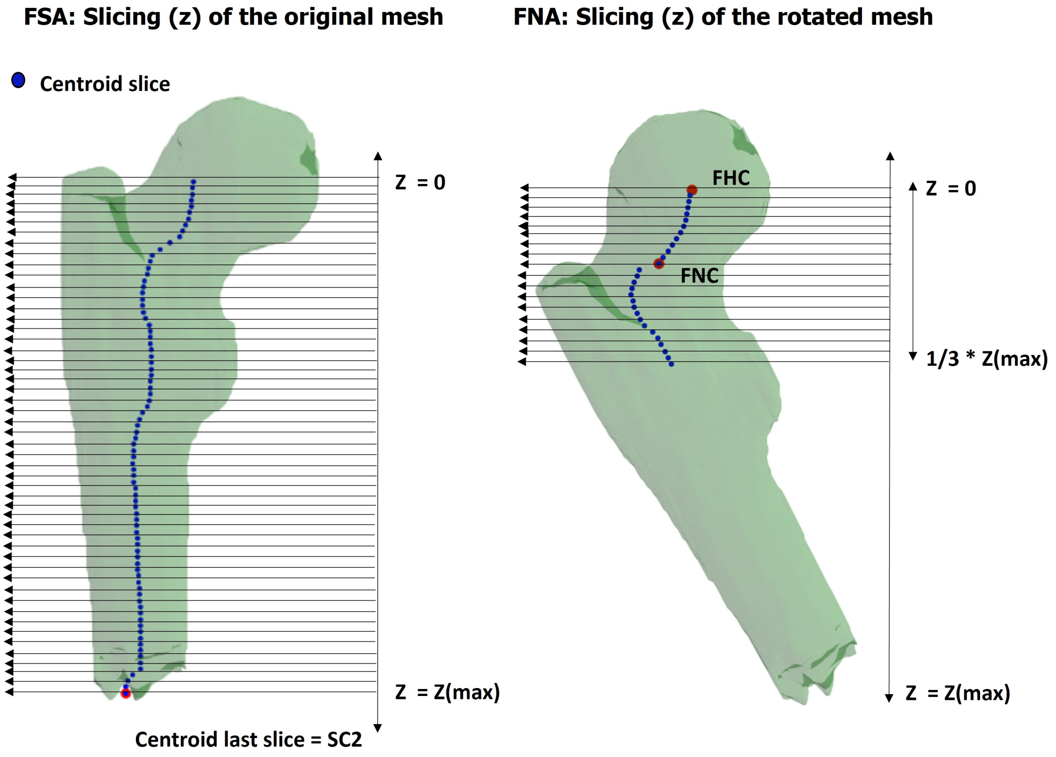

Figure 4.10: **Left:** Slicing the original mesh with vectors projected from the z-axis, starting from the z=0 until z= z(max) of the bounding box surrounding the original mesh. The blue dots represent the centroids of each slice. The end of the shaft axis (SC2) is found as the centroid of the last slice (red dot). **Right:** Slicing the rotated mesh with vectors projected from the z-axis, starting from the femoral head center (FHC) down down until 1/3*z(max). The blue dots represent the centroids of each slice. The femoral neck center (FNC) (red dot) is the centroid of the slice with the smallest area.

Centroid and surface area computation

For each slice, the surface area and centroid were determined. The centroid of the slice with the smallest surface area in the rotated 3D model approximated the femoral neck center. The centroid of the last slice in the translated 3D model provided a reference point SC2, specifically the end of the shaft axis. Figure 4.10 shows one of the 3D hip joint models with its automatically detected centroids in each slice (blue dots) and its centers of interest (red dots).

With the localization of the femoral neck center, SC1 and SC2, the femoral neck axis was formed by connecting the femoral head center and the femoral neck center and the femoral shaft axis was formed by connecting SC1 and SC2. In Figure 4.8 the detected landmarks and axes are shown.

4.8. Radial reformatting

To enable the computation of alpha angles in 3D space, a division of the femoral head into 12 radial sections was implemented. These radial sections were centered around the femoral neck axis, with each section spanning an angular separation of 30 degrees from its adjacent radial section. This angular division follows a clockwise hour pattern, reminiscent of a clock's orientation. For instance, the superior part of the femoral head corresponds to the 12 o'clock position, while the inferior part aligns with the 6 o'clock position (Figure 4.11). This radial segmentation scheme facilitates the localization and analysis of specific regions within the femoral head.

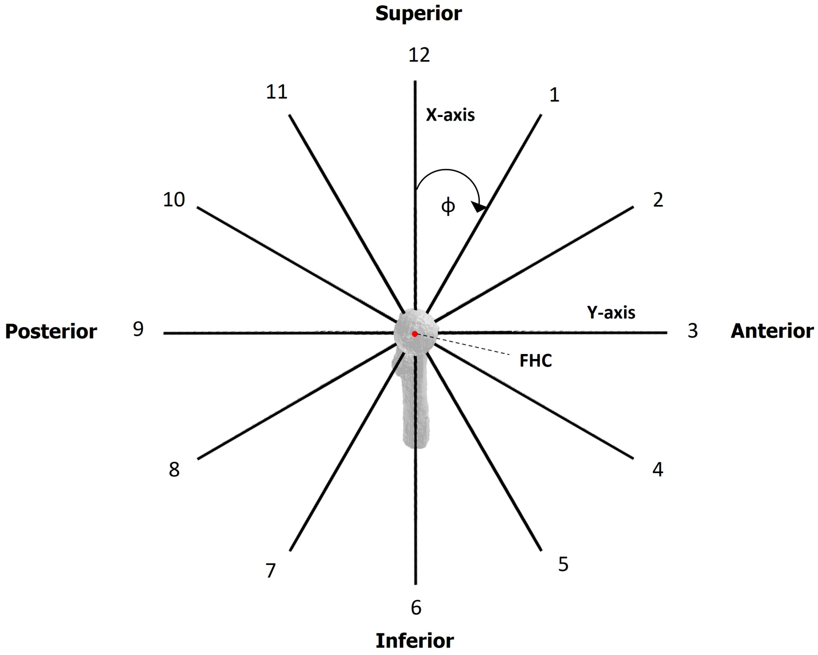

Figure 4.11: Division of the femoral head center into radial sections. All 12 radial sections correspond to the 12 clock positions centered around the femoral head. The location of each radial section is expressed as the azimuth angle (φ).**FHC** = Femoral Head Center.

4.8.1. Standardized alignment

In order to establish a consistent correlation between automatic alpha angle measurements and the corresponding radial sections used for manual measurements, a standardization process was implemented for the positioning of 12 radial sections. This involved aligning the 3D models based on pre-defined hip-specific landmarks, namely the femoral neck axis and the femoral shaft axis. The alignment procedure entailed two rotations: aligning the femoral neck axis with the negative z-axis and aligning the femoral shaft axis with the negative x-axis in a 2D plane (Figure 4.12). The latter adjustment was necessary to account for inter-individual variations in hip retroversion. By applying these rotations, the 3D models were brought into a standardized alignment, ensuring consistent orientation for subsequent analysis and measurement procedures.

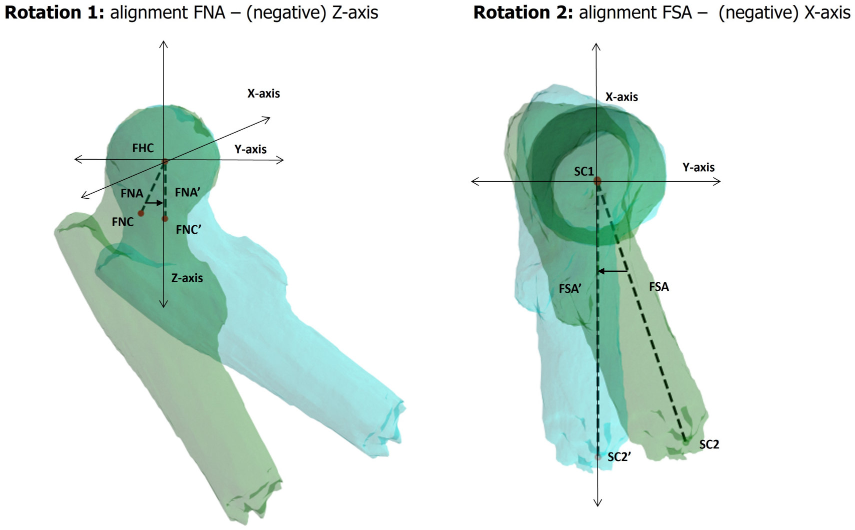

Rotation 1: alignment FNA – (negative) Z-axis

Rotation 2: alignment FSA – (negative) X-axis

Figure 4.12: **Left:** alignment of the femoral neck axis with the (negative) z-axis by means of rotation. **Right:** alignment of the femoral shaft axis with the (negative) x-axis by means of rotation.**FHC** = Femoral Head Center, **FNC** = Femoral Neck Center, **FNC'** = Rotated Femoral Neck Center, **FNA** = Femoral Neck Axis, **FNA'** = Rotated Femoral Neck Axis, **SC1** = Shaft Centroid 1, **SC2** = Shaft Centroid 2, **SC2'** = Rotated Shaft Centroid, **FSA** = Femoral Shaft Axis, **FSA'** = rotated Femoral Shaft Axis.

4.8.2. Spherical coordinate system

The establishment of a standardized alignment allowed for the implementation of a spherical coordinate system within each 3D hip model, with the femoral head center serving as the origin and the femoral neck axis aligned as the negative z-axis (Figure 4.13). In this spherical coordinate system, the position of a specific point in 3D space is determined by three parameters: the distance from the femoral head center, denoted as *r*; the inclination angle, represented by θ; and the azimuth angle, indicated as φ. The transformation from a cartesian coordinate system (x,y,z) to a spherical coordinate system (r,θ,φ) facilitates definition of the radial sections and correlation with manual radial sections during the validation of the alpha angle measurements. Additionally, the angular expression of locations within the spherical coordinate system facilitate alpha angle computation, performed subsequently to this automatic radial reformatting.

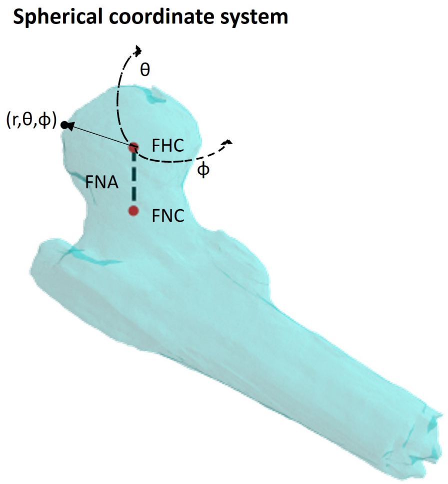

Spherical coordinate system

Figure 4.13: Set-up of the spherical coordinate system, based on the standardized alignment of each 3D hip model. **FHC** = Femoral Head Center, **FNC** = Femoral Neck Center, **FNA** = Femoral Neck Axis, **r** = distance fo origin (FHC), **θ** = Inclination angle, **φ** = Azimuth angle.

4.9. Alpha angle computation

With the set up of a spherical coordinate coordinate system, the next step within the workflow was to locate point P’ within each radial section. It was found by locating the smallest inclination angle θ at which the radial distance from the femoral head center to the bone surface exceeds the fitted spherical radius R (Figure 4.14). To locate point P’, first the fitted spherical radius R has to be found. Secondly, radial distances *r* from the femoral head center to the bone with their corresponding locations (inclination angle θ) for each radial section have to be obtained.

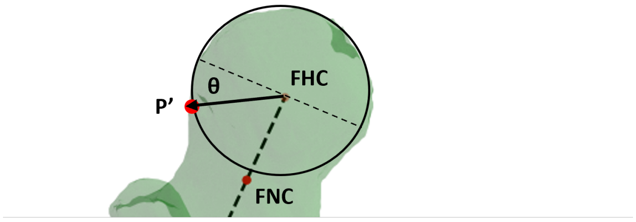

Figure 4.14: **Left:** Localisation of point P’, the smallest inclination angle θ at which the radial distance from the femoral head center to the bone surface exceeds the fitted spherical radius R. **FHC** = Femoral Head Center, **FNC** = Femoral Neck Center.

4.9.1. Fitted spherical radius R

Optimization of the ROI for LSF

To accurately determine the radius R of the femoral head, an additional LSF was performed. While the initial sphere fitting procedure captured the femoral head center, it did not provide the most precise representation of its radius as the sphere was fitted to the anteromedial part of the femoral head, which accounts for approximately 25 percent of the entire femoral head. An optimization of the ROI for fitting was carried out using landmarks that were obtained previously in the workflow. More specifically, a plane bisecting the femoral head was defined based on the positions of the femoral head center and the femoral neck axis. This approach allowed for the extension of the ROI beyond the anteromedial region, accounting for approximately 50 percent of the entire femoral head (Figure 4.15). With the expanded ROI, the newly fitted sphere provided radius R (Figure 4.15).

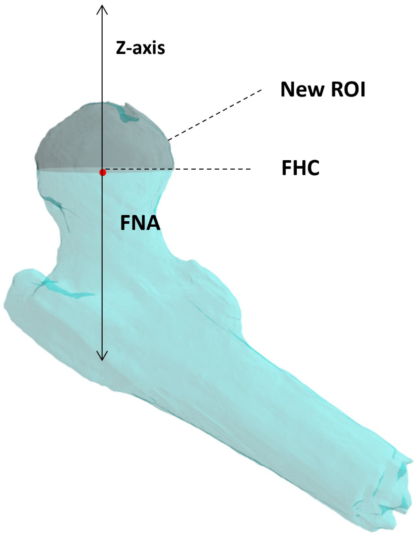

Figure 4.15: Planar cutting of the aligned mesh using the FHC and the FNA, aligned with the z-axis within the coordinate system. The planar cut results in an extended region of interest (grey), used for spherical fitting. **FHC** = Femoral Head Center, **FNA** = Femoral Neck Axis

Radial section-specific spherical fitting

Figure 4.16 shows the contour of the superior portion of the femoral head for 12 radial positions of one of the 3D models in this study. This figure highlights the already known fact that the femoral head is not perfectly round as is assumed in preceding steps in the workflow when performing least square spherical fitting. The radius of certain 2D radial segments may be smaller than that of others, suggesting that radial specific spherical fitting would result greater precision of the radius than one sphere that approximates all radial sections. Moreover, this is in accordance with the Nötzli method. In manual alpha angle assessments, the best fit circle is drawn for each radial section specific as well [7].

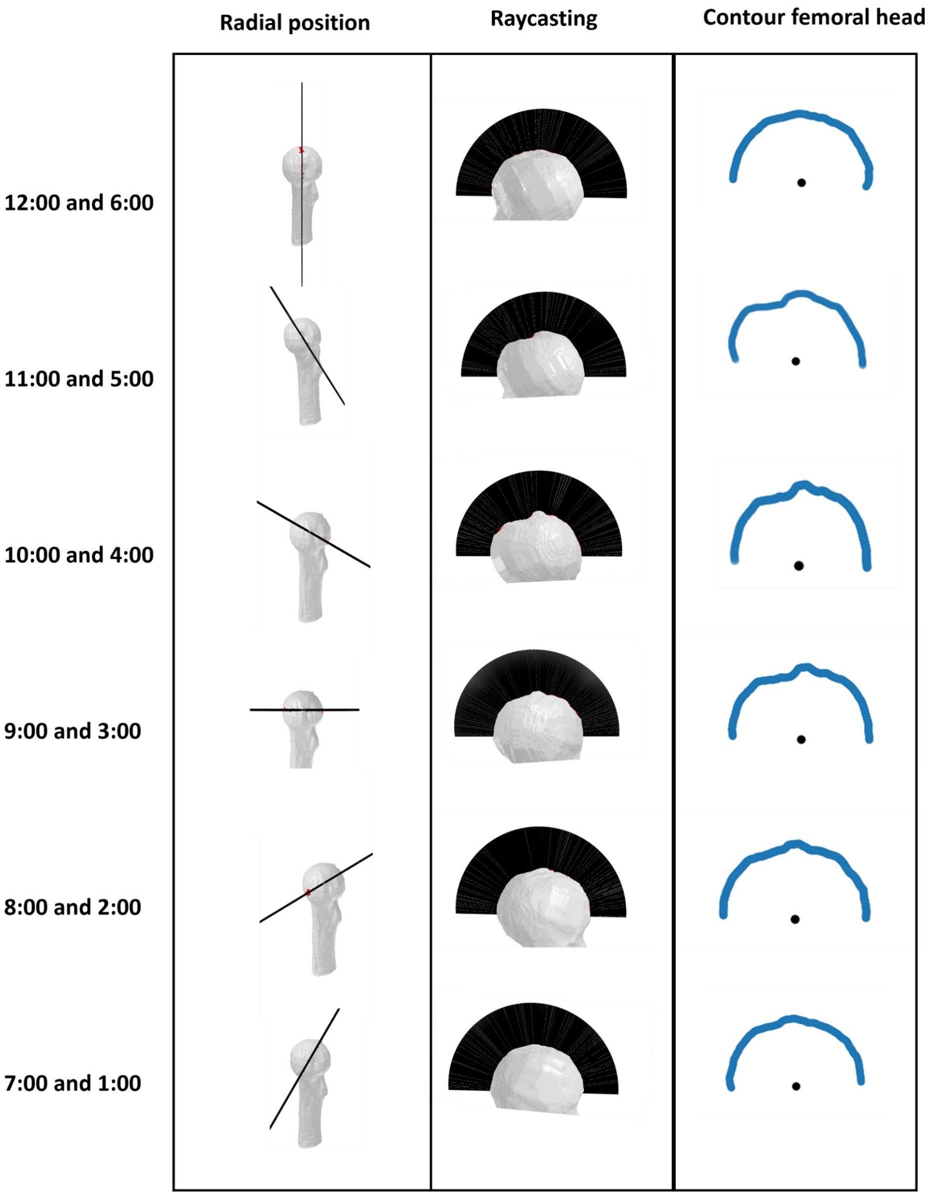

Figure 4.16: Application of the raycasting algorithm (middle) to obtain the points corresponding to the superior portion of the femoral head (right) for each radial plane (left).

A novel radial section-specific spherical fitting method was developed utilizing the ray casting algorithm, which determines whether a given point lies inside or outside a 3D model. The algorithm projects directional vectors T(θ,φ) from the center of the femoral head towards the surface of the 3D mesh. These vectors are referred to as rays, and if they intersect with the 3D mesh surface, the coordinates of the point of intersection can be recorded along with the distance traveled by the rays.

The raycasting algorithm was used to sample the location of points along the superior portion of the femoral head for each radial position (Figure 4.16). These points, representing the superior contour of the femoral head were subsequently used to fit a sphere using the LSF algorithm. This provided 12 radial section-specific radii.

Model Specific Factor

Figure 4.16 depicts that there is variation in radius among radial planes, but also variation within each radial plane. When the workflow aims to detect point P' by searching for the locations at which the radial distance from the femoral head center to the bone surface exceeds the fitted spherical radius R, these internal radial variations can strongly affect the accuracy of this detection. To account for this variation, the threshold (the fitted spherical radius R) was altered by multiplication of the radius R by a model specific factor (MSF).

The model specific factor was calculated with the following equation:

$$MSF = \frac{\frac{1}{n}\sum_{i=1}^{n} x_i + Rsphere}{Rsphere} \tag{4.8}$$

The distance between each point of the pointcloud of the region of interest (xi) and the fitted sphere was determined. The average of these distances and the radius of the fitted sphere were used to calculate the model specific factor. For the eight 3D hip models in this thesis, the model specific factor ranged from 1.02 to 1.03. Because of the empirical nature of this model specific factor, alpha angles with and without multiplication by the model specific factor were computed to research its effect.

4.9.2. Radial distances and locations

To obtain the radial distances for all points within 12 radial sections from the inferior part of the femoral head, a ray vector matrix was created in the spherical coordinate system. This matrix, consisting of 90 x 12 (θ,φ) elements, specifies the direction of the rays in the raycasting algorithm. The 90 rows represented inclination angles and the 12 columns represented azimuth angles corresponding to the radial sections centered around the femoral head. An example of this is shown in Figure 4.17 for one of the radial sections. The rays were cast from the femoral head center and intersected with the 3D mesh, providing the coordinates and radial distances for each element (r,θ,φ) within the 90 x 12 matrix.

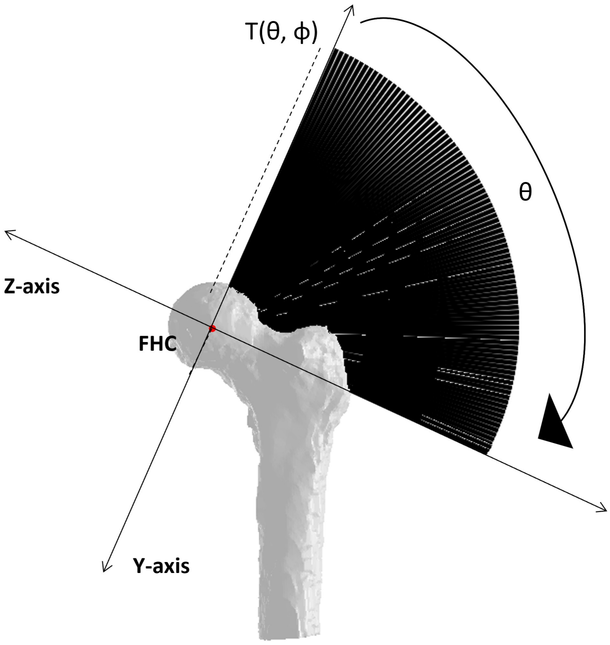

Figure 4.17: Raycasting applied for 90 inclination angles θ at the lateral side of the 3D hip model for one radial section φ, aiming to obtain locations and distances with respect to the femoral head center from each point of the 3D surface mesh that intersects with the rays.

4.9.3. Alpha angle computation

The alpha angle was computed for 12 clockwise positions, sampled along the radial axis. This corresponds to φ = 0°, 30°, 60°, 90°, 120°, 150°, 180°, 210°, 240°, 270°, 300°, 330°(Figure 4.11). The alpha angle was computed by performing the following subtraction: 90 °- the smallest inclination angle θ at which the radial distance from the femoral head center (FHC) to the bone surface exceeds the fitted spherical radius R by a specified threshold value using the model specific factor (Figure 4.14 and Figure 4.17).

Outlier Detection

The performance of semi-automated alpha angle computation can be affected by irregularities on the surface of the 3D model of the hip. The surface of the femoral head is not entirely smooth by nature and can have irregularities due to manual segmentation errors. An irregularity such as a bump on the surface can result in the algorithm recognizing it as the location where the cam morphology starts, as it exceeds the threshold value.

To detect these outliers, the alpha angle algorithm was optimized by examining subsequent inclination angles. Specifically, the alpha angle was calculated as the smallest inclination angle θ at which the radial distance from the femoral head center to the bone surface exceeds the fitted spherical radius R by a specified threshold value. But with the condition that an x number of subsequent inclination angles θ also exceed the threshold value (Figure 4.18). In collaboration with an experienced sports doctor, who took into account the variety of cam morphology observed in clinical practice, a value of n = 1, 5, 10 and 20 subsequent inclination angles were considered to see whether this would be a reliable outlier detection method. Similarly to the model specific factor, due to the empirical nature of this outlier detection method, validation of the semi-automated workflow included comparison of the different number of subsequent inclination angles used during outlier detection and comparison of alpha angle computation with no outlier detection at all.

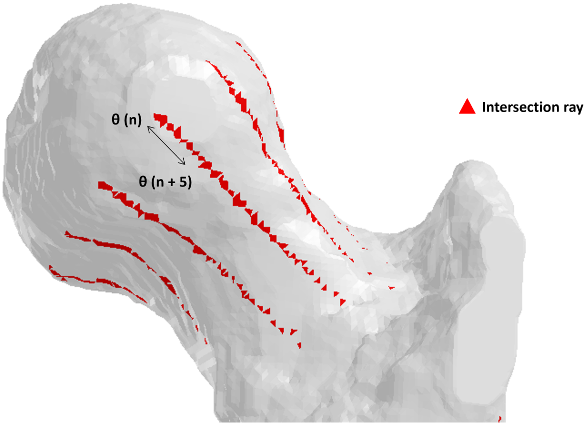

Figure 4.18: The red triangles represent the positions at which the rays intersected with the 3D model for 12 radial positions. The condition of N + 5 subsequent inclination angles is illustrated to visualize to what extent extruding surfaces are minimally detected.

4.10. Validation

To validate the reliability of the developed workflow, alpha angle measurements computed by the semi-automated workflow were compared to alpha angles measured manually by an experienced MSK radiologist using Picture Archiving and Communication System (PACS) software. Both a quantitative and a qualitative analysis was conducted.

4.10.1. Qualitative Validation

The qualitative analysis of the workflow included (1) visual inspection of landmark localisation (femoral head and neck center), (2) visual evaluation of the fitted spheres and (3) visual evaluation of the correspondence between the femoral head morphology of the 3D hip models and the measured and computed exceeding alpha angles. This qualitative evaluation of cam morphology of the 3D hip models was performed in collaboration with an experienced sports doctor.

4.10.2. Quantitative Validation

The workflow includes automatic generation of an excel file that obtains the 12 computed alpha angles. Six radial positions were selected for the quantitative validation of alpha angle measurements, with four measurements being taken in the antero-lateral region of the femoral head-neck (FHN) region at 12:00, 1:00, 2:00, and 3:00, and two measurements at 6:00 and 9:00 in the clockwise direction as depicted in Figure 4.11. These positions were chosen based on the prevalence of the location of cam morphology in the FHN region. Previous studies have demonstrated that when stratified by location, over 90% of the cam morphologies are located in the antero-superior quadrant, which corresponds to the 12:00 until 3:00 clock positions.[30] By focusing on these regions, the goal was to evaluate the performance of the semi-automated measurement method in the most frequently affected areas. In addition, the 6:00 and 9:00 positions were included to examine non-prevalent regions of cam morphology and obtain a circumferential view, which provides a more comprehensive assessment of the methods reliability.

Manual Radial Reformatting

Before alpha angles were manually measured, radial reformatting was performed to be able to correlate a manual alpha angle measurement in a specific radial section to an automatic alpha angle computed in that same specific radial section. Because the existent radial series of the ZTE images of the Feyenoord cohort were not centered correctly around the femoral neck axis, multiplanar reconstruction was performed manually to radially reformat the images. This process involved two steps. First the femoral neck axis was centered correctly as radial axis and the femoral shaft axis was also aligned to correct for retroversion. This alignment was similar to the alignment performed in the workflow. Second, the angular axis was aligned at the six radial clock positions. The angular axis alignment was achieved through manual measurement using an angular measuring tool in the PACS software. Figure 4.19 illustrates an example of the manual process of radially reformatting the images and the manual locating of the 1:00 radial plane. To facilitate interpretation, the contrast of the ZTE images was inverted to obtain pseudo-CT like images with bone depicted as white pixels and soft tissue as grey pixels.

1. Alignment of the radial axis

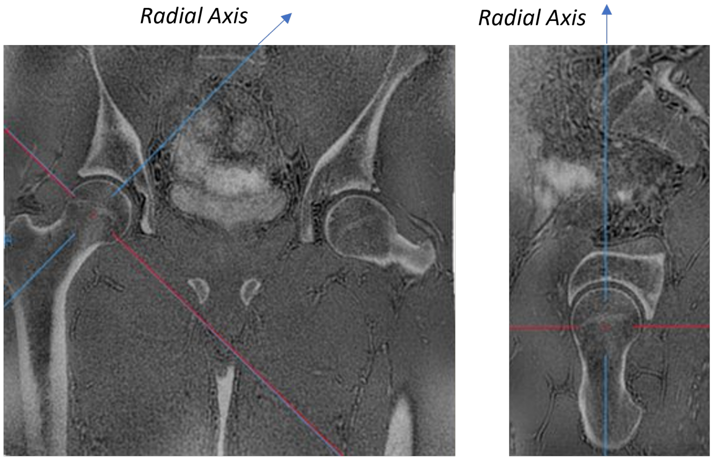

2. Alignment of the angular axis

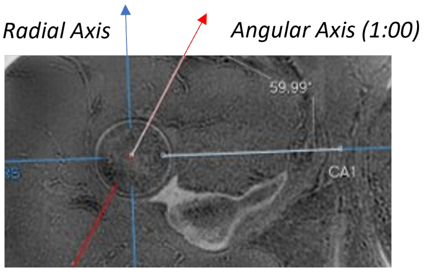

Figure 4.19: Manual multiplanar radial reformatting on the contrast-inverted ZTE images. First the femoral neck axis (FNA) is centered as the radial axis (top left) and aligned in 2D with the femoral shaft axis (top right) . Second, the radial position is chosen by manually rotating the angular axis (red line) around the femoral head using an angular measurement tool in PACS.

Manual Alpha Angle Measurement

Manual alpha angle measurements were performed using the method described by *Nötzli et al.* [7] First, a circle was drawn that best fits the femoral head on the radially reformatted image. The center of the circle approximates the femoral head center which can be used to draw the femoral neck axis when connected to the femoral neck center, which is the center of the isthmus of the femoral neck (Figure 4.20). Also, a line was drawn by the MSK radiologist from the femoral head center to the point (P') at which the femoral head laterally exceeds the best fit circle (Figure 4.20). The alpha angle was then measured as the angle between P' - femoral head center and the femoral neck axis.

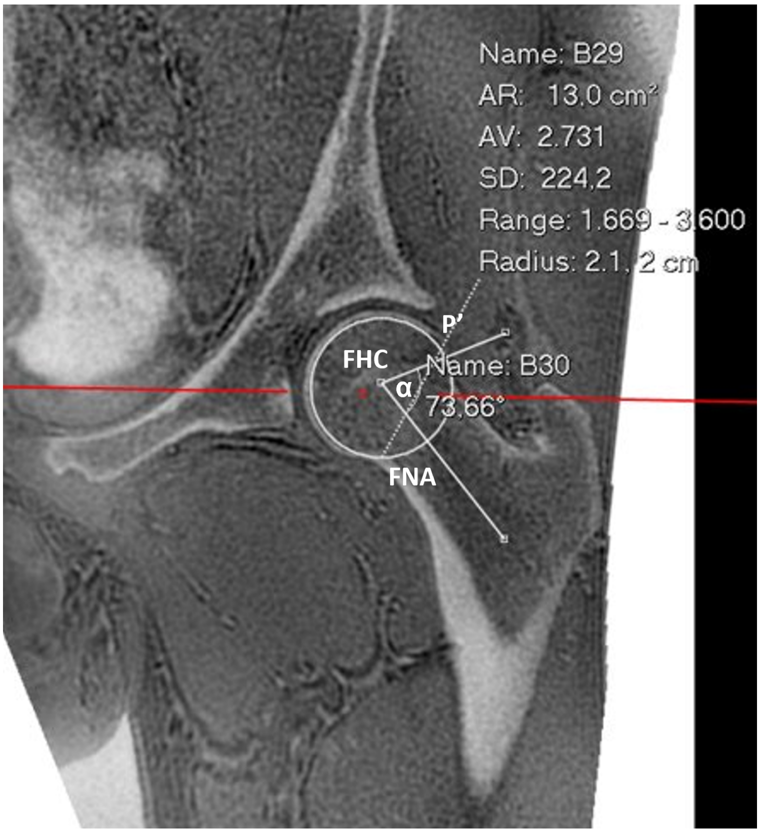

Figure 4.20: Manual alpha angle measurement. **FHC** = Femoral Head Center. **FNA** = Femoral Neck Axis. **P'** = The point where the bone leaves the fitted circle around the femoral head. **α** = the alpha angle, the angle between the line drawn from FHC to P'and the FNA.

4.10.3. Statistical Analysis

The statistical analysis in this study was performed using Python version 3.9.16 [15], Numpy version 1.24.2 [31], and Pingouin version 0.5.3 [32]. For comparison of the radii obtained manually, with the automated radial section-specific approach, a two-sided two-sample t-test with equal variances was conducted to determine if there was any significant difference in mean radii. For comparison of the manual radii and automated radial-section-specific approach with the radial section-aspecific approach, a two-sided one-sample t-test was conducted. For the alpa angle, two validation metrics were calculated: the mean absolute difference (MAD) and the intraclass correlation coefficient (ICC). These metrics were used to assess the inter-observer agreement and reliability of the semi-automated alpha angle measurements in comparison to manual measurements.

The ICC is available in ten different forms, which vary based on the model used (e.g., one way random effects, two way random effects, two way mixed effects), type (e.g., single rater, mean multiple raters), and definition (e.g., absolute agreement, consistency). In this study, a two way mixed effect model was chosen as the same specific set of raters was used for alpha angle measurements in all models. A single rater type was selected, and absolute agreement was prioritized over consistency.[33]

The ICC values indicate the level of agreement, where ICC values above 0.9 indicate excellent agreement, values between <0.9 and >=0.75 indicate good agreement, values between >0.5 and <0.75 indicate moderate agreement, and values below 0.5 indicate poor agreement. [33] Bland-Altman plots were generated using the Matplotlib library version 3.7.1 [34] to show the relationship between the manual and semi-automated alpha angle measurements.

5

Results

In this section, first the outcomes of the questionnaire are presented (Section 5.1). Second, a qualitative evaluation of the workflow is described (Section 5.2) and last, this section provides a qualitative evaluation of the workflow that was developed (Section 5.3).

5.1. Inventory of requirements

The questionnaire was filled in anonymously by 6 radiologists, 5 sports physicians and 4 orthopedic surgeons. These clinicians see approximately 30-100 patients per month with hip/groin complaints. Approximately one third of these patients is diagnosed with FAIS.

5.1.1. Conventional use of imaging

Figure 5.1 shows the imaging modalities that are used to assess the presence of FAIS in patients among different specialisms (radiologists, sports doctors and orthopedic surgeons). As can be seen in Figure 5.1, a wide variety of imaging techniques is used, with the AP X-ray view being the most frequently used across all specializations.

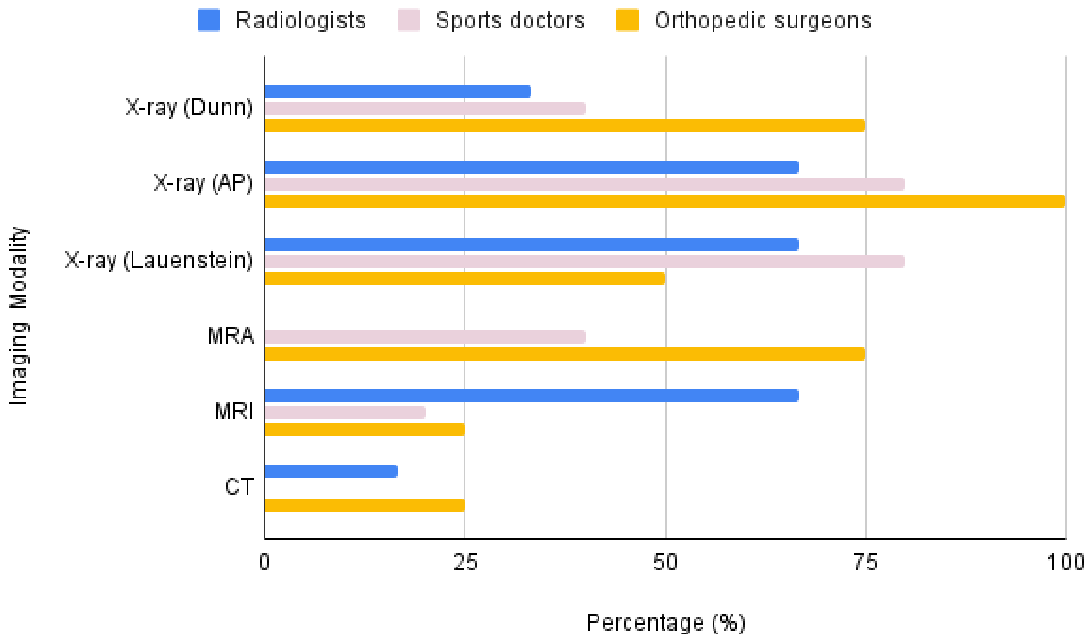

Figure 5.1: The imaging modalities used by radiologists, sports doctors and orthopedic surgeons for diagnosis of CAM morphology.

Figure 5.2 shows whether clinicians use imaging qualitatively, quantitatively or both. All clinicians (100%) use imaging to qualitatively assess the morphology of the hip joint. The majority within each specialism additionally performs quantitative measurements, such as the alpha angle. The threshold to diagnose a cam morphology using the alpha angle is 60° for most clinicians, while some clinicians use 55°.

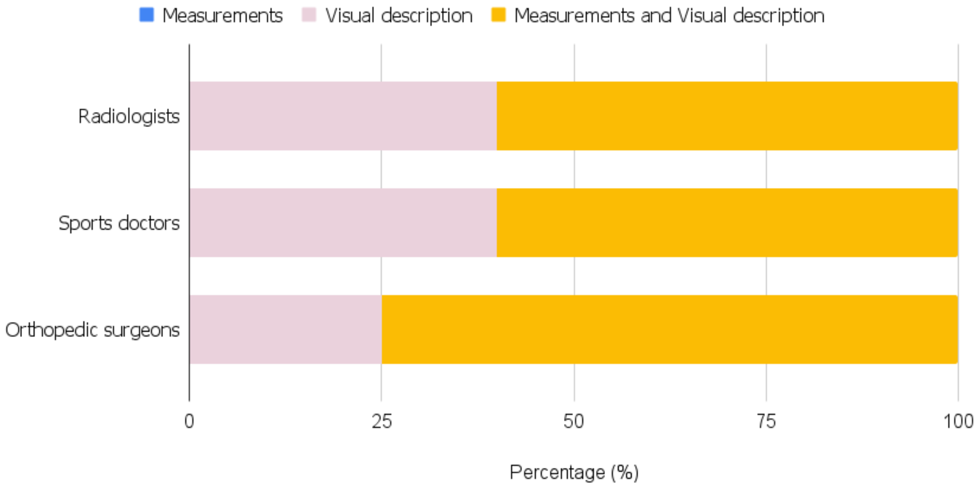

Figure 5.2: The quantitative and/or qualitative use of imaging among radiologists, sports doctors and orthopedic surgeons.

5.1.2. Current software

Since there is already commercial software that performs alpha angle measurements, the participants were asked how they experienced this current software. The majority of radiologists and sports doctors experienced the software as being *'bad'* (60% and 80% respectively), while the majority of orthopedic surgeons rated it as *'average'* (75%).

To better understand the reasons for participants' experiences with the existing commercial software, the questionnaire asked respondents about both positive and negative aspects of the current software and desired features of novel software. The aim of this inquiry was to identify strengths that could be used as requirements for the workflow, as well as weaknesses that could serve as goals for improvement.

Participants reported several strengths and weaknesses of the existing commercial software. Among the strengths were the high level of accuracy for FAIS detection and the software's fast computation. In contrast, participants identified a lack of protocol and user-friendliness as weaknesses. In addition to these concerns, clinicians expressed interest in features such as automatic centering of the femoral head, 3D visualization of areas where bone exceeds the alpha angle threshold, automatic generation of finding reports, and dynamic visualization to show hip impingement during movement.

5.2. Qualitative Evaluation

The small dataset used in this study facilitated an evaluation of the semi-automated workflow through both qualitative and quantitative methods to gain understanding of its strengths and limitations. This qualitative evaluation included an assessment of the spherical fitting (Section 5.2.1), an evaluation of the precise localization of the femoral neck center and femoral head center as landmarks (Section 5.2.2) and an evaluation of the femoral head morphologies for each hip (Section 5.2.3) with a comparison of the correspondence with the quantitative alpha angle measurements (Section 5.2.4).

5.2.1. Least Square Spherical Fitting

Radial section-specific spherical fitting resulted in 12 fitted spheres and radii for each 3D hip model. Radial section-aspecific spherical fitting resulted in one fitted sphere and one radius per 3D hip model that was used for each radial section. Figure 5.3 displays the singular sphere fitted to the femoral head of each 3D hip model. The transparency of the plotted spheres enabled visual assessment of the fitting accuracy. While the fitted spheres matched the superior aspect of the femoral heads, they were relatively oversized for approximating the inferior aspect, especially in regions where the femoral neck had a concave contour. In the right hip of patients 45 and 67, the femoral head's contour was not distinctly visible, and consequently, the fitted sphere did not align closely with the femoral head's surface, as a result of an overestimated radius.

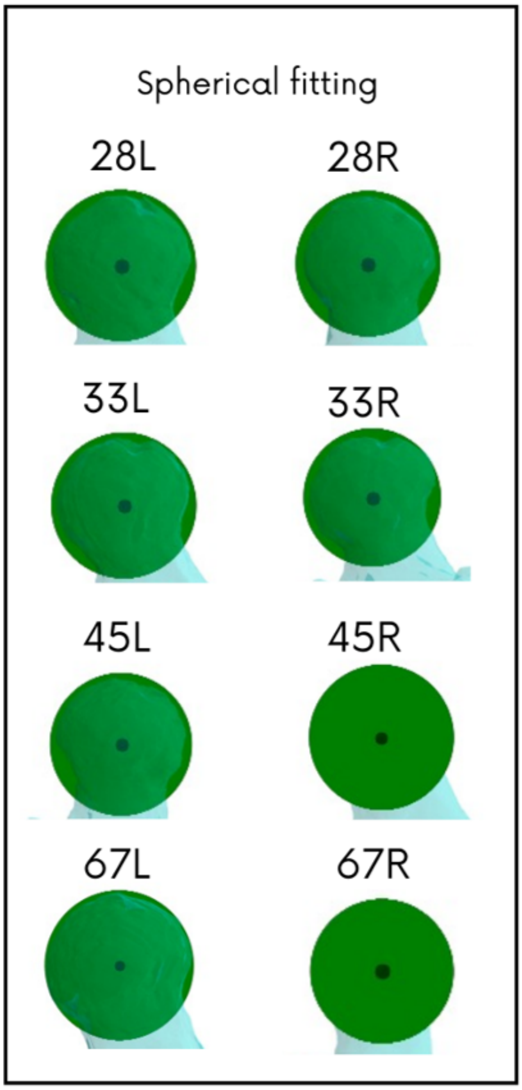

Figure 5.3: This image shows the femoral head (blue) with their fitted spheres (green) using the least square spherical fitting algorithm. The anteromedial part of the femoral head was used for spherical fitting.

5.2.2. Localisation of landmarks

Figure 5.4 shows the eight examined 3D hip models with their identified femoral head center and femoral neck center using the automatic workflow, denoted by a red dot. The femoral neck axis is represented by the dotted line connecting these two red dots. The arrows indicate incorrectly positioned femoral neck axes.

Figure 5.4 shows that for half of the dataset (patient 28 - right and left hip, patient 45 - left hip and patient 67 - right hip) the femoral neck axis seems to be positioned accurately. For the other half of the hips (patient 33 - right and left hip, patient 45 - right hip and patient 67 - left hip), the femoral neck axis seems to be positioned slightly superior as a result of the femoral neck center being detected slightly superior. This is denoted in Figure 5.4 with an arrow. The localized femoral head centers seem to be positioned accurately, centered in the middle of the femoral head of each 3D hip model.

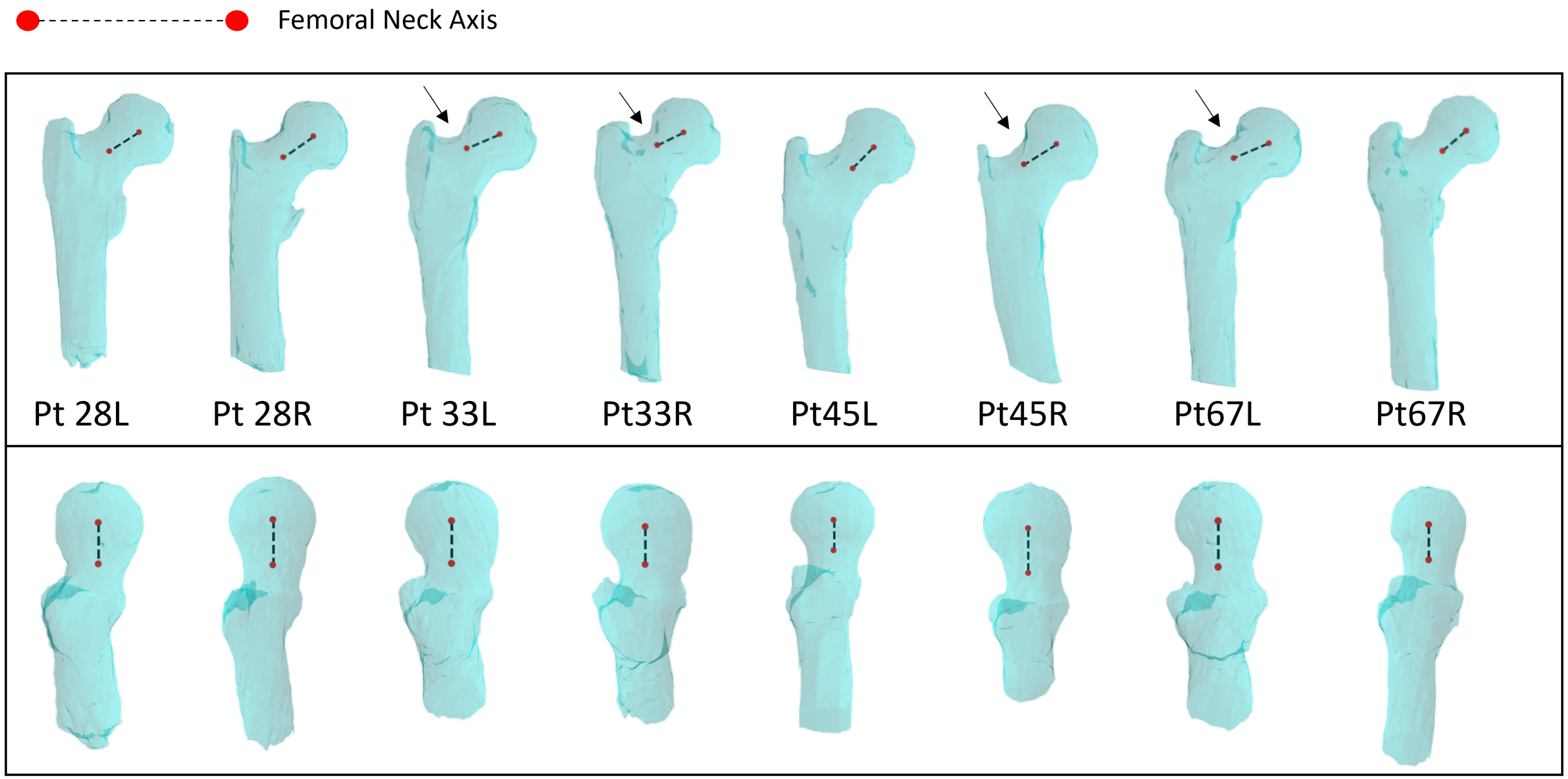

Figure 5.4: This image shows the eight examined 3D hip models with their identified femoral head center and femoral neck center using the automatic algorithm, denoted by a red dot. The femoral neck axis is represented by the dotted line connecting these two red dots. The arrows indicate the 3D hip models that have an incorrect positioned femoral neck axis, slightly more posterior than supposed to.

5.2.3. Femoral Head Morphology

Figure 5.5 shows the eight examined 3D hip model with cam morphology locations denoted in dark blue and with an arrow. Figure 5.5 shows that patient 33 has a prominent anterior cam morphology for both the left and the right hip. More subtle anterior cam morphologies are seen in the right and left hip of patient 28 and in the right hip of patient 45 and left hip of patient 67. A slight posterior bony protrusion is additionally seen in the left hip of patient 28. The left hip of patient 45 and right hip of patient 67 show spherically femoral heads, thus indicating a normal morphology of the femoral head.

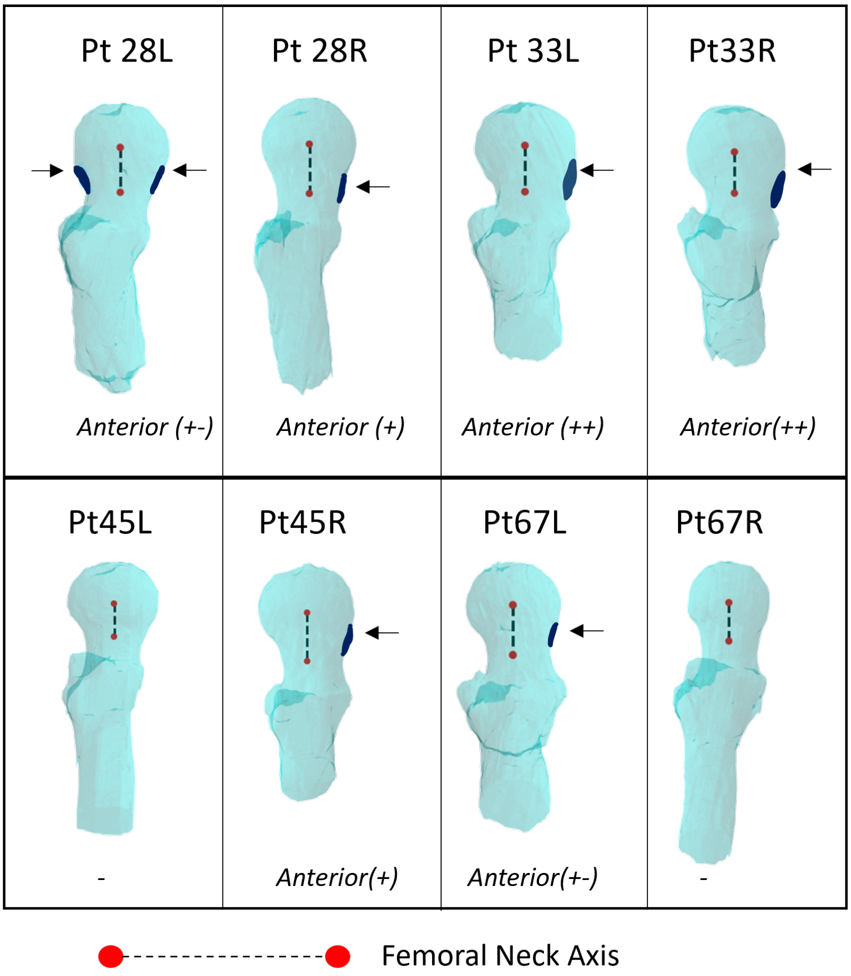

Figure 5.5: This image shows the eight examined 3D hip models with their identified femoral head center and femoral neck center using the automatic algorithm, denoted by a red dot. The femoral neck axis is represented by the dotted line connecting these two red dots. The dark blue part of the 3D model indicates the presence of any cam morphology. The prominence of the cam morphology is denoted below each 3D model using + and - signs.**+-** = slight bony protrusion, **+** = medium bony protrusion, **++** = prominent bony protrusion.

5.2.4. Correspondence Femoral Head Morphology and Alpha Angles

To graphically represent the distribution of the automatically computed and manually measured alpha angles around the femoral-head neck junction, polar plots were automatically generated by the workflow. Figure 5.6 provides an example of a polar plot depicting the alpha angle measurements of the left hip of patient 67. The polar plot displays the manual alpha angle measurements for six radial positions using brown dots, while the semi-automated alpha angle measurements for 12 radial positions are indicated by the blue region. The green circle represents the alpha angle threshold of 60°. These polar plots were automatically generated by the workflow to facilitate alpha angle interpretation for clinicians.

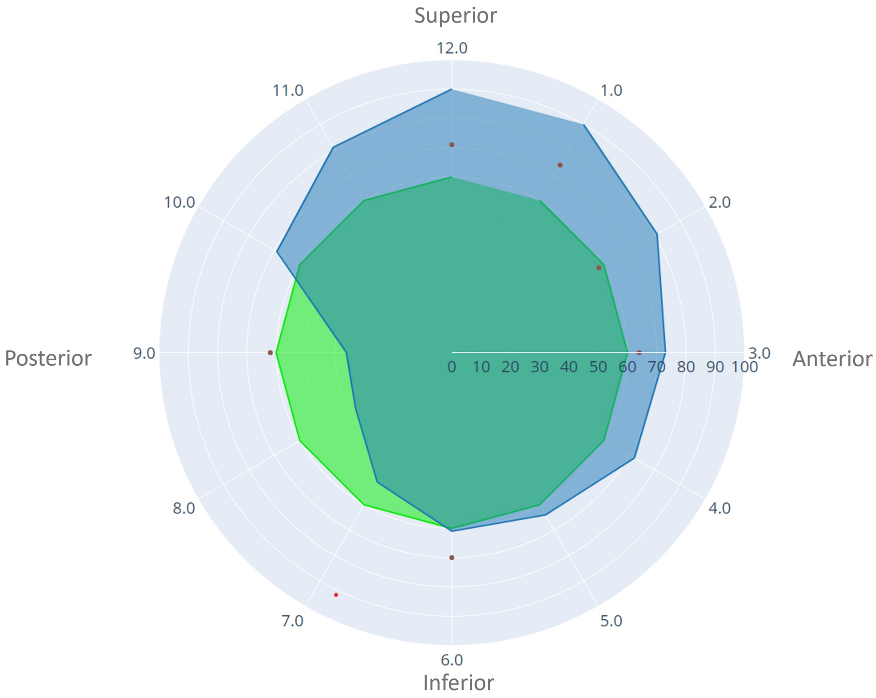

Figure 5.6: Polar plot depicting alpha angle measurements of the left hip of patient 67: the manual alpha angle measurements for 6 radial positions are depicted by the brown dots. The semi-automated alpha angle measurements are depicted in blue for 12 clockwise positions. The green circle represents the alpha angle threshold of 60°.

Polar plots were generated for each 3D hip model using a radial section-specific approach with various threshold and outlier detection methods:

- **Threshold:** Radius of the fitted sphere (R) or radius of the fitted sphere multiplied by the model specific factor.
- **The number of subsequent angles set as condition during outlier detection:** 1, 5, 10, 20.

A qualitative description of each polar plot is presented in Appendix B.

To organize the large number of polar plots generated, a bar chart was constructed, as depicted in Figure 5.7. Each position displaying a cam morphology (Figure 5.4) was systematically compared to the corresponding polar plot to see whether there was an alpha angle exceeding the threshold at that particular location. For instance, when the cam morphology was located anterior, then alpha angles between 2:00 o'clock and 4:00 o'clock were analyzed in the polar plot. It was counted as a true positive when at least one alpha angle (2:00, 3:00 and/or 4:00 o'clock) was higher than the diagnostic threshold of 60°. Note that the correspondence was assessed per anatomical region (superior, anterior, inferior or posterior) and not per radial section. The percentage of 3D hip models exhibiting a cam morphology location with at least one corresponding exceeding alpha angle is depicted as the percentage of true positives, represented by the green bars in Figure 5.7.

Figure 5.7 also shows a rough approximation of the proportion of false positives: the percentage of 3D hip models that have at least one alpha angle in their polar plot that exceeds the threshold at a location where actually a normal femoral head morphology was indicated. The false positives are represented by the blue bars.

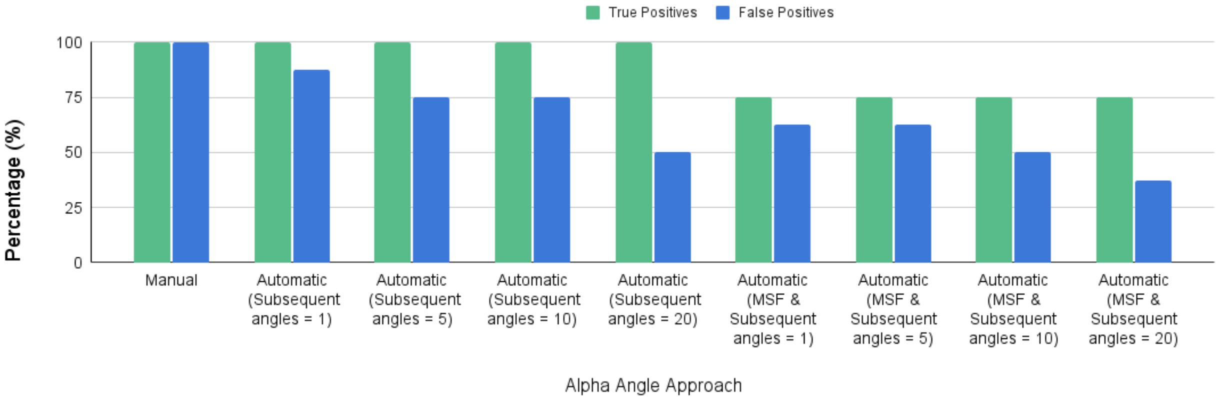

Figure 5.7: Bar graph showing the correspondence between the presence of a cam morphology and the manual and various automatic alpha angle measurements. The number of true positives (green) and false positives (blue) are expressed as percentage (%). **MSF** = Model Specific Factor.

The percentages presented in Figure 5.7 roughly indicate the degree of correspondence between the quantitative manual and semi-automated alpha angle measurements and the qualitative assessment of the femoral head morphology. Figure 5.7 indicates that for all 3D hip models that have a cam morphology, manual alpha angle measurements and all semi-automated measurements *without* a model specific factor threshold have at least one alpha angle within that particular anatomical region that exceeds the 60° threshold (100%). However, application of a model specific factor threshold results in the detection of the cam morphology site in only 75% of the cases, indicating a missed detection of cam morphology in 2 out of 6 hip joint models.

Additionally, Figure 5.7 shows a high percentage of false positives for both manual and semi-automated alpha angle measurements. In all 3D hip models, there was at least one manual measurement that exceeded the 60° threshold but did not correspond to a visual bony protrusion at the indicated site (100%). Similarly, the semi-automated methods also produced a high number of false positives, but applying a model specific factor threshold and increasing the required number of subsequent inclination angles to exceed the threshold reduced the percentage of false positives. Specifically, the lowest percentage of false positives was achieved with the semi-automated alpha angle measurement that applied a MSF threshold and required a minimum of 20 subsequent inclination angles to exceed the threshold.

5.3. Quantitative Validation

This section includes statistical analysis on the comparison of measured radii (Section 5.3.1) and alpha angles (Section 5.3.2).

5.3.1. Statistical Analysis: Radius

Table 5.1 presents the mean radius along with its standard deviation (SD) in millimeters (mm) for the circle drawn by the MSK radiologist and the sphere fitted by the semi-automated workflow for the radial section-specific approach for six clockwise positions. Table 5.1 also shows the radii (mm) measured by the radial section-aspecific approach. The mean radii (mm) ± SD (mm) have also been plotted in Figure 5.8 for the manual and radial section-specific approach. It shows that the mean manual radii are consistently smaller than the mean radial section-specific radii. Additionally, there is variability in the radii within each femoral head as demonstrated by the STD of each 3D hip model (Table 5.1 and Figure 5.8. It is noteworthy that the radii of the radial section-specific and radial section-aspecific approaches do not match, indicating variation in radii among radial sections (Table 5.1).

3D Hip Model	Manual Mean radius ± SD (mm)	Semi-automated (Radial section-specific) Mean radius ± SD (mm)	Semi-automated (Radial section-aspecific) Radius (mm)
Pt 28 (Right Hip)	23.83 ± 0.8	25.85 ± 0.5	26.0
Pt 28 (Left Hip)	23.42 ± 0.6	25.26 ± 0.6	26.0
Pt 33 (Right hip)	21.83 ± 0.4	24.82 ± 0.6	24.0
Pt 33 (Left Hip)	21.83 ± 0.4	24.87 ± 0.2	24.0
Pt 45 (Right hip)	25.00 ± 0.6	26.92 ± 0.5	27.0
Pt 45 (Left hip)	24.17 ± 0.8	26.73 ± 0.3	27.0
Pt 67 (Right hip)	21.00 ± 0.8	21.86 ± 0.3	22.0
Pt 67 (Left hip)	21.00 ± 0.8	22.18 ± 0.6	22.0

Table 5.1: the mean radius ± SD (mm) of the circle drawn by the MSK radiologist and the sphere fitted by the semi-automated workflow for the radial section-specific approach of the six clockwise positions are presented in the second and third column. The fourth column represents the radius (mm) obtained with the radial section-aspecific radial fitting method in which singular spherical fitting is performed to obtain a radius that approximates all radial sections.

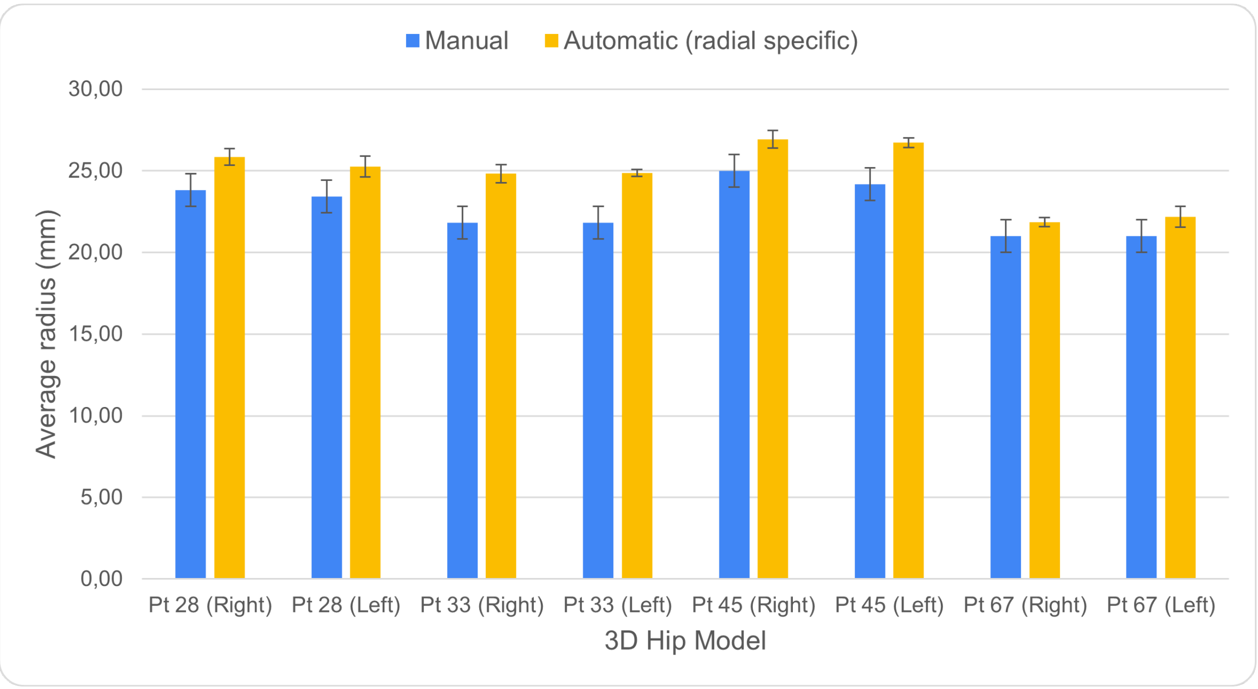

Figure 5.8: Bar graph showing the average radius (mm) of multiple radial sections for each 3D hip model, measured manually (blue) and automatic (yellow) using a radial section-specific spherical fitting. The error bars represent the standard deviation (mm).

A two-sides two-sample t-test was conducted to compare the manual measured radii and the radii obtained through the radial section-specific spherical fitting. Table 5.2 displays the p-values with a bonferonni correction applied to the level of statistical significance to correct for the conduction of multiple statistical tests. This entails dividing the original significance level (p-value = 0.05) by the number of individual statistical tests (N=18), resulting in an adjusted significance level of 0.003. The p-values indicate that 50% of the manual radii show a statistically significant difference from automatic radial section-specific radii (Table 5.2). Radial section-aspecific radii were statistically compared by means of a one-sample t-test as there was only one single radius for each 3D hip model. The p-values indicate that 63% of the manual radii show a statistically significant difference with automatic radial section-aspecific radii and 13% (1 out of 8 3D hip models) with radial section-specific radii show a statistical significant difference (Table 5.2.)

3D Hip Model	p-value (manual vs radial section-specific)	p-value (manual vs radial section-aspecific)	p-value (radial section-aspecifc vs radial section-specific)
Pt 28 (Right Hip)	**0.000**	0.001	0.494
Pt 28 (Left Hip)	0.011	**0.000**	0.035
Pt 33 (Right hip)	**0.000**	**0.000**	0.016
Pt 33 (Left Hip)	**0.000**	**0.000**	**0.000**
Pt 45 (Right hip)	0.045	0.025	0.264
Pt 45 (Left hip)	0.049	0.025	0.517
Pt 67 (Right hip)	0.005	**0.000**	0.743
Pt 67 (Left hip)	**0.002**	**0.000**	0.064

Table 5.2: The p-values as a result of the t-test to compare whether the mean radius of the different type of measurements were significantly different (manual vs semi-automated radial section-specific). P-values below 0.003 were considered statistically significant. All values that are statistically significant are bold.

5.3.2. Statistical Analysis: Alpha Angles

Table 5.3 shows the inter-rater reliability for manual measurement of alpha angles vs automatic measurement of alpha angles. Statistical validation was executed for various automatic approaches based on the novel strategies that were incorporated (radial section-specific spherical fitting, model specific factor threshold alteration and/or outlier detection).

The mean alpha angle measured across all 3D hip models, manually measured by the MSK radiologist was 65.49 ± 10.23° whereas the mean alpha angle measured by the algorithm ranged between 55.83 ° ± 21.28 and 71.36°± 22.67, depending on the automatic approach used. The ICC ranged from -0.02 to 0.40 and the MAD ranged between 19.54° and 22.10°. None of the ICCs were statistically significant ($p\text{-value} < 0.003$), using also a bonferonni corrected level of statistical significance to correct for multiple statistical testing. This means no meaningful relationship between the automatic and manual measurements found.

	Outlier detection (Number of subsequent angles)	Radius Multiplication	Mean	SD	ICC	95% CI	MAD	p-value
Manual			65.49	10.23				
Automatic (radius section-specific)	1	1.0	71.36	22.67	0.40	[-0.51, 0.89]	20.23	0.19
	1	MSF	62.19	23.25	0.17	[-0.67, 0.82]	21.85	0.36
	5	1.0	68.45	22.60	0.19	[-0.66, 0.83]	20.98	0.34
	5	MSF	61.11	23.59	0.23	[-0.63, 0.84]	21.92	0.31
	10	1.0	62.52	23.13	0.16	[-0.68, 0.82]	20.44	0.37
	10	MSF	56.17	22.62	0.21	[-0,64, 0.83]	20.95	0.32
	20	1.0	65.41	22.13	0.25	[-0.62, 0.85]	19.54	0.29
	20	MSF	56.48	22.07	0.19	[-0.66, 0.83]	20.40	0.34
Automatic (radius section-aspecifc)	1	1.0	69.14	23.42	0.17	[-0.60, 0.82]	22.10	0.32
	1	MSF	56.44	21.82	0.36	[-0.54, 0.88]	20.85	0.22
	5	1.0	67.44	23.42	0.18	[-0.66, 0.82]	21.96	0.25
	5	MSF	56.60	21.76	0.29	[-0.66, 0.86]	20.69	0.26
	10	1.0	62.67	24.25	-0.02	[-0.76, 0.75]	22.65	0.51
	10	MSF	55.83	21.28	0.32	[-0.58, 0.86]	20.63	0.25
	20	1.0	63.77	22.74	0.26	[-0.62, 0.85]	20.15	0.29
	20	MSF	55.83	21.28	0.32	[-0.58, 0.86]	20.63	0.25

Table 5.3: The absolute agreement between manual and automatic alpha angle measurements in 3D models of the hip joint: ICCs and MADs with varying outlier detection (n=1,5,10 and 20) and sphere fitting thresholds (1.0 or model specific factor). The table additionally shows the mean ± standard deviation, 95% CI and p-values for all different approaches. **MSF** = Model Specific Factor

The highest ICC of 0.40 [-0.51, 0.89], MAD of 20.23°, p-value = 0.19, was seemingly achieved using a radius section-specific automatic approach without any outlier detection (n=1) without model specific factor multiplication. The lowest ICC reaches a negative value of -0.02 [-0.76,0.75] with a MAD of 22.65°, corresponding to the radius section-aspecific approach with no model specific factor multiplication and 10 subsequent inclination angles exceeding the threshold, set as condition to detect outliers. All ICCs are below 0.50, indicating poor agreement between manual and automatic alpha angle measurements.

Automatic approaches

The various automatic approaches are based on the outlier detection method, the threshold and the spherical LSF method. As shown in Table 5.3, no pattern is observed as there is no consistent increase or decrease in ICC or MAD when one of these independent variables is changed while the other two are kept constant.

The Bland-Altman plot for the automatic approach with the apparently highest ICC was shown in Figure 8.7. The plot revealed mean (non-absolute) angular differences of 4.75° ± 47.75° between the manual and automatic measurements. Bland-Altman plots for all the other comparisons can be found in Appendix A.

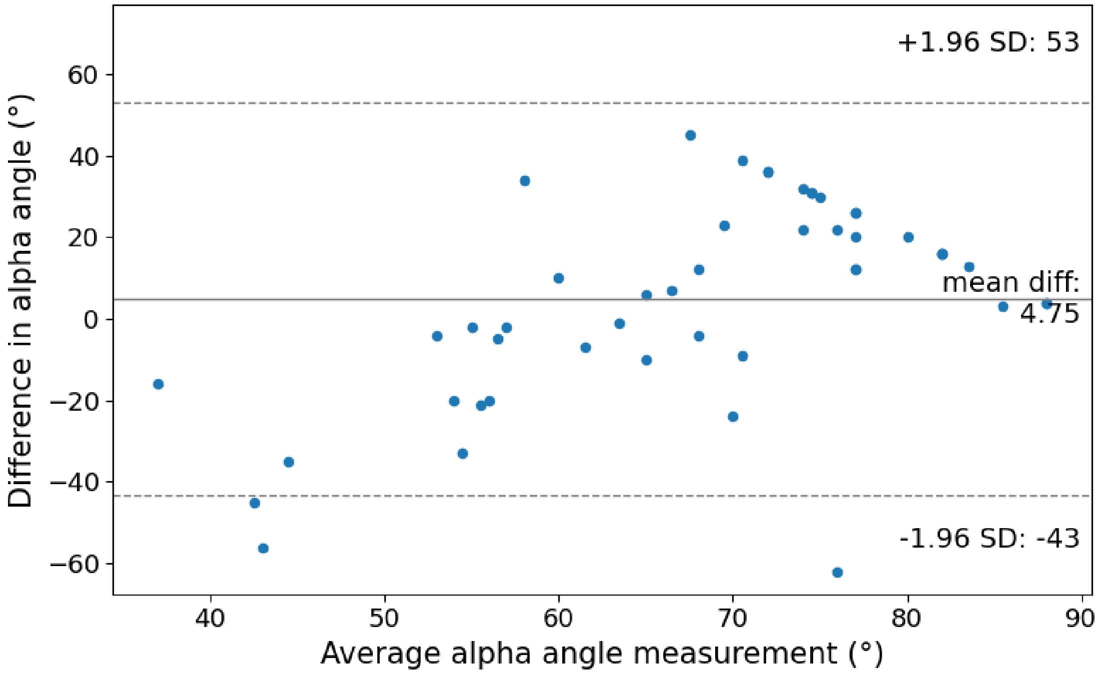

Figure 5.9: Bland-Altman plot depicting the agreement on manual alpha angle measurement by an MSK radiologist and automatic alpha angle measurement computed by a workflow. The alpha angle measurements were obtained with an automatic approach that did not involve multiplication by a model specific factor or any outlier detection. The dotted lines indicate the 1.96 standard deviation with an upper boundary of 53 and a lower boundary of -43. The middle grey line indicates the mean difference of 4.75.

Timing

The time required for the automatic algorithm to perform 12 radial alpha angle measurements, including radial reformatting was 26 seconds. The mean time for one manual alpha angle measurement was 1.3 ± 0.98 min, excluding the additional time required for radial reformatting. For 12 radial alpha angle measurements this would approximately result in a time difference of 15 minutes.

6

Discussion

This study proposed a semi-automated workflow for alpha angle measurements based on ZTE MRI-based 3D models of the proximal femur for patients with FAIS. The proposed workflow is developed in open-source software, which makes it accessible to all clinicians and researchers regardless of their financial resources, enabling them to evaluate the degree of femoral deformity in a fast and objective manner. The workflow computes 12 alpha angles corresponding to the 12 clockwise positions centered around the femoral neck axis, within 26 seconds. This result in a significant reduction in measurement time of approximately 15 minutes in comparison to manual measurements. The alpha angles computed by the workflow were automatically generated in a xlsx report. Additionally, a polar plot is automatically generated that visualizes the distribution of alpha angles around the circumference of a circle, with the center of the circle representing the center of the femoral head. Furthermore, the semi-automated workflow incorporated novel strategies, including radial section-specific spherical LSF, outlier detection and model specific thresholds. These strategies have not been reported in previous studies and intended to improve the accuracy and robustness of the measurements.

6.1. Results analysis: Questionnaire

Prior to developing the semi-automated alpha angle workflow, a questionnaire was conducted among the end-users to understand the current clinical practices regarding FAIS diagnosis and the requirements for the semi-automated workflow to be implementable.

6.1.1. Clinical Practice

Questionnaire outcomes established that in clinical practice 2D Imaging (X-ray) is still the most frequently used imaging modality in the process of diagnosing FAIS. The software to perform manual alpha angle measurements involving user-input was not experienced highly, because of its lack of user friendliness. This might be the reason that some clinicians perform solely a qualitative assessment of the morphology of the hip joint rather than additional quantitative approaches such as measurement of the alpha angle. Non consistent thresholds for the alpha angle were found, emphasizing the need for a more standardized approach.

6.1.2. Requirements Workflow

The semi-automated workflow addressed several of the requirements that clinicians reported for the (semi)-automated software in the questionnaire. This included 3D visualization of where the alpha angle exceeds the threshold, automatic generation of findings reports in xlsx format, fast computation and automatic centering of the femoral head. In addition, clinicians emphasized the need for high accuracy, correction for pelvic tilt, and dynamic visualization of impinged areas during movement. As the performance of the (semi)-automated workflow is further established in future research, future steps may include a more dynamic approach. Ongoing monitoring of end-user needs and preferences will aid in the development of a standardized (semi)-automated approach for improved diagnosis of FAIS.

6.2. Results analysis: Alpha Angle

Reliability assessment showed poor agreement when comparing the manual alpha angle measurements to the semi-automated alpha angle measurements using various semi-automated approaches. The highest ICC of 0.40 [95%CI: -0.51 - 0.89] was achieved using an semi-automated approach with radius section-specific spherical LSF, no model specific factor multiplication and no outlier detection was applied (n=1) (Table 5.3). All the other approaches achieved lower ICCs, ranging from -0.02 to 0.36. The lowest MAD was 19.54° using a radius section-specific spherical LSF, no model specific factor multiplication and an outlier detection applied using 20 subsequent alpha angles. The other approaches ranged from 20.15°- 22.65°.

The poor agreement indicated by the ICC, the large MADs and the wide 95% CI can be explained by a number of reasons. First of all, statistically significant differences (p-value < 0.003) between the radii of manual and semi-automated measurements in each radial section were observed, leading to different localization of where the bone exceeds the best fit circle. Secondly, this study found variation in radii between and within each radial section even at locations without a cam morphology, suggesting the femoral head is not perfectly spherical. This affects both manual and semi-automated alpha angle measurements, as both approaches rely on this assumption. Third, semi-automated alpha angles were affected by the inaccurate localisation of landmarks in some of the 3D hip models. Last, errors in steps involved prior to the workflow measurements propagate throughout the pipeline: segmentation and mesh filtering. Each reason is elaborated on below.

6.2.1. Radii Differences

Statistically significant differences (p-value <0.003) between manually drawn circular radii and automatically fitted radial section-specific spherical radii for 50% of all 3D hip models were found (Table 5.2). For radial section-aspecific spherical radii, statistical differences were found in 63% of all 3D hip models. All manually drawn circular radii were smaller than the radii of the automated fitted spheres. As a result, the point at which the cortical bone exceeds the best fit circle (Point P') will be positioned at a different location in manual measurements compared to semi-automated measurements, leading to disagreement in alpha angle measurements.

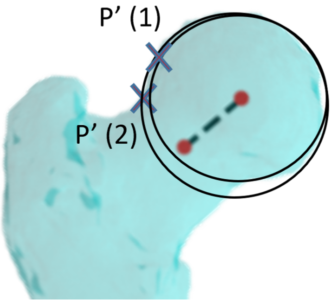

Figure 6.1: This figure illustrates the effect of radii differences. A larger drawn circle to approximate the femoral head will lead to a different localization of point P'.As a result, the alpha angle localized at P'(1) will be higher than the alpha angle localized at P'(2).

6.2.2. Asphericity of the femoral head

The alpha angle as quantitative imaging parameter relies on the assumption that the femoral head is perfectly spherical. The semi-automated workflow was built on this underlying assumption as it follows the definition of the alpha angle: *The angle between the femoral neck axis and the line drawn from the femoral head center to the point (P') at which the femoral head laterally exceeds the best fit circle.* But even without a cam morphology, the femoral head is not perfectly spherical. Although only 13% of the 3D hip models (one out of eight hips) showed statistically significant differences (p-value <0.003) between the radial section-specific and radial section-aspecific approach (Table 5.2), the variability (SD) of the radii among the radial section-specific manually drawn circles and the multiple automated fitted spheres for each 3D hip model indicate that the femoral head is not perfectly spherical (Table 5.1).

Figure 4.16 and Figure 5.3 support this finding by visually showing that the femoral head contour is not perfectly spherical for one of the hips from the dataset used in this study. Asphericity is particularly pronounced in the superior part of the femoral head, where a small dimple at the site of the attachment of the ligamentem teres can be observed. Visual inspection of the inferior part of the femoral head shows that the superior portion (above the femoral head center) is larger than the inferior portion (below the femoral head center) (Figure 5.3). In the semi-automated workflow, spheres were fitted to superior half of the femoral head, which lead to an overestimation of the radius of the femoral head when the inferior part is relatively smaller. The asphericity of femoral heads explains why the radii found by the semi-automated workflow were all larger than the radii of the radiologist who took into account the entire femoral head. This overestimation of the radius of the femoral head has consequences for semi-automated alpha computation, visualized in Figure 6.2.

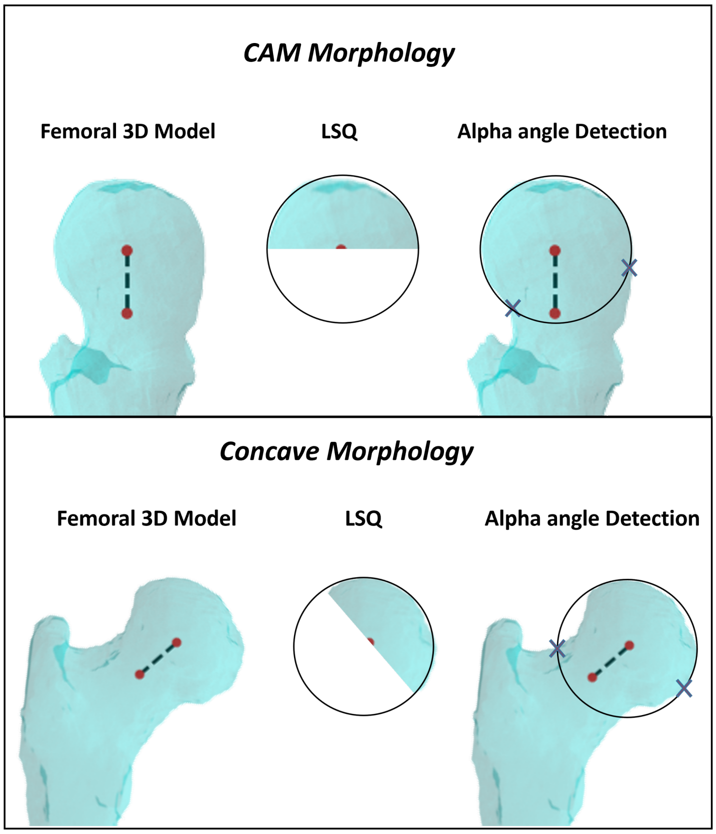

Figure 6.2: This figure illustrates the effect of the how assuming that a normal morphology of the femoral head is spherically shaped affects the semi-automated algorithm in alpha angle detection. In case of a cam morphology (top image), the bone will exceed the fitted at the site of the cam morphology and this site will be detected by the algorithm as the location to measure the alpha angle. In case of a concave morphology (bottom image), the fitted sphere is an overestimation of the femoral head, leading to very low alpha angles to be detected by the semi-automated workflow when the concavity starts rather superior. Very high alpha angles are detected when the concavity starts rather inferior.

In case there is a bony protrusion, nonetheless of the sphere being overestimated, the bony protrusion will exceed the threshold at some point and lead to detection of the cam morphology (Figure 6.2 top image). The opposite situation is an individual with a more concave morphology of the femoral head. If the concavity starts early, then the inclination angle at which the bone exceeds the best fit sphere will be very large, because of the overestimated sphere with respect to the inferior part. This results in very low alpha angles (Figure 6.2 - bottom image - superior cross). If the concavity starts rather late, the inclination angle at which the bone exceeds the best fit sphere will likely be zero or close to zero as the femoral head is at its widest at that point (Figure 6.2 - bottom image - inferior cross). Consequently, asphericity of the femoral head affects semi-automated measurements, resulting in outliers when a hip has a concave morphology.

This finding is supported by the bar graph (Figure 5.7 - Section 5.2.4) that shows a high percentage of true positives, but also a high percentage of false positives in cam morphology detection. This is the case for both the manual and semi-automated alpha angle measurements. The percentage of false positives for manual alpha angle measurements was 100 % (Figure 5.7). This means that in each 3D hip model at a region with a normal morphology, at least one of the six clockwise measurements exceeded the threshold. Notably, the alpha angle values that make up the false positive percentage value were less extreme than the outliers that make up the false positive percentage in the semi-automated workflow. The human brain unconsciously does take into account the inferior part of the femoral head, even though there is a cam morphology and therefore radiologists might draw a smaller best fit circle, resulting in less extreme alpha angle values. This high percentage of false positives suggest that manual alpha angle measurements are also affected by the asphericity of the femoral head. As both semi-automated and manual measurements are affected by this underlying assumption, the findings in this study question the reliability of the alpha angle as a quantitative measure for diagnosis of FAIS in general.

6.2.3. Inaccurate localization of landmarks

The third reason for the poor agreement between manual and alpha angle measurements is due to the inaccurate localization of important landmarks within some of the 3D hip models. Specifically, the femoral neck center was placed more superiorly than its true anatomical central location in 50 % of the 3D models of the proximal femur (four out of eight hips) (Figure 5.4). Although the femoral head center visually seemed to be positioned correctly in the center of the femoral head, incorrect localization of the femoral neck center results in an incorrect positioning of the femoral neck axis as this axis is formed by connecting the femoral head center to the femoral neck center. The femoral neck axis is a crucial reference axis that positions the 3D model within the spherical coordinate system. First of all, it determines the positions of the clockwise radial sections and thus inaccurate positioning leads to a mismatch in clockwise position with manual measurements.

Second of all, the position of the femoral neck axis determines where the raycasting ($\theta = 0$) algorithm starts casting its first ray. Figure 6.3 attempts to explain the effect of an incorrect positioned femoral neck axis as the starting position of the raycasting P1’ is located more superior than P1, and P2’ being more inferior than P2. This causes an overestimation of the inclination angle at which the distance to the femoral head center exceeds the threshold in superior locations, and an underestimation in inferior locations. As a consequence, alpha angle measurements are underestimated in superior locations and overestimated in inferior locations.

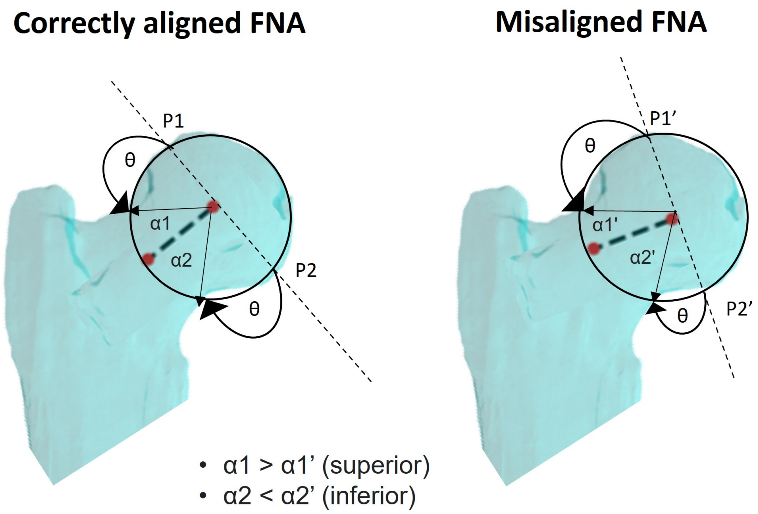

Figure 6.3: This figure demonstrates the impact of a misaligned femoral neck axis (FNA) on alpha angle measurement. The FNA is indicated by the black dotted line connecting the femoral head center (FHC) and femoral neck center (FNC) (red dots) in both images. The inclination angle at which the bone exceeds the best fit circle is represented by θ. a1(’) and a2(’) indicate the superior and inferior alpha angles, respectively. The points where $\theta = 0$ for a specific radial section are represented by P1, P2, P1’, and P2’. The images illustrate that the misaligned FNA results in P2’ being positioned more inferiorly than P2 and P1’ being positioned more superiorly than P1, affecting the alpha angle measurement.

The reason for incorrect femoral neck center positioning is founded in the slicing direction that was specified. The rationale behind slicing is to find the isthmus of the femoral neck, so ideally the slicing direction is specified parallel to the femoral neck axis. Since the direction of the femoral neck axis is an unknown variable, specifically the one that was aimed to find, an alternative approximation of the femoral neck axis was used to initialize the approach: the PS vector. This PS vector, located from the centroid of the hip model to the femoral head center is placed more inferior than the direction of the true anatomical femoral neck axis. This imprecise approximation of the femoral neck axis leads to the femoral neck center being located incorrect in some 3D hip models.

6.2.4. Error Propagation

Lastly, the difference in radii and alpha angle measurements between manual and automated measurements is partially attributed to inaccuracies introduced prior to the semi-automated workflow. The MSK radiologist performed the radii and alpha angle measurement on 2D ZTE MRI scans, whereas the semi-automated radii and alpha angle measurements were performed on 3D hip models. Going from 2D ZTE MRI scans to 3D hip models involved manual segmentation and mesh filtering, which can introduce errors that propagate until the final alpha angle measurement. This means that ICCs and MADs that derive from there are not solely attributed to inaccuracies of the semi-automated workflow. They are also due to prior steps when considering the entire pipeline.

Segmentation

Manual segmentation of the ZTE MRI scans to create 3D hip models has the potential to introduce human error if the femoral head-neck junction is not accurately captured, resulting in an over- or underestimation of the alpha angle. The accuracy of manual segmentation can be influenced by the expertise and experience of the person performing the segmentation. To overcome the limitations of manual segmentation, it is recommended to develop automatic segmentation methods using deep learning techniques. While no specific deep learning method has been developed for the automatic segmentation of the ZTE sequence yet, promising results have been reported for accurately segmenting the hip joint from MRI scans.[35] Human error could be eliminated once deep learning approaches will be adopted.

Mesh Filtering

The manually segmented images were rendered into a 3D model of the hip. This raw 3D model was then subjected to a smoothing operation and reduction of the number of triangles that make up the 3D model. While smoothing can reduce surface irregularities resulting from manual segmentation, both operations can compromise the original morphology of the hip joint.[36] Smoothing can reduce the number of vertices and change the orientation of the faces, resulting in loss of detail. Additionally, mesh filtering operations were applied to ensure the 3D models were watertight, which also involved modification of the original surface of the mesh. For example the process of filling gaps in the mesh may introduce non-physiological features into the model, such as the creation of false surfaces or smoothing over small details that could be clinically relevant, potentially leading to errors in the alpha angle measurements of the 3D models.[36]

6.3. Results analysis: Novel Strategies

The automated workflow proposed novel empirical strategies that have not been reported in previous studies, intended to improve the performance and robustness of automatic alpha angle measurements. The innovative techniques include radial-specific spherical LSF, which replaces the previously used radial-aspecific (singular) spherical LSF. Additionally, a subject-specific threshold was established through model specific factor multiplication, and outliers were detected by including a condition of N number of subsequent angles.

Table 5.3 did not show any increase in ICC or decrease in MAD for all three novel strategies, suggesting that the use of these novel strategies does not improve the performance of the workflow in measuring the alpha angle. Qualitative evaluation of some of these strategies do possess potential, as discussed below.

6.3.1. Spherical Fitting

As already mentioned in Section 6.2.2, both quantitative and qualitative evaluation indicate that the femoral head is not perfectly spherical. Although there is still variation *within* radial sections, using a radial section-specific spherical fitting will eliminate inaccuracies in alpha angle measurement due to variation *between* radial sections.

6.3.2. Threshold

The qualitative evaluation conducted in this study regarding the threshold revealed that the model specific factor multiplication led to a decreased number of true positives. Specifically, the model specific factor multiplication causes a 2-3% alteration in the threshold, depending on the 3D hip model used. The fact that such a small change in the threshold has a negative impact on cam morphology detection highlights the sensitivity of the alpha angle to inaccuracies in the radius of the fitted sphere. Although this study indicates that using an model specific factor threshold is not an effective strategy for improving alpha angle measurements, it confirms the overall sensitivity of the alpha angle measurement. The findings also underscore the need for location-specific thresholds, as a single threshold for the entire femoral head is too simplistic. Such research should be taken into account in future investigations to enhance the accuracy and reliability of alpha angle measurements.

6.3.3. Outlier Detection

Section 6.2.2 of this study provided a detailed explanation of how the asphericity of the femoral head resulted in an overestimation of the fitted sphere in the workflow, leading to the generation of extreme alpha angle values or outliers for certain clockwise positions. This highlights the presence of outliers in the automated workflow and emphasizes the importance of detecting and eliminating them. The bar graph depicted in Figure 5.7 indicates that the application of outlier detection reduces the percentage of false negatives. Additionally, it was observed that the higher the number of subsequent inclination angles, the lower the percentage of false negatives. The polar plots presented in Appendix A further illustrate that outlier detection effectively removes 90° alpha angles, which correspond to locations where normal morphology is indicated.

Qualitative evaluation of the outlier detection method suggests its potential usefulness, although quantitative reliability statistical analysis does not fully support it. It is worth noting, however, that the optimal number of subsequent angles to be considered needs to be fine-tuned and validated in future studies. This is important because setting the condition to 20 subsequent inclination angles could potentially result in missing small bony protrusions, like little osteophytes. This makes this outlier detection method a trade-off between sensitivity and specificity.

6.4. Literature Comparison

6.4.1. Interobserver reliability (automatic vs manual)

Various ICCs values have been reported in literature for comparison between manual and automatic alpha angle measurements. Most of the ICCs reported are similar to the highest ICC reported in this study, indicating poor-moderate agreement.[37, 38, 39] However, the reported 95% CIs are narrower. This highlights the importance of validating the proposed workflow in this study with a larger dataset.

There was one study from *Xia et al* that reported excellent agreement with intraobserver and interobserver variabilities of >0.95 (0.91-0.98) using statistical shape modeling for bone segmentation and automatic selection of the femoral head-neck junction as the region of interest. They used LSF with a sphere, hyperboloid, and ellipse for the femoral head, neck, and shaft, respectively, and determined alpha angles using 2D shape maps similar to this study, but with smoothness constraints to find the alpha angle.[40] The excellent agreement of this method suggests that alternative (semi)-automated approaches might improve the reliability of (semi)-automated alpha angle measurements.

6.4.2. Interobserver reliability (manual vs manual)

The aforementioned studies also reported inter-observer ICCs between manual measurements performed by different assessors. *Fischer et al* reported poor inter-observer agreement with ICCs of manual measurements of 0.222/0.223/0.347. No 95% CI values were reported. [38]. *Ewertowski et al* found moderate interobserver ICCs of 0.45 [95% CI:0.22-0.61] (measurement 1) and 0.56 [95% CI:0.30-0.64] (measurement 2). These results suggest that the level of agreement between (semi)-automated and manual measurements is comparable to the agreement between manual measurements taken by different observers. Manual alpha angle measurements are strongly dependent on how the best fit circle is drawn to approximate the head. As discussed, asphericity leads to different subjective interpretation of the best fit which may explain the low agreement found also between observers.

6.5. Limitations and Future Research Recommendations

Limitations and associated future research recommendations of this research are stated below in Section 6.5.2 until Section 6.5.4. Section 6.5.5 until Section 6.5.7 provide additional future recommendations for quantitative evaluation of cam morphology.

6.5.1. Quality of the ZTE Images

The first limitation is that the quality of ZTE MRI scabs was not optimal. A high degree of noise was present and the spatial resolution was low, leading to partial volume effects that made it difficult to distinguish the contours of the cortical bone. This challenged human interpretation of the images during both the manual segmentation and manual alpha angle measurements. Specifically at the supero-anterior location, the depiction of cortical bone was particularly thin at the supero-anterior location, which is the most critical location for identifying cam morphology in the 3D model. The 3D models were created based on ZTE MRI scans, because of its unique capability as MRI sequence to depict cortical bone without having to use radiation as opposed to CT, but if it doesn't accurately depict the true contour of the cortical bone, its use should be questioned or its quality should be enhanced.

To enhance the quality of the data, modifications to the MRI ZTE sequence parameters could be considered (Table 4.1). Specifically, increasing the number of averages (NEX) and decreasing the field of view (FOV) to cover only the hip joint may enhance the signal-to-noise ratio (SNR) of the scans. Additionally, recent advancements in deep learning techniques have demonstrated the ability to remove motion artifacts and denoise ZTE scans, which could lead to significant improvements in image quality and facilitate automatic segmentation in the future.[41]

6.5.2. Diversity within the Dataset

The second limitation of this study is that the Feyenoord Cohort is comprised exclusively of young male football players who were exposed to high mechanical loading during their childhood. In future research, it would be also interesting to include a broader population, such as females, older individuals, and those who are less physically active. As technology advances and automated segmentation techniques are refined, generating 3D models of the hip joint will become less labor-intensive, thus making an expanded validation more feasible.

6.5.3. Size of the Dataset

The third limitation is that a small dataset has been used for validation, consisting of only 48 alpha angle measurements derived from eight 3D models of the hip. A power analysis was conducted to determine the minimum sample size needed to achieve a power of 80%, given an estimated standard deviation of 8°, an α of .05, and a desired MAD of 2°. This power analysis suggested that at least 43 alpha angle measurements needed to be validated. However, since some of the alpha angles are correlated (as they are derived from the same hip), the power analysis may have underestimated the required sample size. This is reflected in the wide 95% CIs that were reported in Table 5.3. Statistical analysis has been conducted also for each clockwise position. Appendix B includes tables with statistical outcomes per clockwise position. These clockwise specific statistics were not included in the main body of the thesis as the statistics were only computed with 8 measurements per clockwise position (corresponding to 1 measurement per hip).

Table 5.3 includes a negative ICC, which in general means that the agreement is worse than random. ICCs will be negative whenever the variability within the two types of measurements exceeds the variability across the two types of measurements. It is recommended that in future research, validation is executed with a larger dataset.

6.5.4. Components of Subjectivity

The final limitation of this study is that no inter and intra-observer reliability for the manual measurements has been conducted. Because the semi-automated workflow is still early in its development it was decided to not involve an additional MSK radiologist and/or let the alpha angle measurements be repeated. It would be recommended in future to determine the level of observer error to establish the reliability of the manual measurements. Manual alpha angle measurements rely on the clinician's experience with reading hip radiograph. Besides, manual radial reformatting was also executed by the MSK radiologist. The ZTE MRI scans were acquired with a misaligned radial axis thus this extra manual step was required. This may have impacted the match with automated radially reformatted planes.

6.5.5. Error Propagation

It was beyond the scope of this study to research the influence and error propagation of the segmentation and the mesh filtering. Future research should consider incorporating assessment of error propagation to gain a comprehensive understanding of the potential impact of these processing steps on the accuracy and precision of semi-automated alpha angle measurements. By identifying potential sources of error, future studies can focus on refining the image processing and 3D mesh filtering pipeline to minimize error propagation and enhance the accuracy of the computed hip parameters.

6.5.6. Alternative localisation of landmarks

Slicing was an approach that did not result in accurate localisation of the femoral neck center in all 3D hip models. This approach was chosen because of the small dataset available. In case a dataset labelled with landmarks and cam morphology locations is available, more advanced approaches such as statistical shape modelling in combination with correspondence mapping or deep learning can be applied to automatically detect landmarks, axes and regions of interest, preventing the need for any approximation that might lead to inaccuracies. The use of statistical shape modelling in general could aid in creating a reference 3D model of the proximal femur, representing a normal femoral head morphology. Registration of 3D hip models with such a statistical shape model could result in more accurate cam morphology detection that incorporates the imperfect spherical shape of the femoral head.

6.5.7. Alternative Hip Parameters

The alpha angle is the most commonly used quantitative imaging parameters to evaluate the degree of asphericity in FAIS patients.[14] However there are existing alternative quantitative parameters such as the Triangular Index (TI) and the Head-Neck Offset Ratio (HNOR) which could potentially be valuable complentary to the alpha angle (Figure 6.4). This section solely introduces the idea of using alternative quantitative imaging parameters, because it extends beyond the primary focus of this thesis. A more comprehensive and detailed discussion can be found in Appendix C.

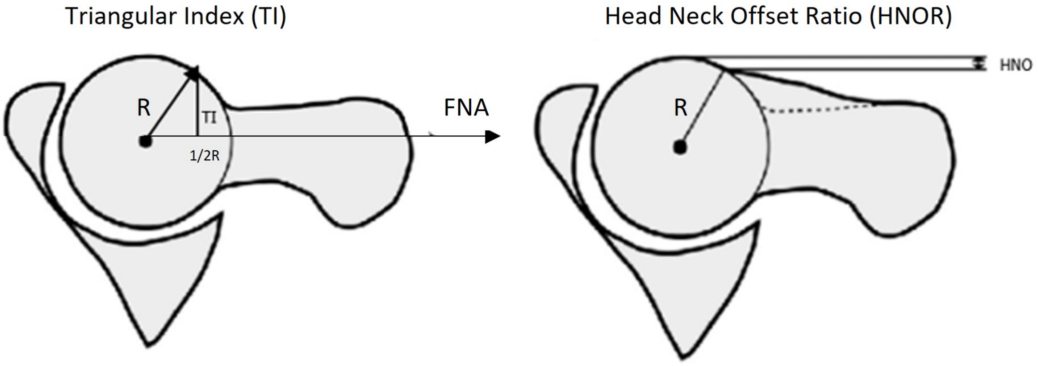

Figure 6.4: Left: The Triangular Index (TI). The radius (R) of the femoral head is measured. Then 1/2 R and the corresponding perpendicular height (H) to the cortex are measured. This is the TI. If the pathologically increased R at 1/2r (the TI) ≥ R + 1.67 mm, the cam morphology is present. **Right**: The Head Neck Offset Ratio (HNOR). The HNOR is computed by dividing the Head-Neck-Offset (HNO) by the diameter of the fitted sphere (= 2*R). The HNO is defined as the distance between the tangent of the femoral neck and the tangent of the femoral head parallel to the FNA. A threshold of <0.17 is suggested for the HNOR to be indicative for cam morphology.

Nepple et al reported interobserver/intraobserver ICCs of the TI of 0.72 [95%: 0.63-0.80]/ 0.99 [95%CI: 0.99-1.00] respectively. The HNOR had an interobserver ICC of 0.89 [95%:0.85, 0.92] and an intraobserver ICC of 0.96 [95%: 0.93-0.96].[37] These values are substantially higher than the alpha angles interobserver/intraobserver ICCs reported by Nepple et al of 0.43/0.92 with 95% CI of [0.35-0.56] and [0.87-0.95], respectively.[37]

Although not extensively reported in literature or used in clinical practice, the TI might be a reliable quantitative imaging parameter. The limitation of the TI is that it only shows the contour of the femoral head-neck region at one position (1/2R from the FHC), which limits clinicians to interpretation of the extent of the cam. Therefore, a future recommendation would be to measure the TI at multiple positions (for example at distances 1/3R, 1/2R and 2/3R from the FHC) to not miss any cam morphology. Additionally, further research should point out the correct threshold and potentially whether there should be location specific, gender-specific or ethnicity-specific thresholds.

To compare the diagnostic performance of alternative parameters and to determine their complementarity in diagnosis, a supervised machine learning approach could be adopted. The machine learning model can be trained with input features, which can include various combinations of alpha angles, triangular indices, head-neck-offset ratios, or any other relevant parameters. The objective of this model training is to accurately classify the morphology as either normal or cam morphology, representing the desired output. By optimizing an objective function through iterative training, supervised learning algorithms can learn a function that predicts the output (diagnosis) for new inputs (feature combinations). As part of the model training process, these algorithms can also rank the features in terms of their importance or contribution to the predictive performance. Combining multiple parameters can potentially improve the diagnostic performance compared to using a single parameter alone. By considering different features simultaneously, the machine learning model can capture complex relationships and interactions among the parameters, leading to more accurate predictions.

7

Conclusion

In this study, a semi-automated workflow for the measurement of alpha angles was developed to facilitate the quantitative evaluation of cam morphology. The workflow is capable of assessing the 3D structure of the femoral head by calculating 12 alpha angles distributed circumferentially around the femoral neck within 26 seconds, automatically outputted in an xlsx file. This represents a time saving of 15 minutes compared to manual measurements. The workflow also automatically generates a polar plot to depict the clockwise morphology of the femoral head neck region, making it interpretable for clinicians. Additionally, novel strategies were incorporated, including radial section-specific spherical least square fitting to approximate the radius of the femoral head, outlier detection to handle surface irregularities and model specific thresholds to account for the asphericity of the femoral head.

The various automatic approaches, depending on which novel strategies were incorporated, demonstrated high mean absolute differences ranging from 20° to 23° and poor level of agreement (ICC range: -0.02 - 0.40) when compared to manual measurements. Alternative studies proposing a semi-automated workflow for alpha angle measurement achieve similar reliability scores ranging from poor-moderate ICCs with the exception of one excellent ICC by *Xia et al.* Quantitative evaluation of the novel strategies did not show any consistent change in performance. Qualitative evaluation found that radius section-specific spherical fitting and outlier detection do have the potential of improving the performance of alpha angle measurements.

The proposed semi-automated workflow could be improved by refining the localization of landmarks, enhancing the quality and segmentation of the ZTE MRI scans using deep learning techniques, and enlarging the dataset used for validation to improve statistical power. Additionally, the propagation of errors resulting from mesh filtering should be taken into account.

This study established that the femoral head is not perfectly spherically shaped, as is assumed in the alpha angle measurement. Variability between and within radial sections of the femoral head were quantitatively demonstrated, and qualitatively, the spheres did not match the contour of the femoral head. Changes in spherical radii of 2-3% due to multiplication of the spherical radius R by a model specific factor, resulted in less accurate cam morphology detection. This revealed the strong reliance of the alpha angle on accurate radius detection. Combining the alpha angle with alternative quantitative imaging parameters for diagnosis of cam morphology, such as the Head Neck Offset Ratio and the Triangular Index, may provide more reliable and consistent measurements than using the alpha angle alone.

Future research should explore the potential of these complementary alternative parameters, as well as the use of statistical shape models that incorporate the imperfect spherical shape of the femoral head. These reference models could be used for registration or the automatic localization of landmarks, axes and regions of interest, feasible when large labelled data sets are available.

As this semi-automated workflow was developed as an open-source software package in Python, researchers can easily modify and adapt it for their own research on FAIS.

Bibliography

[1] Elizabeth Huntoon, Katherine Louise, and Mary Caldwell. “Lower Limb Pain and Dysfunction”. In: Jan. 2021, 727–747.e4. ISBN: 9780323625395. DOI: `10.1016/B978-0-323-62539-5.00036-9`.

[2] Pim van Klij et al. “Cam morphology in young male football players mostly develops before proximal femoral growth plate closure: a prospective study with 5-yearfollow-up”. en. In: *Br. J. Sports Med.* 53.9 (May 2019), pp. 532–538.

[3] Vina P S Tan et al. “Influence of physical activity on bone strength in children and adolescents: a systematic review and narrative synthesis”. en. In: *J. Bone Miner. Res.* 29.10 (Oct. 2014), pp. 2161–2181.

[4] D R Griffin et al. “The Warwick Agreement on femoroacetabular impingement syndrome (FAI syndrome): an international consensus statement”. en. In: *Br. J. Sports Med.* 50.19 (Oct. 2016), pp. 1169–1176.

[5] Pim van Klij et al. “Classifying Cam Morphology by the Alpha Angle: A Systematic Review on Threshold Values”. In: *Orthopaedic Journal of Sports Medicine* 8.8 (Aug. 2020), p. 232596712093831. DOI: `10.1177/2325967120938312`. URL: `https://doi.org/10.1177/2325967120938312`.

[6] Cristián Barrientos et al. “Is there a pathological alpha angle for hip impingement? A diagnostic test study”. In: *Journal of Hip Preservation Surgery* 3.3 (Apr. 2016), pp. 223–228. DOI: `10.1093/jhps/hnw014`. URL: `https://doi.org/10.1093/jhps/hnw014`.

[7] H. P. Notzli et al. “The contour of the femoral head-neck junction as a predictor for the risk of anterior impingement”. In: *The Journal of Bone and Joint Surgery. British volume* 84-B.4 (May 2002), pp. 556–560. DOI: `10.1302/0301-620x.84b4.0840556`. URL: `https://doi.org/10.1302/0301-620x.84b4.0840556`.

[8] Kawan S. Rakhra et al. “Comparison of MRI Alpha Angle Measurement Planes in Femoroacetabular Impingement”. In: *Clinical Orthopaedics &amp Related Research* 467.3 (Mar. 2009), pp. 660–665. DOI: `10.1007/s11999-008-0627-3`. URL: `https://doi.org/10.1007/s11999-008-0627-3`.

[9] Ying Xia et al. “Automated 3D quantitative assessment and measurement of alpha angles from the femoral head-neck junction using MR imaging”. en. In: *Phys. Med. Biol.* 60.19 (Oct. 2015), pp. 7601–7616.

[10] Ryan E. Breighner et al. “Evaluation of Osseous Morphology of the Hip Using Zero Echo Time Magnetic Resonance Imaging”. In: *The American Journal of Sports Medicine* 47.14 (Oct. 2019), pp. 3460–3468. DOI: `10.1177/0363546519878170`. URL: `https://doi.org/10.1177/0363546519878170`.

[11] Ricardo Andrade Fernandes de Mello et al. “Three-Dimensional Zero Echo Time Magnetic Resonance Imaging Versus 3-Dimensional Computed Tomography for Glenoid Bone Assessment”. In: *Arthroscopy: The Journal of Arthroscopic &amp Related Surgery* 36.9 (Sept. 2020), pp. 2391–2400. DOI: `10.1016/j.arthro.2020.05.042`. URL: `https://doi.org/10.1016/j.arthro.2020.05.042`.

[12] A. Lu, K.R. Gorny, and M.-L. Ho. “Zero TE MRI for Craniofacial Bone Imaging”. In: *American Journal of Neuroradiology* (Aug. 2019). DOI: `10.3174/ajnr.a6175`. URL: `https://doi.org/10.3174/ajnr.a6175`.

[13] Emil Ljungberg et al. “Silent zero TE MR neuroimaging: Current state-of-the-art and future directions”. In: *Progress in Nuclear Magnetic Resonance Spectroscopy* 123 (Apr. 2021), pp. 73–93. DOI: `10.1016/j.pnmrs.2021.03.002`. URL: `https://doi.org/10.1016/j.pnmrs.2021.03.002`.

[14] Pim van Klij et al. “The Prevalence of Cam and Pincer Morphology and Its Association With Development of Hip Osteoarthritis”. In: *Journal of Orthopaedic &amp Sports Physical Therapy* 48.4 (Apr. 2018), pp. 230–238. DOI: `10.2519/jospt.2018.7816`. URL: `https://doi.org/10.2519/jospt.2018.7816`.

[15] Python Core Team. *Python: A dynamic, open source programming language*. Python version 3.9. Python Software Foundation. 2019. URL: `https://www.python.org/`.

[16] Lauren N. Heckelman et al. “Design and validation of a semi-automatic bone segmentation algorithm from MRI to improve research efficiency”. In: *Scientific Reports* 12.1 (May 2022). DOI: `10.1038/s41598-022-11785-6`. URL: `https://doi.org/10.1038/s41598-022-11785-6`.

[17] Florian Wiesinger et al. “Zero TEMR bone imaging in the head”. In: *Magnetic Resonance in Medicine* 75.1 (Jan. 2015), pp. 107–114. DOI: `10.1002/mrm.25545`. URL: `https://doi.org/10.1002/mrm.25545`.

[18] Icometrix. *Icometrix/DICOM2NIFTI*. URL: `https://github.com/icometrix/dicom2nifti`.

[19] Jaber Juntu et al. “Bias Field Correction for MRI Images”. In: *Advances in Soft Computing*. Springer Berlin Heidelberg, pp. 543–551. DOI: `10.1007/3-540-32390-2_64`. URL: `https://doi.org/10.1007/3-540-32390-2_64`.

[20] URL: `https://simpleitk.org/doxygen/latest/html/classitk_1_1simple_1_1N4BiasFieldCorrectionImageFi` `html`.

[21] Aryaman Sharda. *Image Filters: Gaussian Blur — aryamansharda.medium.com*. `https://aryamansharda.medium.com/image-filters-gaussian-blur-eb36db6781b1`. [Accessed 09-May-2023].

[22] Prabhavi Jayanetti. *Remove Salt and Pepper noise with Median Filtering — medium.com*. `https://medium.com/analytics-vidhya/remove-salt-and-pepper-noise-with-median-filtering-b739614fe9db`. [Accessed 09-May-2023].

[23] Sunil Yadav. *Speckle vs Gaussian Noise? — sunil7545*. `https://medium.com/@sunil7545/speckle-vs-gaussian-noise-7f4f47230d82`. [Accessed 09-May-2023].

[24] G. Bradski. “The OpenCV Library”. In: *Dr. Dobb’s Journal of Software Tools* (2000).

[25] Maria Petrou and Costas Petrou. *Image Processing: The Fundamentals*. Wiley, Apr. 2010. DOI: `10.1002/9781119994398`. URL: `https://doi.org/10.1002/9781119994398`.

[26] *Marching Cubes — cs.carleton.edu*. `https://www.cs.carleton.edu/cs_comps/0405/shape/marching_cubes.html`. [Accessed 09-May-2023].

[27] Noémie Bonneau et al. “A three-dimensional axis for the study of femoral neck orientation”. In: *Journal of Anatomy* 221.5 (Sept. 2012), pp. 465–476. DOI: `10.1111/j.1469-7580.2012.01565.x`. URL: `https://doi.org/10.1111/j.1469-7580.2012.01565.x`.

[28] Charles Jekel. *Least squares sphere fit*. URL: `https://jekel.me/2015/Least-Squares-Sphere-Fit/`.

[29] Wuyang Li. *Point Cloud Sphere Fitting*. Nov. 2020. URL: `https://wuyang-li1990.medium.com/point-cloud-sphere-fitting-cc619c0f7ced`.

[30] Shane Hanzlik et al. “The Prevalence of Cam Morphology: A Cross-Sectional Evaluation of 3, 558 Cadaveric Femora”. In: *Frontiers in Surgery* 7 (Jan. 2021). DOI: `10.3389/fsurg.2020.588535`. URL: `https://doi.org/10.3389/fsurg.2020.588535`.

[31] Charles R. Harris et al. “Array programming with NumPy”. In: *Nature* 585.7825 (Sept. 2020), pp. 357–362. DOI: `10.1038/s41586-020-2649-2`. URL: `https://doi.org/10.1038/s41586-020-2649-2`.

[32] Raphael Vallat. “Pingouin: statistics in Python”. In: *The Journal of Open Source Software* 3.31 (Nov. 2018), p. 1026.

[33] Terry K. Koo and Mae Y. Li. “A Guideline of Selecting and Reporting Intraclass Correlation Coefficients for Reliability Research”. en. In: *Journal of Chiropractic Medicine* 15.2 (June 2016), pp. 155–163. ISSN: 1556-3707. DOI: `10.1016/j.jcm.2016.02.012`. URL: `https://www.sciencedirect.com/science/article/pii/S1556370716000158` (visited on 03/23/2023).

[34] J. D. Hunter. “Matplotlib: A 2D graphics environment”. In: *Computing in Science & Engineering* 9.3 (2007), pp. 90–95. DOI: `10.1109/MCSE.2007.55`.

[35] Guodong Zeng et al. “MRI-based 3D models of the hip joint enables radiation-free computer-assisted planning of periacetabular osteotomy for treatment of hip dysplasia using deep learning for automatic segmentation”. In: *European Journal of Radiology Open* 8 (2021), p. 100303. DOI: `10.1016/j.ejro.2020.100303`. URL: `https://doi.org/10.1016/j.ejro.2020.100303`.

[36] Mario Botsch et al. *Polygon Mesh Processing*. A K Peters/CRC Press, Oct. 2010. DOI: `10.1201/b10688`. URL: `https://doi.org/10.1201/b10688`.

[37] Jeffrey J. Nepple et al. “Interobserver and Intraobserver Reliability of the Radiographic Analysis of Femoroacetabular Impingement and Dysplasia Using Computer-Assisted Measurements”. In: *The American Journal of Sports Medicine* 42.10 (Aug. 2014), pp. 2393–2401. DOI: `10.1177/0363546514542797`. URL: `https://doi.org/10.1177/0363546514542797`.

[38] Marc Fischer et al. “Automated Morphometric Analysis of the Hip Joint on MRI from the German National Cohort Study”. In: *Radiology: Artificial Intelligence* 3.5 (Sept. 2021), e200213. DOI: `10.1148/ryai.2021200213`. URL: `https://doi.org/10.1148/ryai.2021200213`.

[39] Nastassja Pamela Ewertowski et al. “Automated measurement of alpha angle on 3D-magnetic resonance imaging in femoroacetabular impingement hips: a pilot study”. In: *Journal of Orthopaedic Surgery and Research* 17.1 (July 2022). DOI: `10.1186/s13018-022-03256-5`. URL: `https://doi.org/10.1186/s13018-022-03256-5`.

[40] Ying Xia et al. “Automated 3D quantitative assessment and measurement of alpha angles from the femoral head-neck junction using MR imaging”. In: *Physics in Medicine and Biology* 60.19 (Sept. 2015), pp. 7601–7616. DOI: `10.1088/0031-9155/60/19/7601`. URL: `https://doi.org/10.1088/0031-9155/60/19/7601`.

[41] Xinzeng Wang et al. “Novel deep learning-based noise reduction technique for prostate magnetic resonance imaging”. In: *Abdominal Radiology* 46.7 (Feb. 2021), pp. 3378–3386. DOI: `10.1007/s00261-021-02964-6`. URL: `https://doi.org/10.1007/s00261-021-02964-6`.

[42] K. K. Gosvig et al. “A new radiological index for assessing asphericity of the femoral head in cam impingement”. In: *The Journal of Bone and Joint Surgery. British volume* 89-B.10 (Oct. 2007), pp. 1309–1316. DOI: `10.1302/0301-620x.89b10.19405`. URL: `https://doi.org/10.1302/0301-620x.89b10.19405`.

[43] Alex S. Nicholls et al. “The association between hip morphology parameters and nineteen-year risk of end-stage osteoarthritis of the hip: A nested case–control study”. In: *Arthritis &amp Rheumatism* 63.11 (Oct. 2011), pp. 3392–3400. DOI: `10.1002/art.30523`. URL: `https://doi.org/10.1002/art.30523`.

[44] Sobechukwu W I Onwuzu et al. “Normative values of the alpha angle and triangular index measured from the hip radiographs of an African population”. In: *Journal of Medical Imaging and Radiation Sciences* 53.4 (Dec. 2022), pp. 681–685. DOI: `10.1016/j.jmir.2022.09.023`. URL: `https://doi.org/10.1016/j.jmir.2022.09.023`.

[45] Fernando Nemtala, Rodrigo M Mardones, and Alexander Tomic. “Anterior and posterior femoral head-neck offset ratio in the cam impingement”. en. In: *Cartilage* 1.3 (July 2010), pp. 238–241.

8

Appendix A: Bland Altman Plots

This appendix includes bland altman plots depicting the agreement between manual measurements and each different automatic approach. The automatic approach with the highest ICC of 0.40 using no outlier detection and no model specific factor (MSF) is presented already in the main body of this thesis and therefore is not presented in this appendix (Section 5.3). Each approach depends on the number of subsequent angles (SA) set as condition to detect outliers (SA = 1, 5, 10 or 20) and the threshold that was used. The threshold is either the radius of the fitted sphere or the radius of the fitted sphere multiplied by the MSF. The title of each subsection specifies the used automatic approach.

8.1. SA = 5 and Threshold = Radius fitted sphere

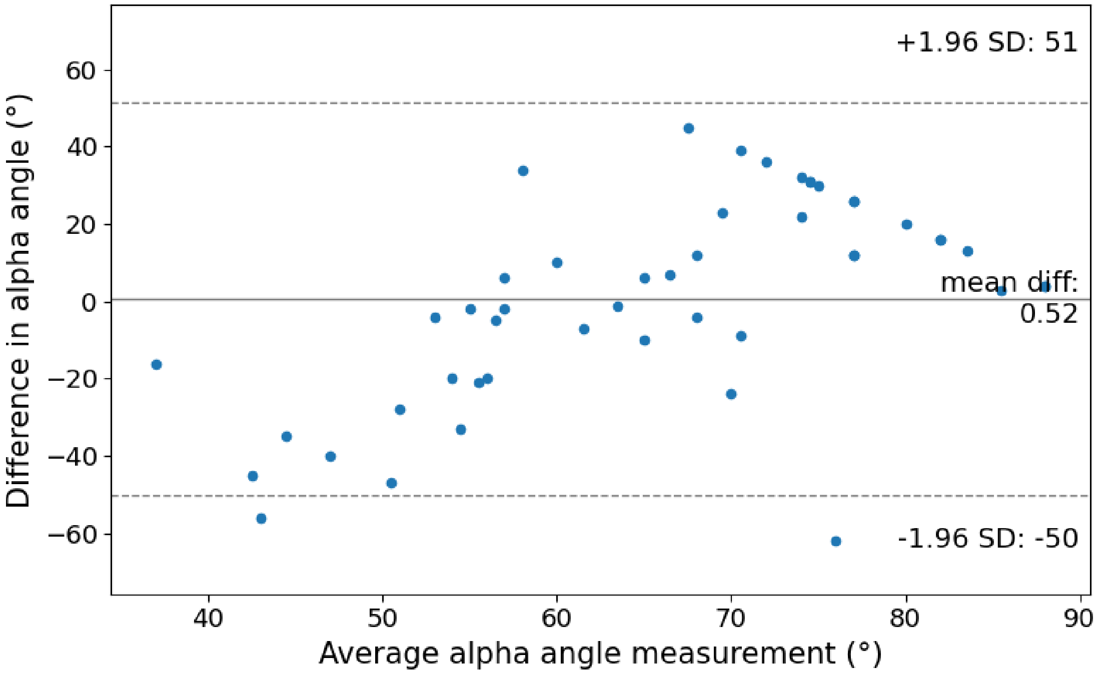

Figure 8.1: Bland-Altman plot depicting the agreement on manual alpha angle measurement by an MSK radiologist and automatic alpha angle measurement computed by a workflow. The dotted lines indicate the 1.96 standard deviation with an upper boundary of 51 and a lower boundary of -50. The middle grey line indicates the mean difference of 0.52.

8.2. SA = 10 and Threshold = Radius fitted sphere

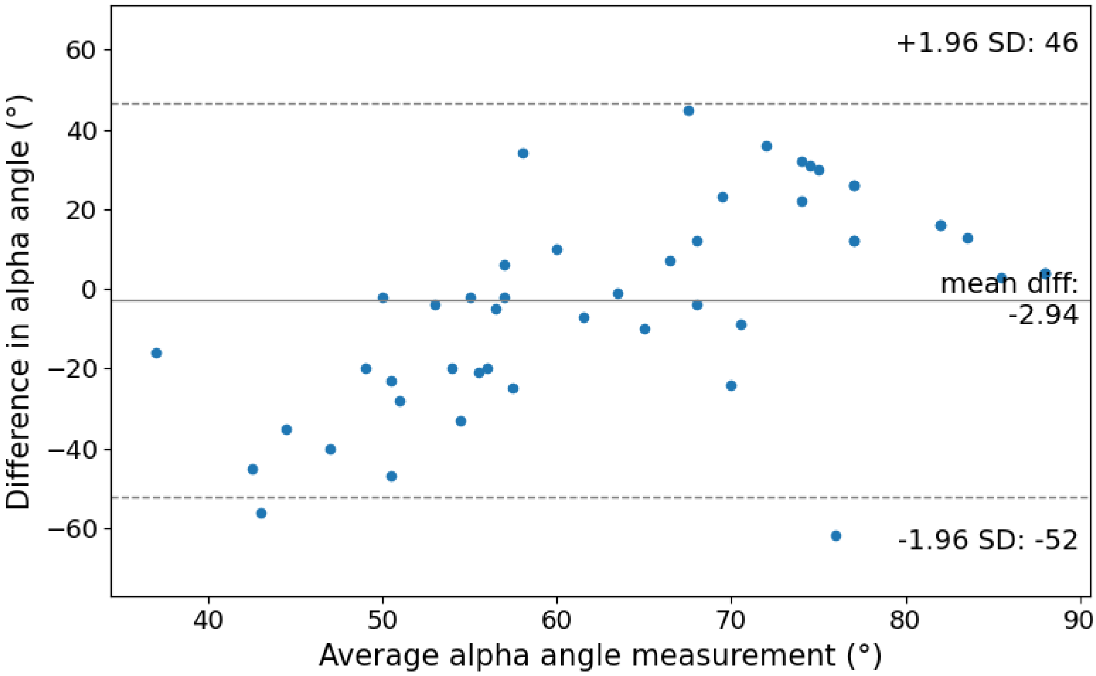

Figure 8.2: Bland-Altman plot depicting the agreement on manual alpha angle measurement by an MSK radiologist and automatic alpha angle measurement computed by a workflow. The dotted lines indicate the 1.96 standard deviation with an upper boundary of 46 and a lower boundary of -52. The middle grey line indicates the mean difference of -2.94

8.3. SA = 20 and Threshold = Radius fitted sphere

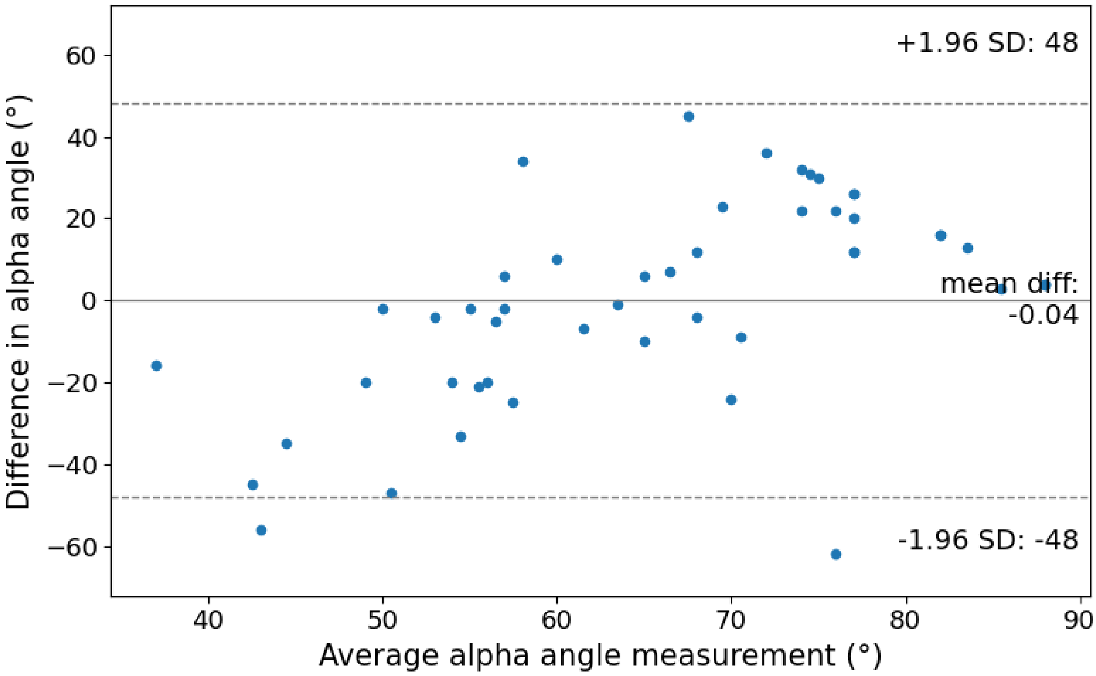

Figure 8.3: Bland-Altman plot depicting the agreement on manual alpha angle measurement by an MSK radiologist and automatic alpha angle measurement computed by a workflow. The dotted lines indicate the 1.96 standard deviation with an upper boundary of 48 and a lower boundary of -48. The middle grey line indicates the mean difference of -0.04.

8.4. SA = 1 and Threshold = Radius fitted sphere * MSF

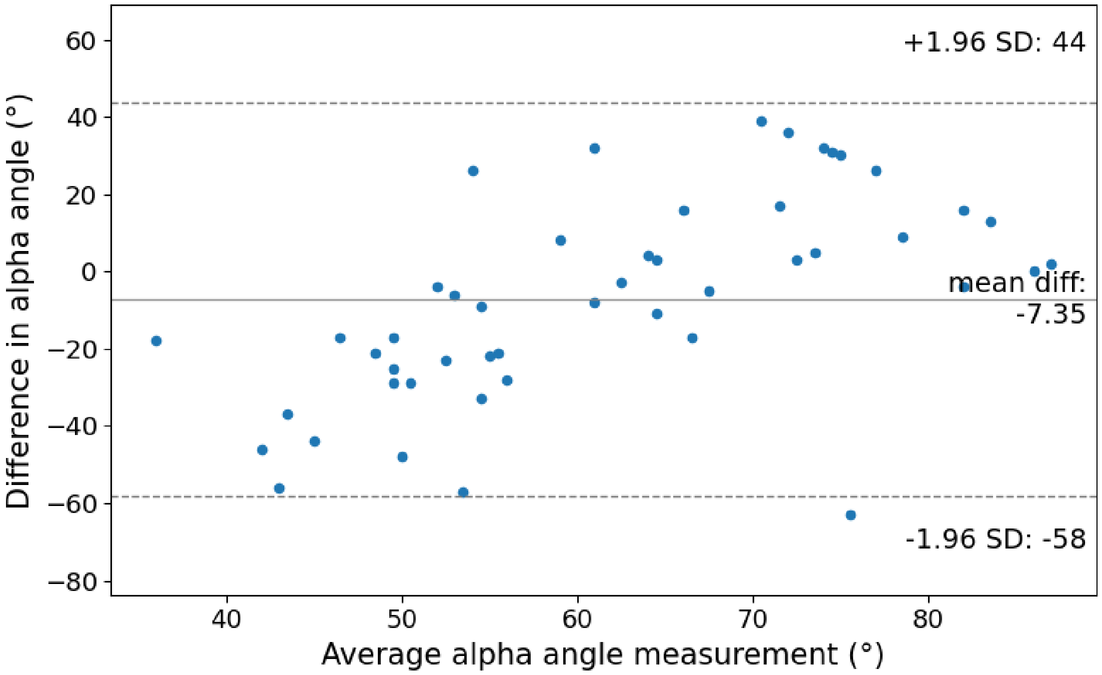

Figure 8.4: Bland-Altman plot depicting the agreement on manual alpha angle measurement by an MSK radiologist and automatic alpha angle measurement computed by a workflow. The dotted lines indicate the 1.96 standard deviation with an upper boundary of 44 and a lower boundary of -58. The middle grey line indicates the mean difference of -7.35.

8.5. SA = 5 and Threshold = Radius fitted sphere * MSF

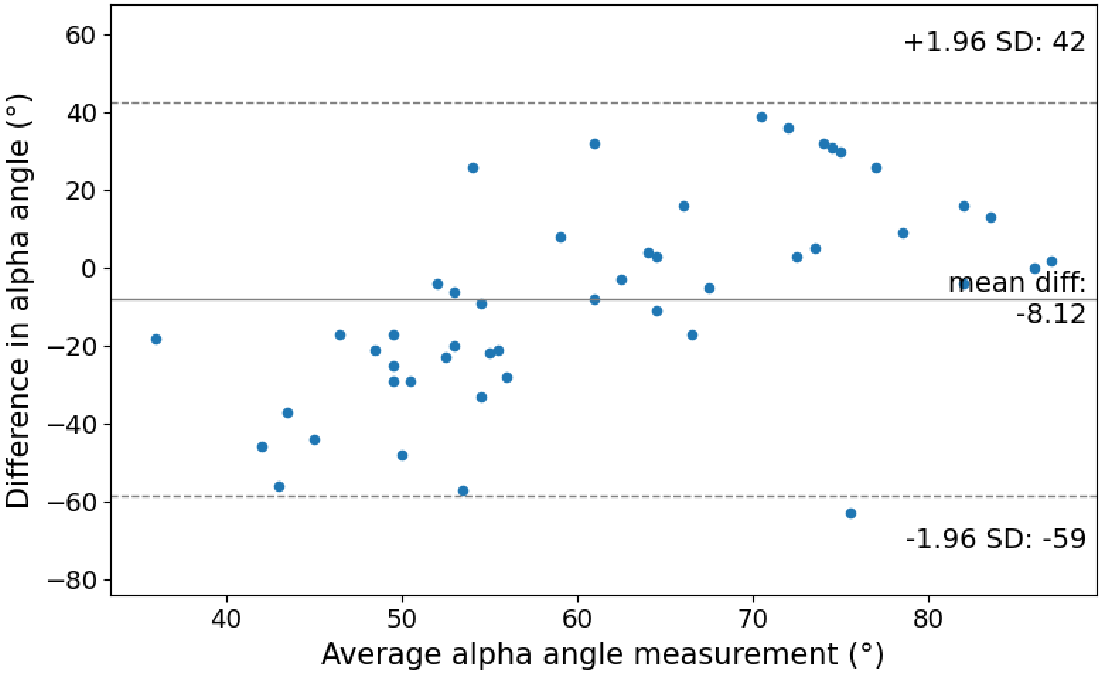

Figure 8.5: Bland-Altman plot depicting the agreement on manual alpha angle measurement by an MSK radiologist and automatic alpha angle measurement computed by a workflow. The dotted lines indicate the 1.96 standard deviation with an upper boundary of 42 and a lower boundary of -59. The middle grey line indicates the mean difference of -8.12.

8.6. SA = 10 and Threshold = Radius fitted sphere * MSF

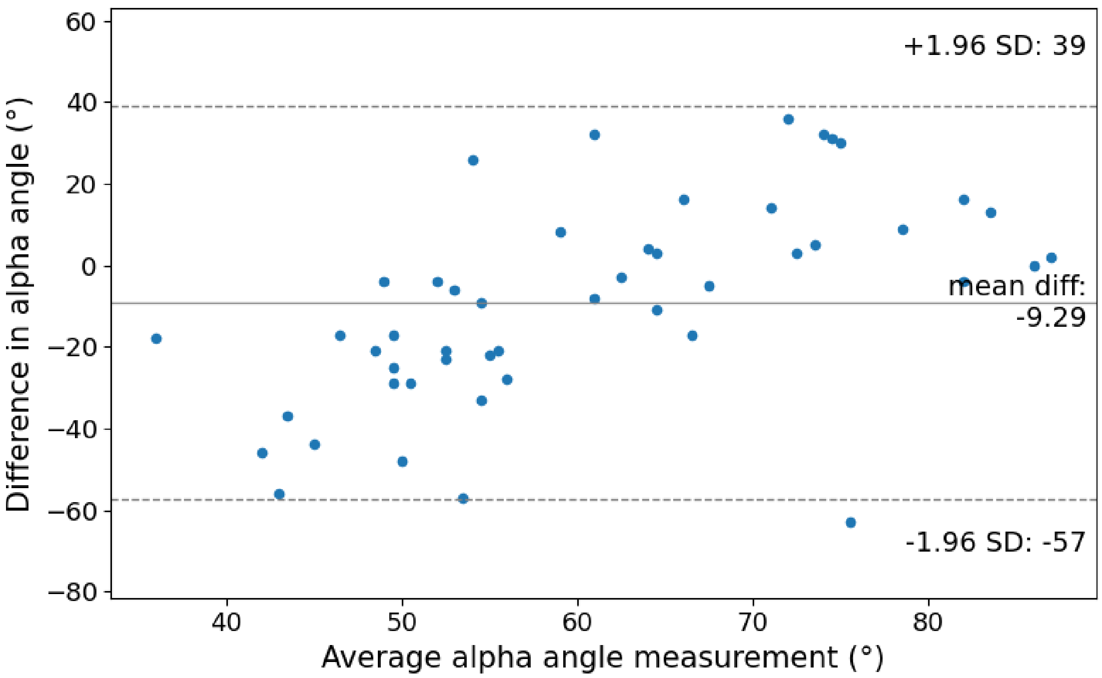

Figure 8.6: Bland-Altman plot depicting the agreement on manual alpha angle measurement by an MSK radiologist and automatic alpha angle measurement computed by a workflow. The dotted lines indicate the 1.96 standard deviation with an upper boundary of 39 and a lower boundary of -57. The middle grey line indicates the mean difference of -9.29.

8.7. SA = 20 and Threshold = Radius fitted sphere * MSF

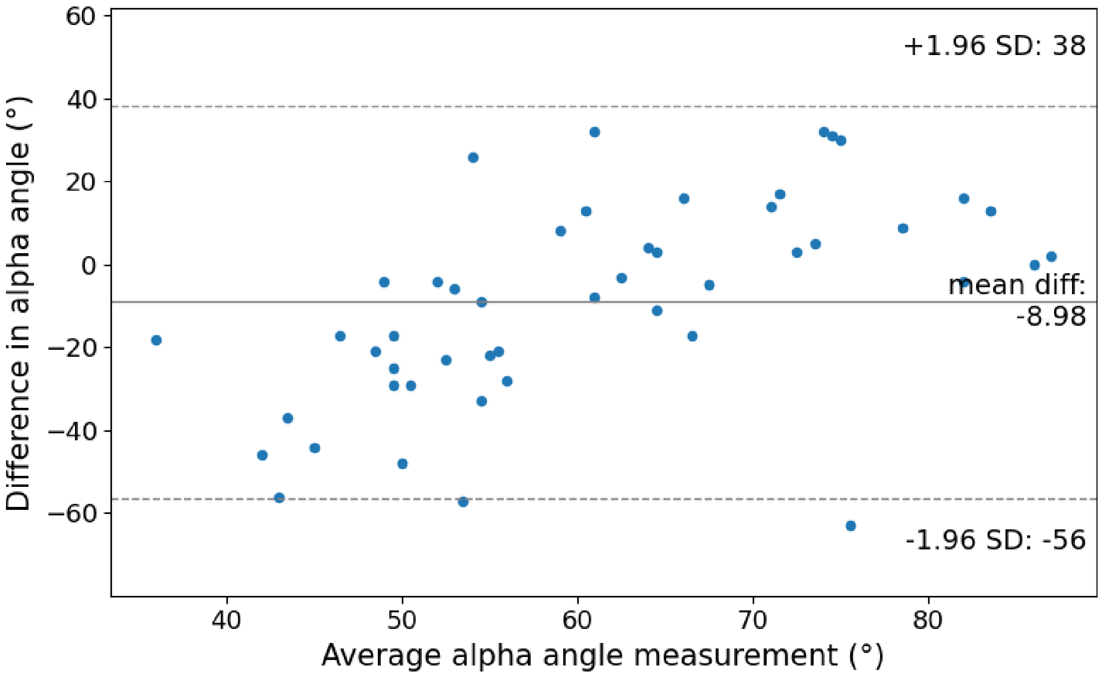

Figure 8.7: Bland-Altman plot depicting the agreement on manual alpha angle measurement by an MSK radiologist and automatic alpha angle measurement computed by a workflow. The dotted lines indicate the 1.96 standard deviation with an upper boundary of 38 and a lower boundary of -56. The middle grey line indicates the mean difference of -8.98.

9

Appendix B: Individual patient data

This appendix presents polar plots for each 3D hip model, displaying alpha angle measurements computed using different semi-automated methods alongside manual measurements for 6 radial positions (brown dots). The semi-automated alpha angle measurements are represented in blue for 12 clockwise positions, and the alpha angle threshold of 60° is marked by a green circle. A polar plot is generated for each automatic approach, which varies by the number of subsequent inclination angles (n = 1,5,10,20) for outlier detection and includes or excludes a multiplication of the radius by the model specific factor (MSF), ranging from 1.02 to 1.03.

All polar plots for each 3D hip model are qualitatively evaluated in this appendix. A bar graph has been created that summarizes this qualitative evaluation, to be found in the main body of the thesis (Section 5.2).

Patient 28: Left hip)

The 3D model of the left hip of patient 28 shows a slight supero- anterior cam morphology with an additional bony protrusion localized posterior. The manual measurements indicated minor exceeding alpha angles at the superior and inferior side whereas the workflow (Factor = 1.02-1.03) localized prominent exceeding alpha angles at the supero-posterior and supero-anterior side for all subsequent angles. The workflow (Factor = 1.0) additionally indicates the presence of a bony protrusion antero-inferior. Subsequent outlier detection does not show any effect in the workflow (factor = 1.0) whereas only one outlier at 3:00 o'clock seems to be detected for the workflow (factor = 1.02-1.03) when the condition is set to n=20 subsequent exceeding inclination angles.

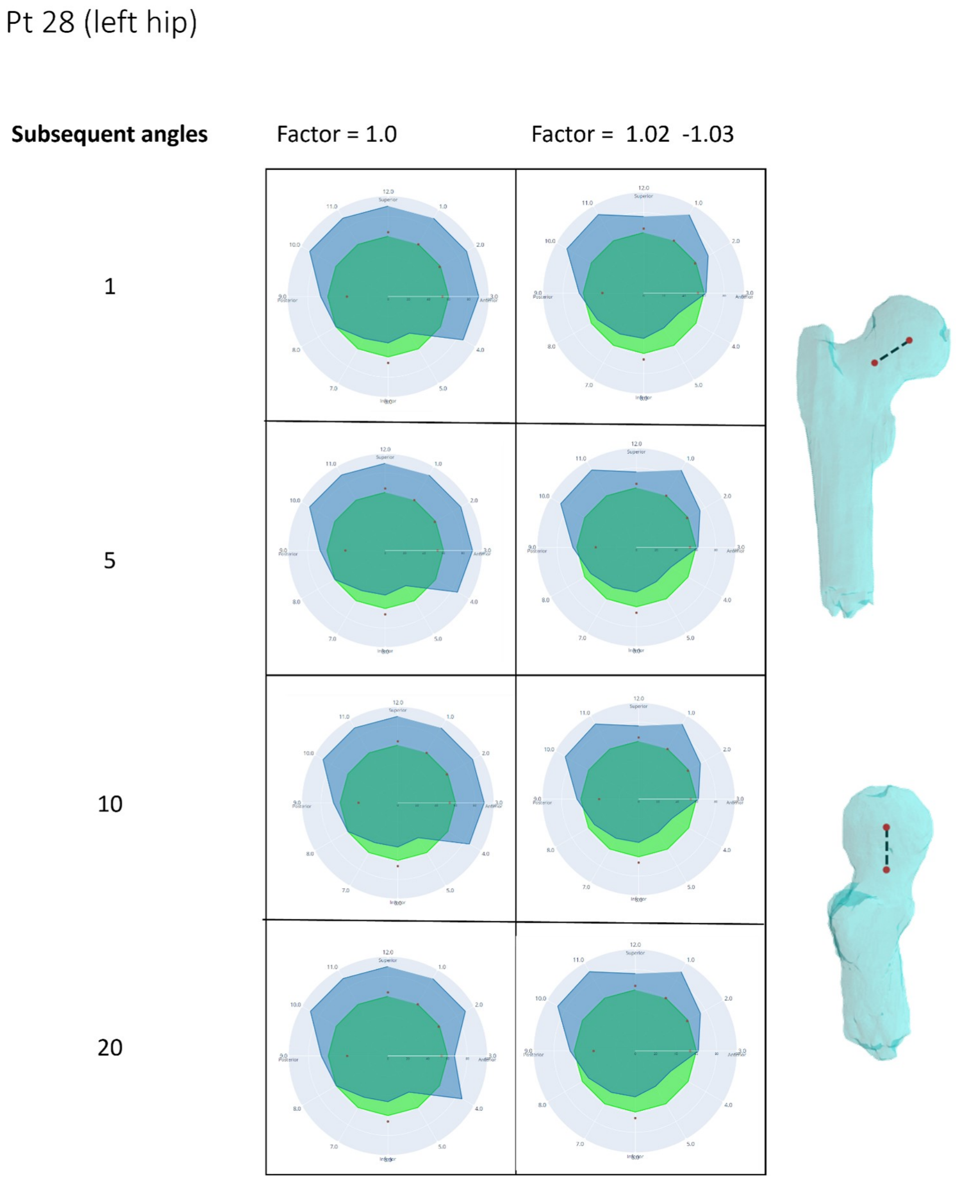

Figure 9.1: Polar plots depicting various alpha angle measurements of the left hip of patient 28: the manual alpha angle measurements for 6 radial positions are depicted by the brown dots. The semi-automated alpha angle measurements are depicted in blue for 12 clockwise positions. The green circle represents the alpha angle threshold of 60 degrees. A polar plot is generated for each different automatic approach: varying the number of subsequent inclination angles for outlier detection and whether there is additional multiplication of the radius by a model specific factor.

Patient 28: Right hip

The 3D model of the left hip of patient 28 shows a very slight anterior bony protrusion. The radiologist localized slight exceeding alpha angles at the antero-superior side. The workflow (Factor = 1.0) localized the exceeding alpha angles at both the anterior and posterior side. The workflow (Factor = 1.02-1.03) only detects exceeding alpha angles at 2:00 o'clock and 8:00 o'clock, being located supero-anterior and posterior. Outlier detection detects some of the outliers, being posterior located.

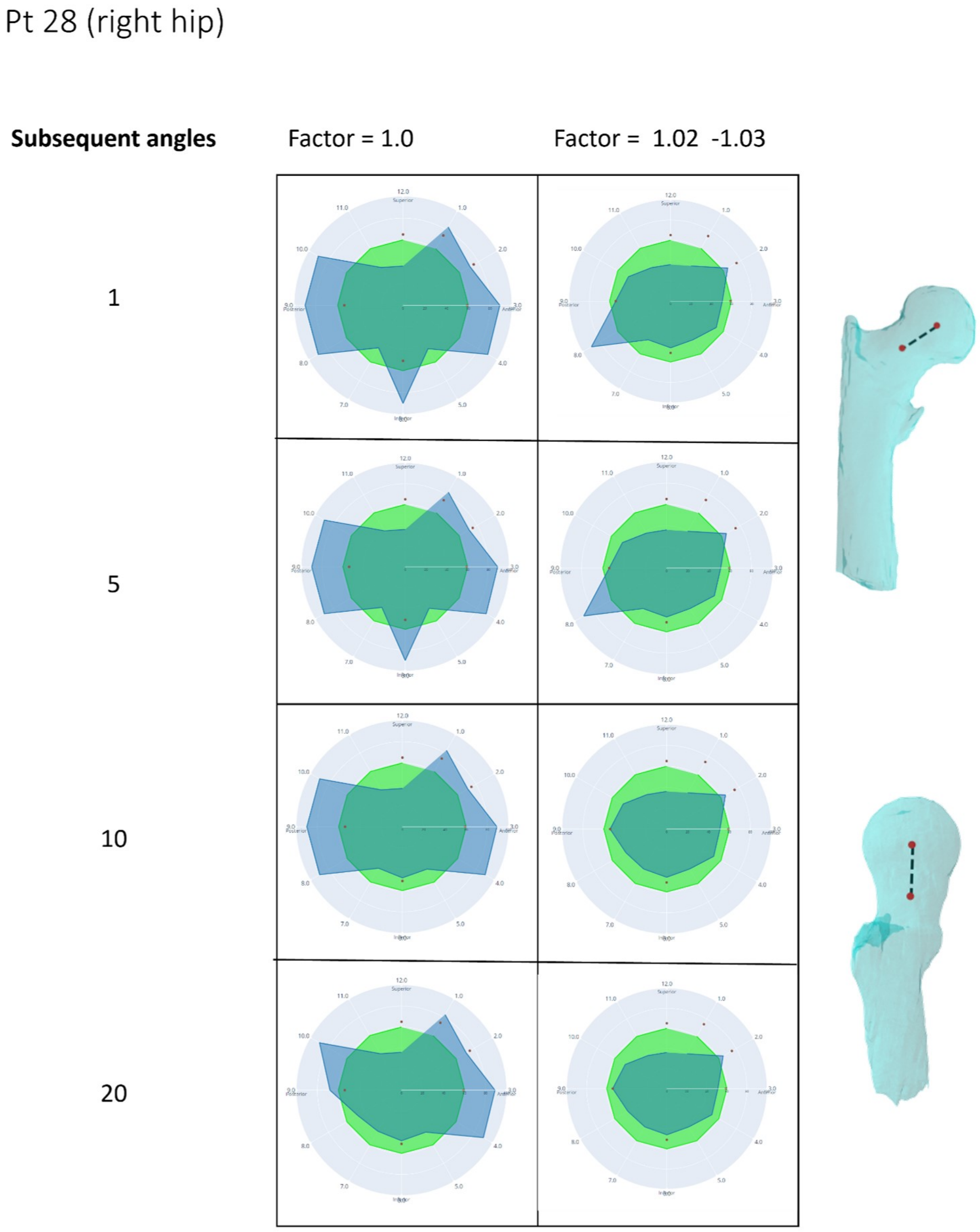

Figure 9.2: Polar plots depicting various alpha angle measurements of the right hip of patient 28: the manual alpha angle measurements for 6 radial positions are depicted by the brown dots. The semi-automated alpha angle measurements are depicted in blue for 12 clockwise positions. The green circle represents the alpha angle threshold of 60 degrees. A polar plot is generated for each different automatic approach: varying the number of subsequent inclination angles for outlier detection and whether there is additional multiplication of the radius by a model specific factor.

Patient 33: Left hip

The 3D model of the left hip of patient 33 shows a prominent anterior bony protrusion. The manual measurements indicated prominent exceeding alpha angles at the anterior-superior side and a minor exceeding alpha angle at 6:00 o'clock (inferior). The workflow (Factor = 1.0) localized the exceeding alpha angles at supero-anterior infero-anterior with outlier detection detecting some outliers postero-inferior. The workflow (Factor = 1.02- 1.03) localized the exceeding alpha angles also supero-anterior and infero-anterior with outlier detection detecting making no difference.

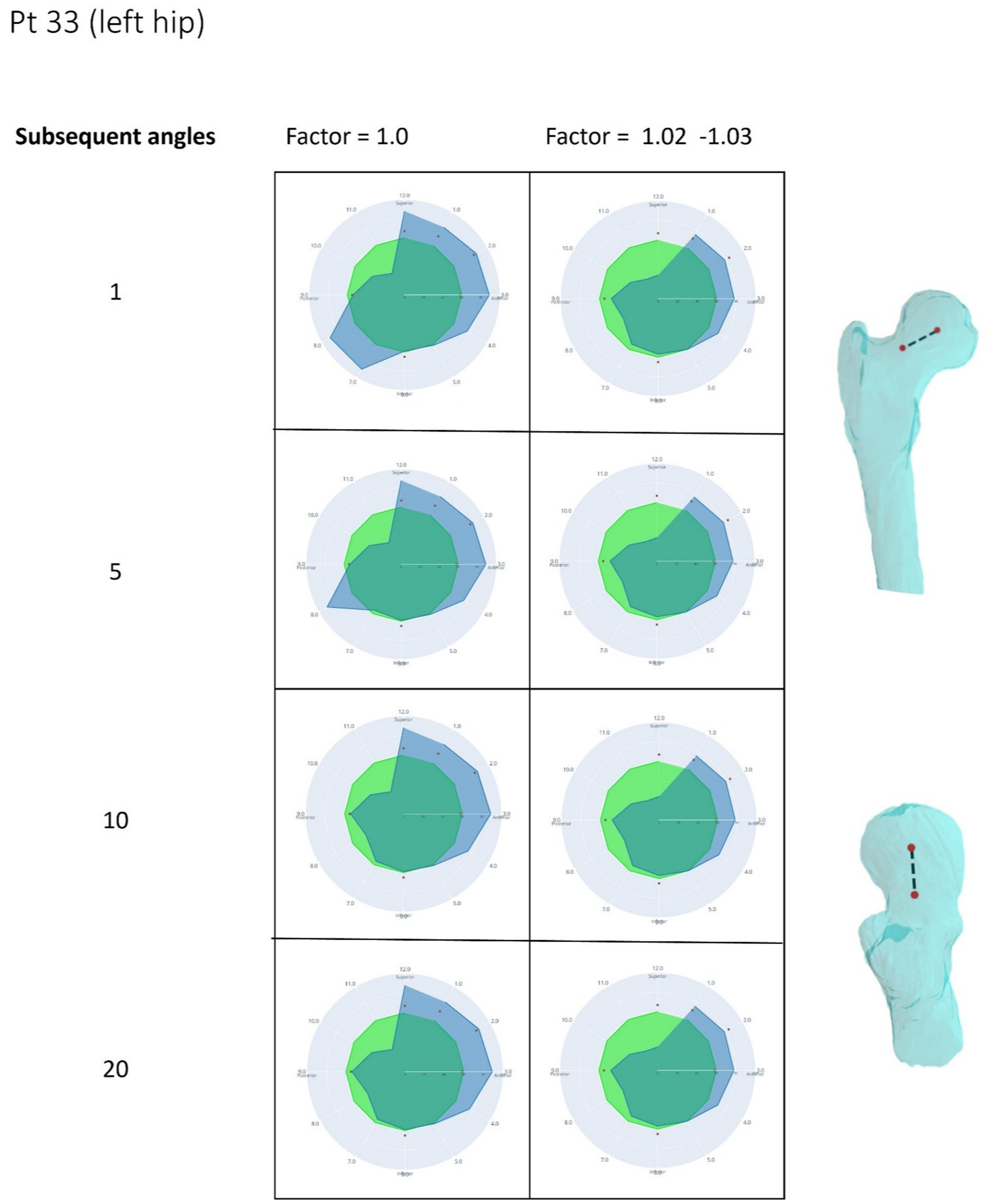

Figure 9.3: Polar plots depicting various alpha angle measurements of the left hip of patient 33: the manual alpha angle measurements for 6 radial positions are depicted by the brown dots. The semi-automated alpha angle measurements are depicted in blue for 12 clockwise positions. The green circle represents the alpha angle threshold of 60 degrees. A polar plot is generated for each different automatic approach: varying the number of subsequent inclination angles for outlier detection and whether there is additional multiplication of the radius by a model specific factor.

Patient 33 Right hip

The 3D model of the right hip of patient 33 shows a prominent anterior bony protrusion. The radiologist localized exceeding alpha angles at the antero-superior side. The workflow (Factor = 1.0 and Factor = 1.02-1.03) localized the exceeding alpha angles at the anterior side. Outlier detection locates a posterior outlier at 8:00 o'clock with 5 subsequent inclination angles set as condition to exceed the threshold.

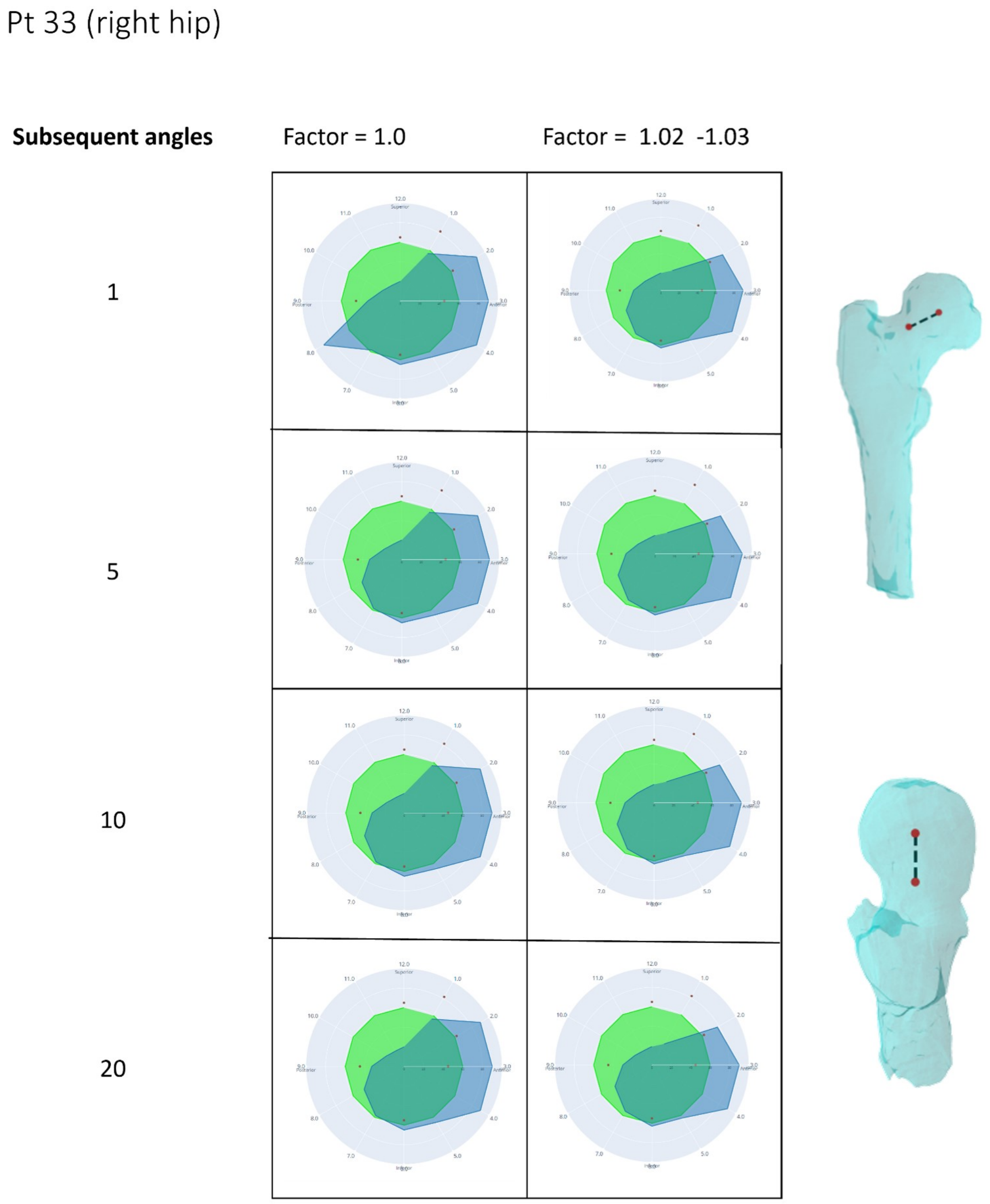

Figure 9.4: Polar plots depicting various alpha angle measurements of the right hip of patient 33: the manual alpha angle measurements for 6 radial positions are depicted by the brown dots. The semi-automated alpha angle measurements are depicted in blue for 12 clockwise positions. The green circle represents the alpha angle threshold of 60 degrees. A polar plot is generated for each different automatic approach: varying the number of subsequent inclination angles for outlier detection and whether there is additional multiplication of the radius by a model specific factor.

Patient 45: Left hip

The 3D model of the left hip of patient 45 shows a normal morphology of the femoral head. Manual measurements in the polar plot indicate slight exceeding alpha angles at the antero-superior side. The workflow (Factor = 1.0 and 1.02-1.03) both localize exceeding alpha angles at the postero-inferior side with workflow (Factor = 1.0) also showing a bony protrusion at the antero-inferior side. After outlier detection with 20 subsequent alpha angles, no exceeding alpha angles remain, corresponding to a normal morphology of the femoral head.

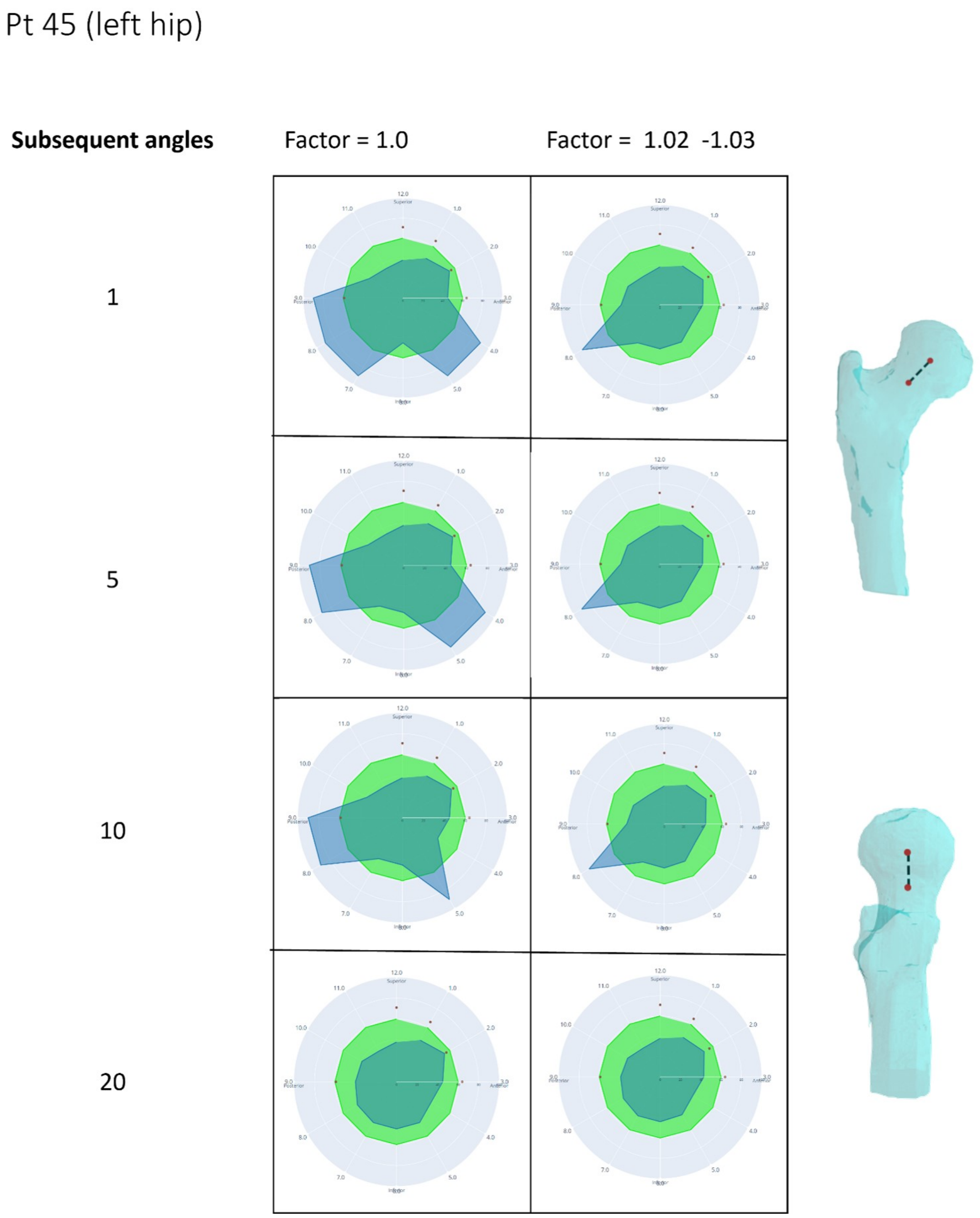

Figure 9.5: Polar plots depicting various alpha angle measurements of the left hip of patient 45: the manual alpha angle measurements for 6 radial positions are depicted by the brown dots. The semi-automated alpha angle measurements are depicted in blue for 12 clockwise positions. The green circle represents the alpha angle threshold of 60 degrees. A polar plot is generated for each different automatic approach: varying the number of subsequent inclination angles for outlier detection and whether there is additional multiplication of the radius by a model specific factor.

Patient 45: Right hip

The 3D model of the right hip of patient 45 shows a slight anterior bony protrusion. Manual measurements in the polar plot indicate prominent exceeding alpha angles at the antero-superior side. The workflow (Factor = 1.0 and 1.02-1.03) localized exceeding alpha angles at both the antero-inferior and postero-inferior side. Outlier detection indicates posterior exceeding alpha angles to be outliers. For workflow (Factor = 1.0) an antero-inferior exceeding alpha angle remains whereas workflow (factor 1.02-1.03) indicates no exceeding alpha angles after outlier detection, suggesting a normal morphology.

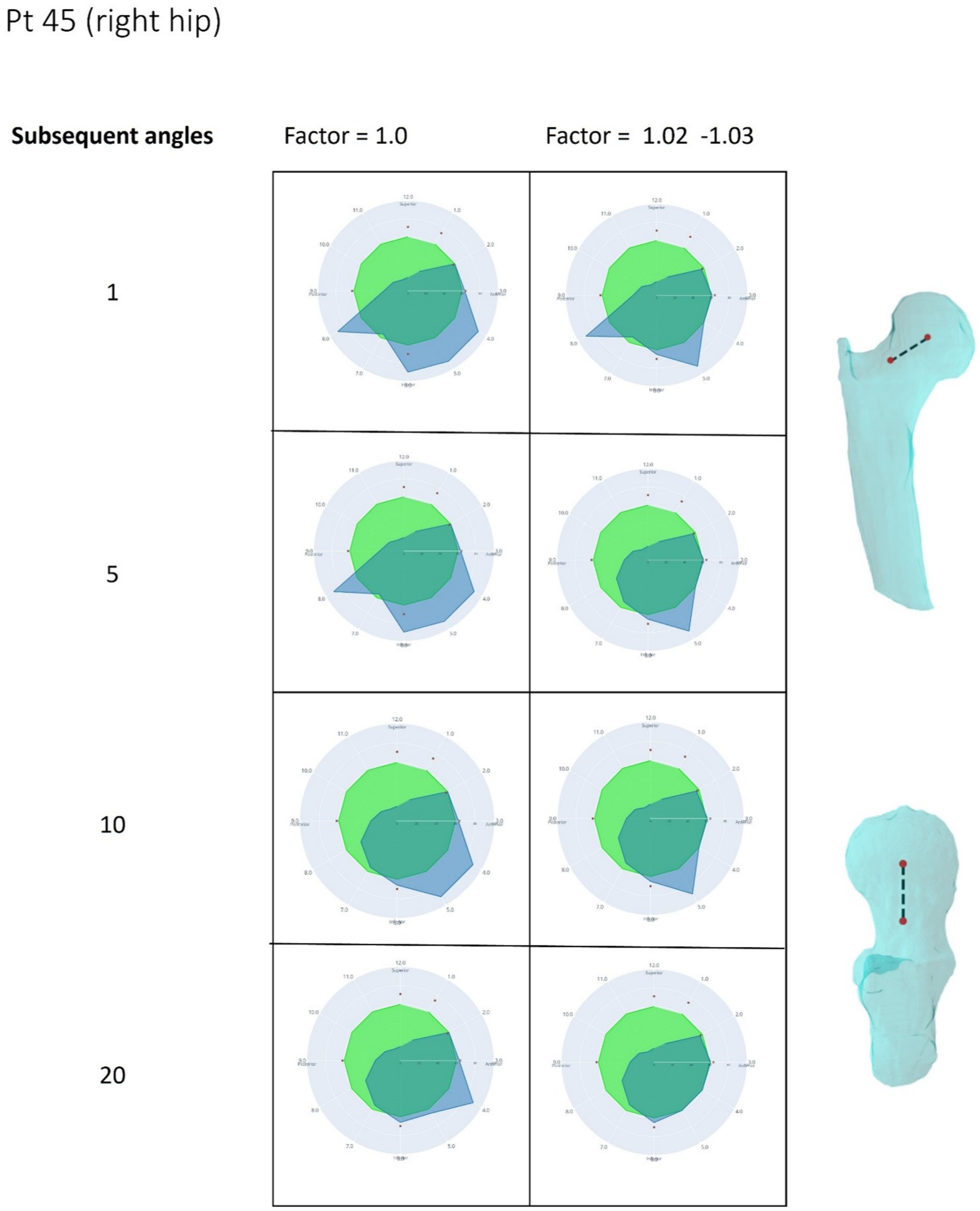

Figure 9.6: Polar plots depicting various alpha angle measurements of the right hip of patient 45: the manual alpha angle measurements for 6 radial positions are depicted by the brown dots. The semi-automated alpha angle measurements are depicted in blue for 12 clockwise positions. The green circle represents the alpha angle threshold of 60 degrees. A polar plot is generated for each different automatic approach: varying the number of subsequent inclination angles for outlier detection and whether there is additional multiplication of the radius by a model specific factor.

Patient 67: Left hip

The 3D model of the left hip of patient 67 shows a slight anterior bony protrusion. The radiologist localized prominent exceeding alpha angles at the antero-superior side, postero-superior side and inferior side. The workflow (Factor = 1.0) localized the exceeding alpha angles almost circumferential except for postero-inferior with outlier detection only suggesting inferiorly there is an outlier. The workflow (Factor = 1.02-1.03) has a similar pattern, but less prominent alpha angles are computed in comparison to the workflow (Factor = 1.0). The manual and semi-automated measurements correspond regarding location, but both do not correspond to with what is visually seen on the 3D hip model.

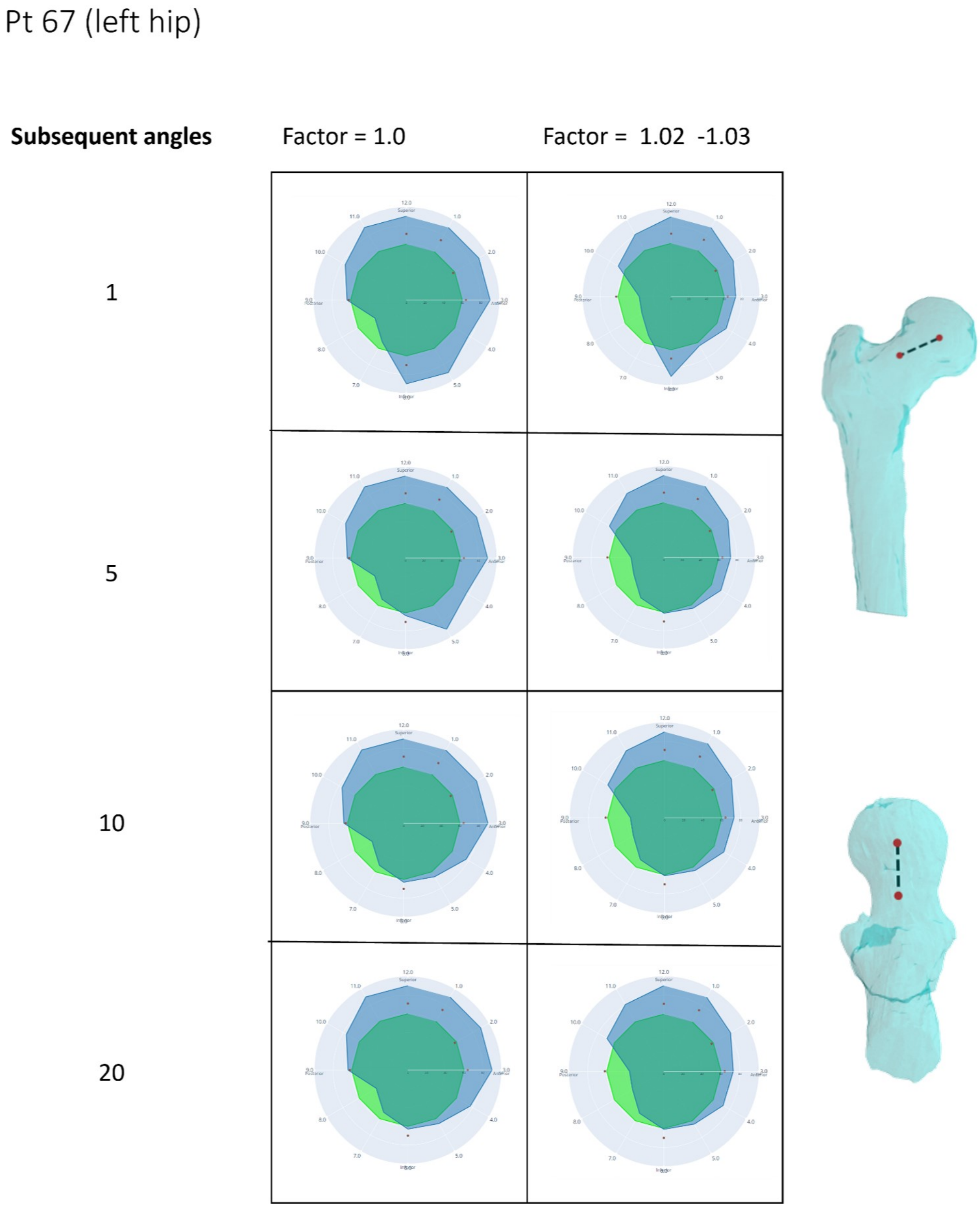

Figure 9.7: Polar plots depicting various alpha angle measurements of the left hip of patient 67: the manual alpha angle measurements for 6 radial positions are depicted by the brown dots. The semi-automated alpha angle measurements are depicted in blue for 12 clockwise positions. The green circle represents the alpha angle threshold of 60 degrees. A polar plot is generated for each different automatic approach: varying the number of subsequent inclination angles for outlier detection and whether there is additional multiplication of the radius by a model specific factor.

Patient 67: Right hip

The 3D model of the right hip of patient 67 shows a very slight anterior bony protrusion. The radiologist localized prominent exceeding alpha angles at the inferior and antero-superior side and a minor exceeding alpha angle at the posterior side. The workflow (Factor = 1.0) also localizes prominent exceeding alpha angles superiorly and inferiorly. Outlier detection detects some outliers inferiorly for the factor = 1.0 workflow, but generally after outlier detection the superior exceeding alpha angles are indicating a prominent bony protrusion and according to the workflow (Factor = 1.02-1.03), there is also still extruding bone at the postero-inferior site.

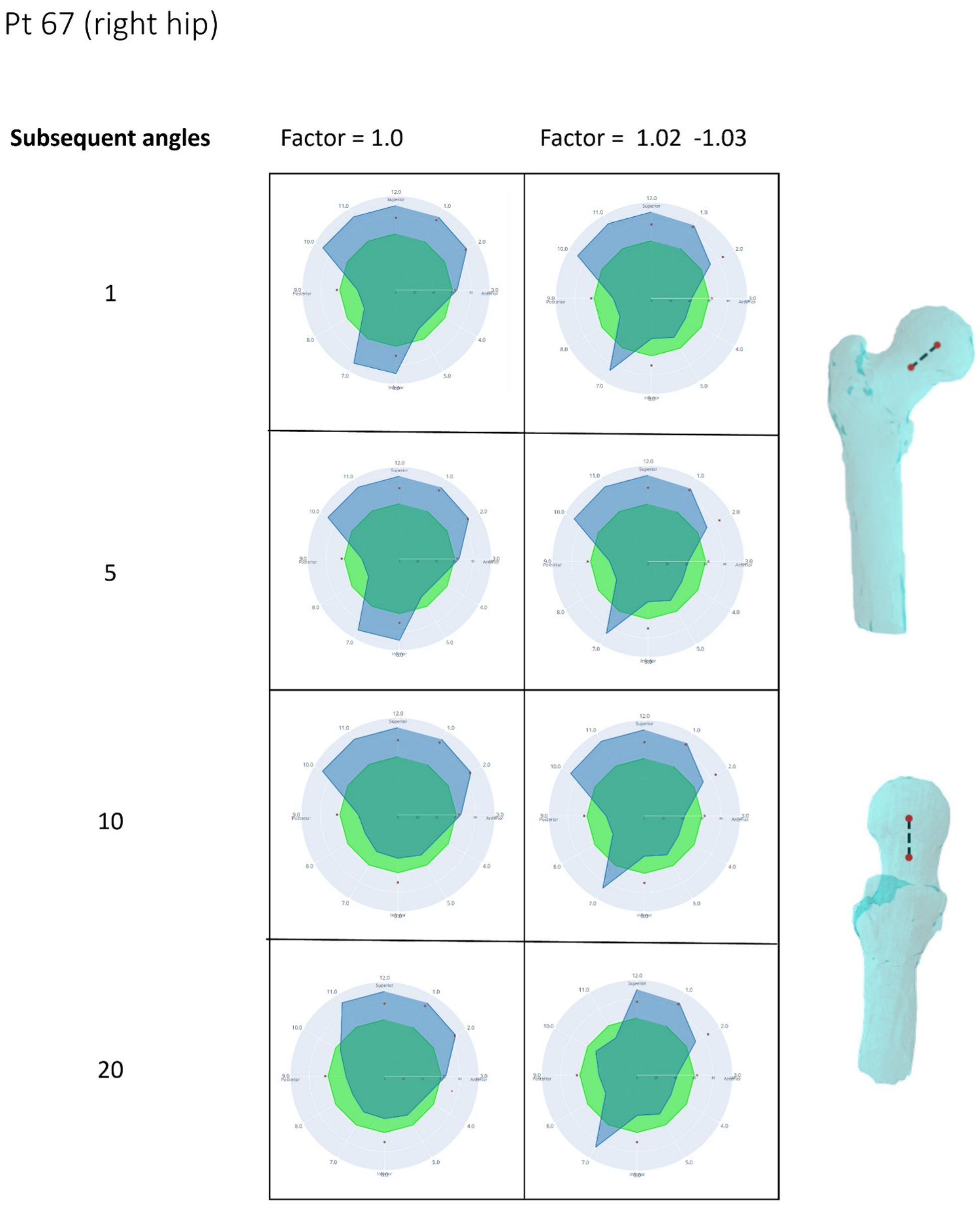

Figure 9.8: Polar plots depicting various alpha angle measurements of the right hip of patient 67: the manual alpha angle measurements for 6 radial positions are depicted by the brown dots. The semi-automated alpha angle measurements are depicted in blue for 12 clockwise positions. The green circle represents the alpha angle threshold of 60 degrees. A polar plot is generated for each different automatic approach: varying the number of subsequent inclination angles for outlier detection and whether there is additional multiplication of the radius by a model specific factor.

10

Appendix B: Clockwise Validation

The main body of this thesis includes the validation of all alpha angle measurements. Additionally, the ICC and MAD were calculated for six clockwise positions separately: 12:00, 1:00, 2:00, 3:00, 6:00 and 9:00 o'clock. For each radial position, centered around the femoral neck axis, a table was created that shows the ICCs and MADs for the comparison of manual measurements vs automatic measurements using various combinations of outlier detection and sphere fitting thresholds. The tables additionally show the mean ± SD, 95 % CI and p-values for all different approaches. The tables are depicted below in this appendix.

Worth noting is that because of the separation by radial position, each reliability measure was based on solely 8 measurements (8 hips). This small dataset is reflected in the large 95% CI interval. MADs range fom 11.63°(Table 10.3) to 33.00°(Table 10.1) and ICCs range from -0.71 (Table 10.4) to 0.40 (Table 10.3). Negative ICC values indicate that the variability within the two measurements exceeds the variability across the measurements.

To enhance the reliability of clockwise measurements, it is necessary to carry out further research with larger sample sizes.

10.0.1. 12:00 o'clock

	Outlier detection - Number of subsequent angles	**Radius Multiplication**	**Mean**	**SD**	**ICC**	**MAD**	**95% CI**	**p-value**
Manual			68.89	4.14				
Automatic (radius specific)	1	1.0	63.75	31.19	0.00	28.38	[-0.67, 0.67]	0.50
	1	factor	41.25	25.11	0.22	31.63	[-0.52, 0.77]	0.28
	5	1.0	50.00	30.12	0.08	31.63	[-0.62, 0.71]	0.42
	5	factor	41.25	25.11	0.22	31.63	[-0.52, 0.77]	0.28
	10	1.0	50.00	30.12	0.08	31.63	[-0.62, 0.71]	0.42
	10	factor	41.25	25.11	0.22	31.63	[-0.52, 0.77]	0.28
	20	1.0	63.75	31.19	0.00	28.38	[-0.67, 0.67]	0.50
	20	factor	41.25	25.11	0.22	31.63	[-0.52, 0.77]	0.28
Automatic (radius aspecific)	1	1.0	58.38	31.91	0.05	30.25	[-0.64, 0.69]	0.45
	1	factor	48.50	29.71	0.11	31.38	[-0.60, 0.72]	0.39
	5	1.0	58.38	31.91	0.05	30.25	[-0.64, 0.69]	0.45
	5	factor	49.00	29.32	0.09	30.89	[-0.64, 0.69]	0.39
	10	1.0	50.38	31.50	0.08	33.00	[-0.62, 0.71]	0.42
	10	factor	48.50	29.71	0.11	31.38	[-0.60, 0.72]	0.39
	20	1.0	58.38	31.91	0.05	30.25	[-0.64, 0.69]	0.45
	20	factor	48.50	29.71	0.11	31.38	[-0.60, 0.72]	0.39

Table 10.1: The absolute agreement between manual and automatic measurements of the alpha angle at 12:00 o'clock in 3D Models of the hip joint: ICCs and MADs with varying outlier detection and sphere fitting thresholds. The table additionally shows the mean ± standard deviation, 95% CI and p-values for different approaches.

10.0.2. 1:00 o'clock

	Outlier detection - Number of subsequent angles	Radius Multiplication	Mean	SD	ICC	MAD	95% CI	p-value
Manual			73.38	7.69				
Automatic (radius section-specific)	1	1.0	79.63	16.39	-0.22	19.25	[-0.77, 0.52]	0.71
	1	factor	65.13	26.59	-0.05	23.25	[-0.69, 0.64]	0.55
	5	1.0	71.75	23.22	0.07	21.25	[-0.62, 0.71]	0.42
	5	factor	65.13	26.59	-0.05	23.25	[-0.69, 0.64]	0.55
	10	1.0	71.75	23.22	0.08	31.63	[-0.62, 0.71]	0.42
	10	factor	65.13	26.59	-0.05	23.25	[-0.69, 0.64]	0.55
	20	1.0	71.75	23.22	0.07	21.25	[-0.62, 0.71]	0.42
	20	factor	65.13	26.59	-0.05	23.25	[-0.69, 0.64]	0.55
Automatic (radius section-aspecific)	1	1.0	70.25	23.21	-0.07	20.63	[-0.62, 0.70]	0.43
	1	factor	59.63	27.52	-0.04	23.63	[-0.69, 0.65]	0.54
	5	1.0	70.25	23.21	0.07	20.63	[-0.62, 0.70]	0.43
	5	factor	60.38	28.01	–0.04	27.75	[-0.69, 0.64]	0.54
	10	1.0	65.76	26.91	-0.02	23.63	[-0.68, 0.65]	0.52
	10	factor	59.63	27.52	-0.04	27.00	[-0.69, 0.65]	0.54
	20	1.0	70.25	23.21	0.07	20.63	[-0.62, 0.70]	0.43
	20	factor	59.63	27.52	-0.03	23.63	[-0.69, 0.65]	0.54

Table 10.2: The absolute agreement between manual and automatic measurements of the alpha angle at 1:00 o'clock in 3D Models of the hip joint: ICCs and MADs with varying outlier detection and sphere fitting thresholds. The table additionally shows the mean ± standard deviation, 95% CI and p-values for different approaches.

10.0.3. 2:00 o'clock

	Outlier detection - Number of subsequent angles	Radius Multiplication	Mean	SD	ICC	MAD	95% CI	p-value
Manual			67.25	11.65				
Automatic (radius section-specific)	1	1.0	75.88	14.56	0.40	11.88	[-0.36, 0.84]	0.14
	1	factor	70.38	18.11	0.32	14.13	[-0.44, 0.81]	0.20
	5	1.0	75.88	14.56	0.40	11.88	[-0.36, 0.84]	0.14
	5	factor	70.38	18.11	0.32	14.13	[-0.44, 0.81]	0.20
	10	1.0	75.88	14.56	0.40	11.88	[-0.36, 0.84]	0.14
	10	factor	70.38	18.11	0.32	14.13	[-0.44, 0.81]	0.20
	20	1.0	75.88	14.56	0.40	11.88	[-0.36, 0.84]	0.14
	20	factor	70.38	18.11	0.32	14.13	[-0.44, 0.81]	0.20
Automatic (radius section-aspecific)	1	1.0	78.63	13.87	0.32	13.38	[-0.44, 0.81]	0.20
	1	factor	69.38	10.45	0.29	11.63	[-0.47, 0.80]	0.22
	5	1.0	78.63	13.87	0.32	13.38	[-0.44, 0.81]	0.20
	5	factor	70.38	11.64	0.39	11.38	[-0.38, 0.84]	0.15
	10	1.0	77.63	13.52	0.22	13.63	[-0.52, 0.77]	0.28
	10	factor	69.38	10.45	0.29	11.63	[-0.47, 0.80]	0.22
	20	1.0	78.63	13.90	0.32	13.38	[-0.44, 0.81]	0.20
	20	factor	69.38	10.45	0.29	11.63	[-0.47, 0.82]	0.22

Table 10.3: The absolute agreement between manual and automatic measurements of the alpha angle at 2:00 o'clock in 3D Models of the hip joint: ICCs and MADs with varying outlier detection and sphere fitting thresholds. The table additionally shows the mean ± standard deviation, 95% CI and p-values for different approaches.

10.0.4. 3:00 o'clock

	Outlier detection - Number of subsequent angles	Radius Multiplication	Mean	SD	ICC	MAD	95% CI	p-value
Manual			58.88	6.25				
Automatic (radius section-specific)	1	1.0	72.75	16.74	-0.35	20.38	[-0.83, 0.41]	0.83
	1	factor	68.63	16.54	-0.25	18.50	[-0.78, 0.50]	0.74
	5	1.0	72.75	16.74	-0.35	20.38	[-0.83, 0.41]	0.83
	5	factor	68.63	16.54	-0.25	28.50	[-0.78, 0.50]	0.74
	10	1.0	72.75	16.74	-0.35	20.38	[-0.83, 0.41]	0.83
	10	factor	67.13	15.00	-0.35	17.00	[-0.82, 0.41]	0.82
	20	1.0	72.75	16.74	-0.71	20.38	[-0.83, 0.41]	0.83
	20	factor	64.25	12.31	-0.34	14.13	[-0.82, 0.42]	0.81
Automatic (radius section-aspecific)	1	1.0	77.63	16.42	-0.38	23.75	[-0.84, 0.38]	0.84
	1	factor	62.5	15.98	-0.45	16.88	[-0.86, 0.31]	0.89
	5	1.0	77.63	16.42	-0.38	23.75	[-0.84, 0.38]	0.85
	5	factor	63.88	17.64	-0.39	18.25	[-0.84, 0.38]	0.85
	10	1.0	73.63	18.94	-0.34	24.50	[-0.82, 0.42]	0.82
	10	factor	62.5	15.98	-0.45	16.88	[-0.81, 0.45]	0.89
	20	1.0	74.75	16.00	-0.40	20.88	[-0.81, 0.45]	0.79
	20	factor	62.5	15.97	-0.45	16.88	[-0.86, 0.31]	0.89

Table 10.4: The absolute agreement between manual and automatic measurements of the alpha angle at 3:00 o'clock in 3D Models of the hip joint: ICCs and MADs with varying outlier detection and sphere fitting thresholds. The table additionally shows the mean ± standard deviation, 95% CI and p-values for different approaches.

10.0.5. 6:00 o'clock

	Outlier detection - Number of subsequent angles	Radius Multiplication	Mean	SD	ICC	MAD	95% CI	p-value
Manual (Notzli method)			69.25	15.78				
Automatic (radius specific)	1	1.0	64.88	16.30	-0.16	21.63	[-0.75, 0.57]	0.66
	1	factor	58.00	14.78	-0.19	23.00	[-0.76, 0.54]	0.69
	5	1.0	64.88	16.30	-0.16	21.63	[-0.75, 0.57]	0.66
	5	factor	58.00	14.78	-0.19	23.00	[-0.76, 0.54]	0.69
	10	1.0	54.13	8.55	0.30	17.63	[-0.46, 0.81]	0.21
	10	factor	52.63	8.76	0.32	18.63	[-0.44, 0.81]	0.20
	20	1.0	54.13	8.55	0.30	17.63	[-0.46, 0.81]	0.21
	20	factor	52.63	8.76	0.32	18.63	[-0.44, 0.81]	0.20
Automatic (radius section-aspecific)	1	1.0	71.75	18.99	0.24	19.50	[-0.50, 0.78]	0.26
	1	factor	56.50	15.19	0.24	19.75	[-0.51, 0.78]	0.27
	5	1.0	65.38	15.82	-0.17	20.88	[-0.75, 0.56]	0.66
	5	factor	53.13	9.08	0.32	18.13	[-0.44, 0.81]	0.20
	10	1.0	54.38	8.77	0.32	17.38	[-0.44, 0.81]	0.20
	10	factor	52.88	8.94	0.20	18.38	[-0.43, 0.82]	0.19
	20	1.0	54.63	8.87	0.31	17.13	[-0.45, 0.81]	0.21
	20	factor	52.88	8.93	0.33	18.38	[-0.43, 0.82]	0.19

Table 10.5: The absolute agreement between manual and automatic measurements of the alpha angle at 6:00 o'clock in 3D Models of the hip joint: ICCs and MADs with varying outlier detection and sphere fitting thresholds. The table additionally shows the mean ± standard deviation, 95% CI and p-values for different approaches.

10.0.6. 9:00 o'clock

	Outlier detection - Number of subsequent angles	Radius Multiplication	Mean	SD	ICC	MAD	95% CI	p-value
Manual			55.13	7.70				
Automatic (radius section-specific)	1	1.0	64.38	24.22	0.15	22.25	[-0.57, 0.74]	0.34
	1	factor	45.25	18.09	-0.02	20.63	[-0.68, 0.65]	0.53
	5	1.0	60.63	22.20	0.19	18.50	[-0.54, 0.76]	0.31
	5	factor	40.63	12.48	-0.38	21.00	[-0.84, 0.38]	0.85
	10	1.0	50.63	19.87	-0.06	20.00	[-0.70, 0.63]	0.56
	10	factor	40.5	12.46	-0.39	21.25	[-0.84, 0.37]	0.85
	20	1.0	54.25	20.07	0.04	17.875	[-0.64, 0.69]	0.45
	20	factor	45.25	18.09	-0.02	20.63	[-0.68, 0.65]	0.53
Automatic (radius section-aspecific)	1	1.0	58.25	22.52	0.04	19.88	[-0.64,0.69]	0.46
	1	factor	42.13	11.79	-0.43	22.63	[-0.85, 0.33]	0.88
	5	1.0	55.0	23.31	-0.03	18.00	[-0.68, 0.65]	0.53
	5	factor	42.88	12.32	-0.41	23.75	[-0.84, 0.36]	0.86
	10	1.0	54.25	23.43	-0.03	23.38	[-0.68, 0.65]	0.53
	10	factor	42.13	11.79	-0.43	18.75	[-0.85, 0.33]	0.88
	20	1.0	46.0	14.34	-0.37	19.13	[-0.83, 0.39]	0.84
	20	factor	42.13	11.79	-0.43	18.75	[-0.85, 0.33]	0.88

Table 10.6: The absolute agreement between manual and automatic measurements of the alpha angle at 9:00 o'clock in 3D Models of the hip joint: ICCs and MADs with varying outlier detection and sphere fitting thresholds. The table additionally shows the mean ± standard deviation, 95% CI and p-values for different approaches.

11

Appendix C: Alternative quantitative imaging parameters

Polar plots of two alternative quantitative imaging parameters for the diagnosis of cam morphology are presented for each 3D hip model in this appendix: the Triangular Index (TI) and the Head-Neck Offset Ratio (HNOR). These two alternative quantitative imaging parameters also evaluate the degree of asphericity in FAIS patients and have been computed in this study in addition to the alpha angle. These measurements are discussed in this appendix instead of the main body of the thesis, because they have not been validated by manual measurements. This appendix provides a speculative discussion on the potential of these alternative quantitative parameters.

11.1. Triangular Index

11.1.1. Introduction

One of the alternative parameters is the triangular index, introduced by *Gosvig et Al.* It measures the length of the natural femoral-head radius (r) along the FNA at a point 0.5 r laterally (Figure 11.1). [42] If the radius R at this point exceeds the natural radius of the femoral head by 1.67 mm, a cam morphology is present. [42]

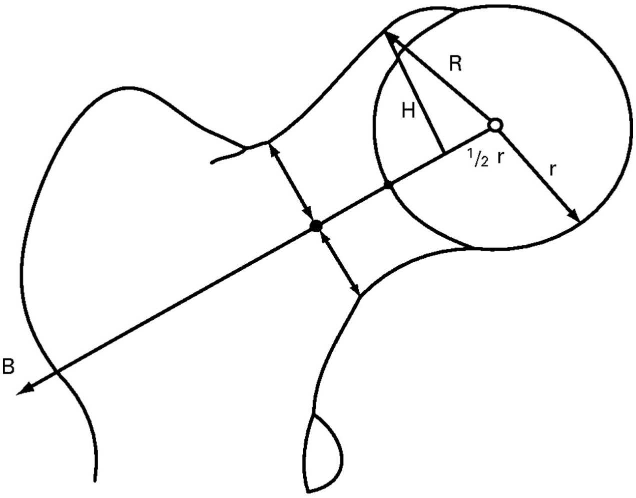

Figure 11.1: The triangular index as quantitative parameter for assessment of asphericity. The radius (r) of the femoral head is measured. Then 1/2 r and the corresponding perpendicular height (H) to the cortex are measured. If the pathologically increased R at 1/2r ≥ r + 1.67 mm, the cam morphology is present.[42]

11.1.2. Method

The TI was computed for all eight hips (four left, four right) using the ray casting algorithm. Rays were cast from the point 1/2 r to obtain a set of locations and heights for each radial position (Figure 11.1). The distance from these locations (points) to the femoral head center formed a radial section-specific TI. Similarly to the alpha angle, polar plots were generated that reflect the TI for 12 radial sections centered around the femoral neck axis.

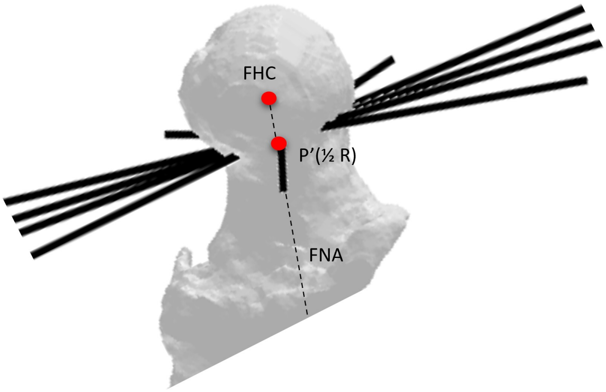

Figure 11.2: Application of the ray-casting algorithm to detect the femoral neck points corresponding to 1/2R.

11.1.3. Results

The green field represents the threshold which is the radius of the fitted sphere + 1.67 mm, a threshold proposed by *Gosvig et al*. [42] The resulting polar plots are visualized in Figure 11.3. The blue protrusions in Figure 11.3 indicate locations where the TI exceeds the threshold, meaning that the resultant radius R2 is at least 1.67 mm larger than the fitted spherical radius R at these points. The size of the blue protrusion reflects the severity of CAM morphology at that location.

For patient 28, the 3D hip model of the left joint revealed bony protrusions in the anterior and posterior areas, which were confirmed by increased TI values in the corresponding areas on the polar plot. The right hip joint showed a cam morphology in the anterior region, with a slight elevation in the TI only at that point (Figure 11.3). Patient 33 had a prominent anterior cam morphology in both hips, which was also reflected by higher TI values in those areas in the polar plots. Patient 45 had normal hip morphology on the left side, which corresponded to TI values below the threshold in all radial positions. However, the right hip showed a slight increase in antero-inferior triangular index, which was not detected in the 3D model. Finally, patient 67's polar plot showed a circumferential increase in TI values, except for the postero-inferior site, which did not correspond to the slight anterior cam morphology detected on the 3D model. The polar plot of the left hip of patient 67 shows an increased TI almost circumferentially except for the postero-inferior site. This does not correspond with the slight anterior cam morphology detected on the 3D hip model. The 3D hip model of patient 67 (right side) shows a very slight anterior cam morphology, which does not correspond to the normal morphology seen on the 3D hip model.

11.1.4. Discussion and Conclusions

The TI polar plots generated by the automatic algorithm using the data set of this study show that the algorithm can accurately detect cam morphology in locations with prominent bony protrusions. For more subtle protrusions, the TI may sometimes reflect the existence of the protrusion, but not always, and may show increased values even when the protrusion is not visually present.

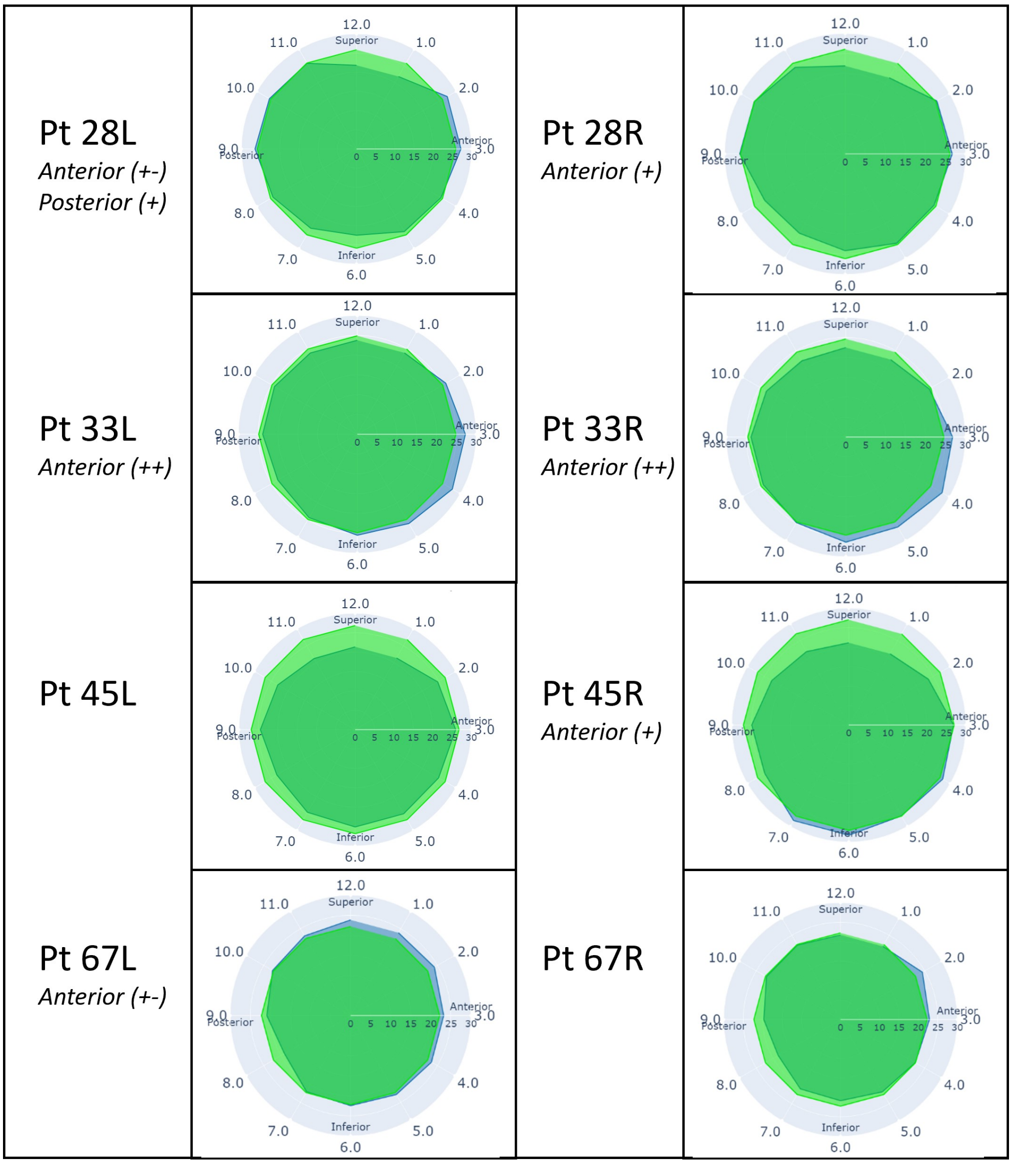

Figure 11.3: Polar plots for each hip, representing the TI for each radial section. The blue area represents the patient specific TI. The green area represents the patient specific threshold. On the side of each polar plot the patient number and hip side is stated together with the location of the cam morphology - qualitatively evaluated. The + and - side indicate the size of the cam morphology.

The advantages of the TI is that it is less influenced by slight changes in radius or positioning of the FHC in comparison to the alpha angle, as it is a more simplified measurement. The TI has shown excellent agreement in 2D radiographs in studies conducted by *Onwuzu et al* (ICC: 0.924) and *Gosvig et al* (ICC: 0.95). *Nicholls et al* achieved good agreement (ICC: 0.74) in detecting the cam morphology using the TI, but all these ICCs were limited to 2D radiographs and have yet to be validated in 3D.[42][43][44]

A limitation of the TI as diagnostic FAIS parameter is that it is measured at 1/2r. This means that small bony protrusions located below or above this location will not be detected. A future recommendation would be that the TI would be measured at 3 locations: 1/3 R, 1/2R and 2/3R to ensure that no bony protrusion is missed or that it should act as a complementary hip parameter besides the alpha angle. First the TI should be validated using manual measurements using a larger dataset. Most importantly, the threshold was set by *Gosvig et al*, but further research should point out whether this is the correct threshold and potentially whether there should be location specific, gender-specific or ethnicity-specific thresholds.

11.2. The Head-Neck Offset Ratio

11.2.1. Introduction

The Head-Neck-Offset Ratio (HNOR) is computed by dividing the Head-Neck-Offset(HNO) by the diameter of the fitted sphere. The HNO is defined as the distance between the tangent of the femoral neck and the tangent of the femoral head parallel to the femoral neck axis (Figure 11.4). A threshold of <0.17 is suggested for the HNOR to be indicative for cam morphology.[45]

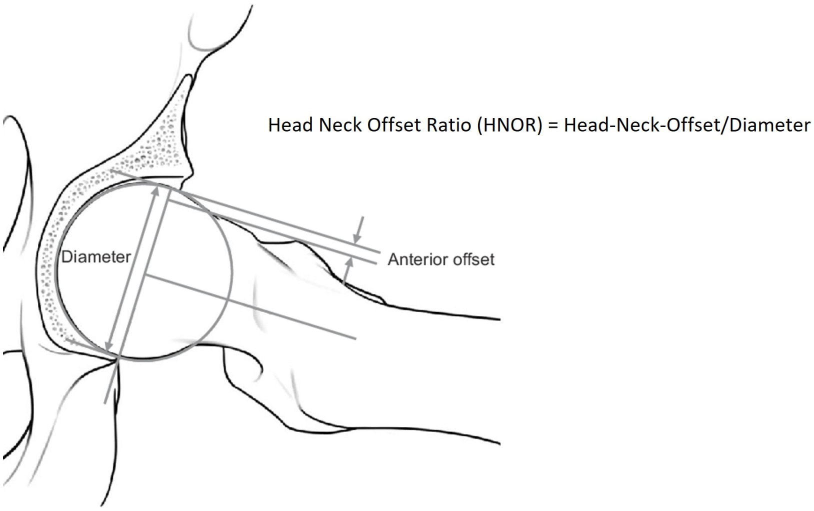

Figure 11.4: The Head-Neck-Offset-Ratio (HNOR).The Head-Neck-Offset (HNO) is defined as the distance between the tangent of the femoral neck and the tangent of the femoral head parallel to the femoral neck axis. A threshold of <0.17 is suggested for the HNOR to be indicative for cam morphology.

11.2.2. Method

The HNOR was computed for 12 radial sections centered around the femoral neck axis in all eight hips using the ray casting algorithm. Rays were cast from the femoral head center and the femoral neck center to obtain two sets of locations and heights for each radial position (Figure 11.5). For each radial position, the distance from the femoral neck to the surface of the 3D model was subtracted from the distance of the femoral head to the surface of the 3D model obtain the HNO. Polar plots were generated for the HNOR for all eight hips.

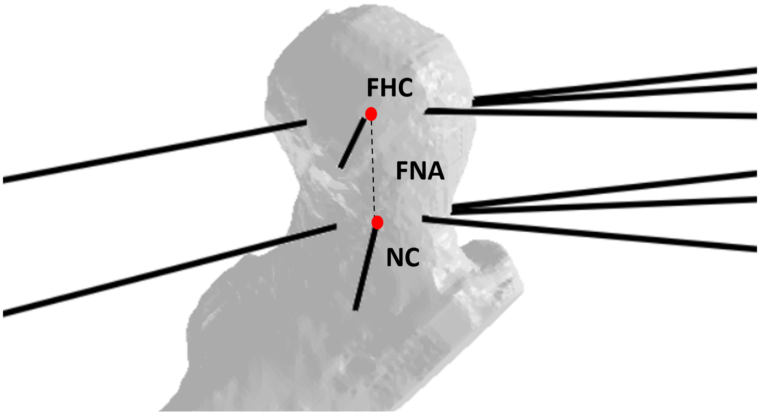

Figure 11.5: Application of the ray-casting algorithm to detect the HNO(R)

11.2.3. Results

The resulting polar plots are visualized in Figure 11.6. The green field represents the threshold which is when the HNOR is larger than 0.17. The blue protrusions in Figure 11.6 represent locations where the Head-Neck-Offset-Ratio does **not** exceed the threshold, meaning that that location has a normal morphology. If the measured HNOR is below 0.17, it stays in the red region, indicative for cam morphology. The location of cam morphology is reflected in lower HNOR at those specific locations, but lower HNORs are also depicted for locations of normal morphologies. Notably, for all 8 hips the HNOR stays below 0.17 at the inferior site. Specifically the superior site, has a very large HNOR for all hips except patient 45 (the left hip) and patient 67 (right hip).

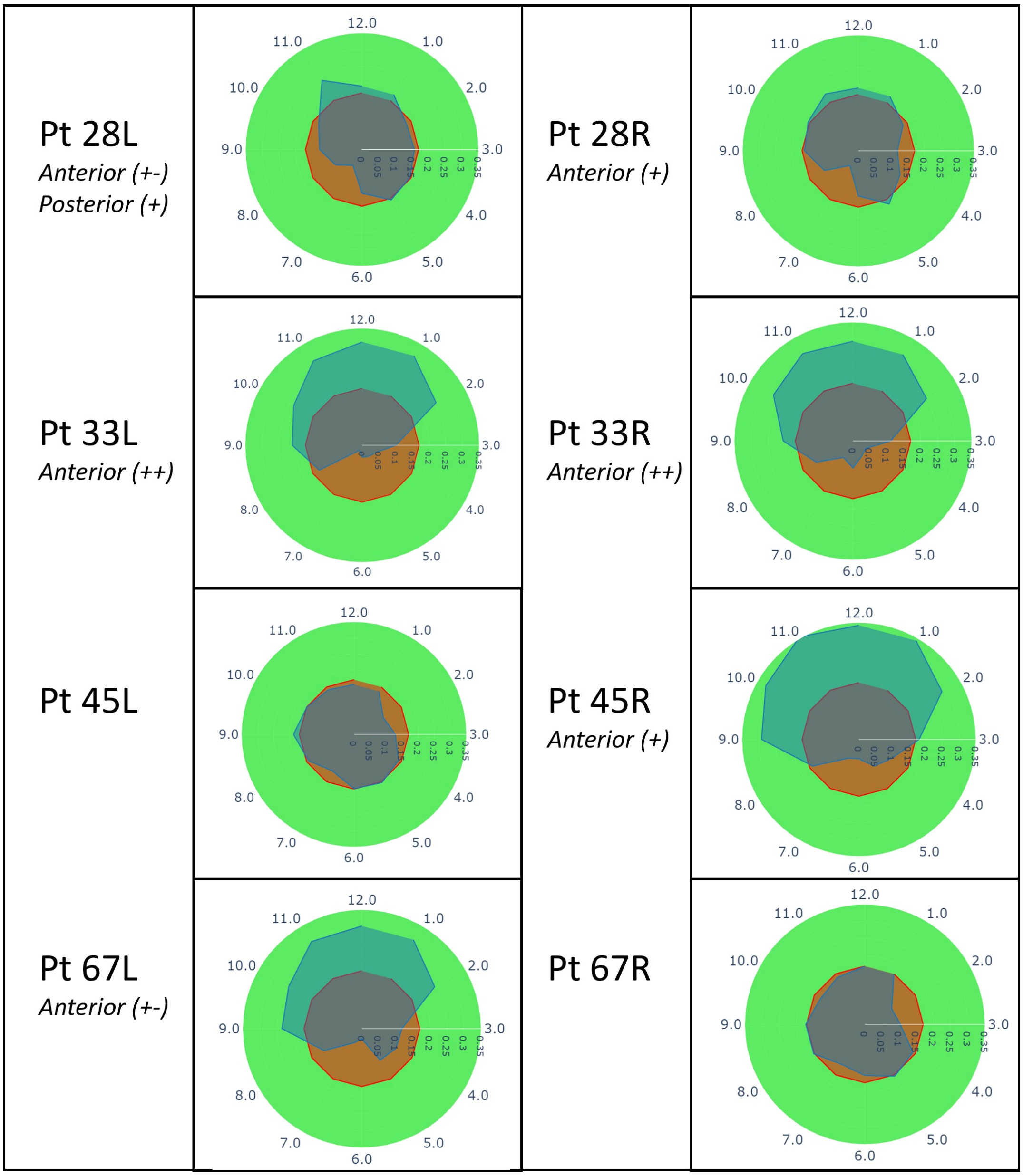

Figure 11.6: Polar plots for each hip, representing the HNOR for each radial section. The blue area represents the patient specific HNOR. The red area represents the threshold of 0.17. Once the blue area is below the red (<0.17) it means that location is indicative for cam morphology. On the side of each polar plot the patient number and hip side is stated together with the location of the cam morphology - qualitatively evaluated. The + and - side indicate the size of the cam morphology.

11.2.4. Discussion and Conclusion

The polar plots generated are capable of detecting the location cam morphology reflected by the HNOR, but the amount of false positives is fairly high. This is most of all attributed to the positioning of the femoral neck axis. As mentioned in the main body of this thesis, the femoral neck axis was positioned rather superior for four hips: 33L, 33R, 45R and 67L. A more superior positioning of the femoral neck axis leads to smaller neck offsets in the superior region and larger neck offsets in the inferior region. This results in high HNORs in the superior region and lower HNORs in the inferior region, which is clearly also visible in the polar plots of these respective hips. This shows the strong dependency of this parameter on the positioning of the femoral neck axis, both automatically and manually. Considering the other four hips that did have an accurate positioning of the femoral neck axis (28L, 28R, 45L and 67R) by visualization, the HNOR polar plots also show a rather odd circumferential shape. This indicates that this parameter might be influenced by an additional error. Nonetheless it would be interesting to investigate its potential with a non-subjective analysis by means of validation or machine learning approaches.